Atmospheric moist convection

Peter Bechtold

Research Department

March 2009 – last revised 4 March 2019

ECMWF
European Centre for Medium-Range Weather Forecasts

TRAINING

Table of Contents

Preface

The current Note covers material presented in the Training course lectures I-IV on "atmospheric moist convection and its parameterization", and further elaborates on other subjects like the diurnal cycle of convection, numerics and the momentum and tracer transport by convection. The aim is to give an overview of convective phenomena and their links with synoptic meteorology, and to provide the basic concepts and parametrization and modelling tools. Of course, not all phenomena could be treated, as e.g. phenomena like monsoon circulations and tropical storms.

The material presented should be easily accessible to beginners in the field, but should also be of interest for people more advanced, and those interested in diverse areas like cloud resolving modelling, and weather forecasting. The references to research articles are certainly not exhaustive, and the reader interested in specific subjects is encouraged to find more references in the cited articles or refer to Textbooks. Among those I would particularly recommend:

- Emanuel K. A., 1994: *Atmospheric convection*, Oxford University Press.
- Houze R., 1993: *Cloud dynamics*, *Academic Press.*
- Holton J. R., 2004: *An introduction to Dynamic Meteorology*, 4th edition, Academic Press.
- Riehl, H. 1979: *Climate and weather in the Tropics,* Academic Press.
- *Dynamic meteorology, midlatitude convection, weather forecasting*
- Bluestein H., 1993: *Synoptic-Dynamic meteorology in midlatitudes*, Vol II, Oxford University Press.

The general circulation

- J. P. Peixoto and A. H. Ort, 1992: *The physics of climate*, American Institute of Physics.
- Steinheimer, M., M. Hantel and P. Bechtold, 2008: Convection in Lorenz's global energy cycle with the ECMWF model. *Tellus* (in press). Also available as *ECMWF Technical Memorandum* **No 545**.

Convection parameterization

- Emanuel K. A. and D.Raymond, 1993: *The representation of cumulus convection in numerical models*, American Meteorological Society Meteor. Monogr.
- Smith R. K, 1997: *The physics and parameterization of moist atmospheric convection*, Kluwer Academic Publishers.
- Bechtold, P., 2008c: Convection parametrization. ECMWF Seminar proceedings on "The parametrization of subgrid physical processes", 63-85. also available under *http://www.ecmwf.int/publications /library/ do/ references/list/200809* .

Atmospheric Thermodynamics

- Dufour L. et J. v. Mieghem, 1975: *Thermodynamique de l'Atmosphère*, Institut Royal météorologique de Belgique
- Iribarne, J. V. and W. L. Godson, 1973: *Atmospheric Thermodynamics*, D. Reidel Publisher Co.

Simulating convection and atmospheric variability

- Bechtold, P., M. Köhler, T. Jung, F. Doblas-Reyes, M. Leutbecher, M. Rodwell, F. Vitart and G. Balsamo, 2008b: Advances in simulating atmospheric variability with the ECMWF model: From synoptic to decadal time-scales. *Quart. J. Roy. Meteor. Soc.,* **134**, 1337-1351. Also available as *ECMWF Technical Memorandum* **No 556**.

1 The nature of moist convection

1.1 Introduction

For a definition of convection we can go back to the principal of Archimedes (260, b.C.) saying that a body immersed in a fluid will be driven upward by a force equal to the difference between its weight and the weight of the fluid displaced. Here we will mainly deal with moist convection, i.e. upward and downward motions ("thermals") that are associated with moist air and water phase changes (clouds). "Dry" convection, e.g. boundary layer convection is dealt with in the "boundary-layer" course, even if it is also of interest to us as "dry" convection might give raise to "moist" convection.

As an example, typical convective cloud systems are identified on an infrared satellite image from 7 April 2003 (Figure 1.1), deep and shallow convection in the midlatitudes and subtropics, tropical convection in the inner tropical convergence zone (ITCZ), tropical mesoscale convective systems (so called squall lines) over land , stratocumulus clouds over the cold waters off the west coasts of Africa and off the west coasts of the continents in general, and convection associated with other prominent convergence zones, here the South Atlantic convergence zone. These cloud systems are forced by radiative effects, surface fluxes and synoptic and large-scale circulations, but also strongly impact on the larger-scales through the radiative effects and in particular through the net release of latent heat in deep precipitating convective systems. However, not only the amount of (convective) precipitation in the Tropics is much larger than in higher latitudes, also the response and forcing differ. Therefore, in the following midlatitude and tropical convection are treated separately.

Figure 1.1: Infrared METEOSAT satellite image (GEOS and Meteosat disks) of 14 August 2016 showing typical deep and shallow convective cloud systems.

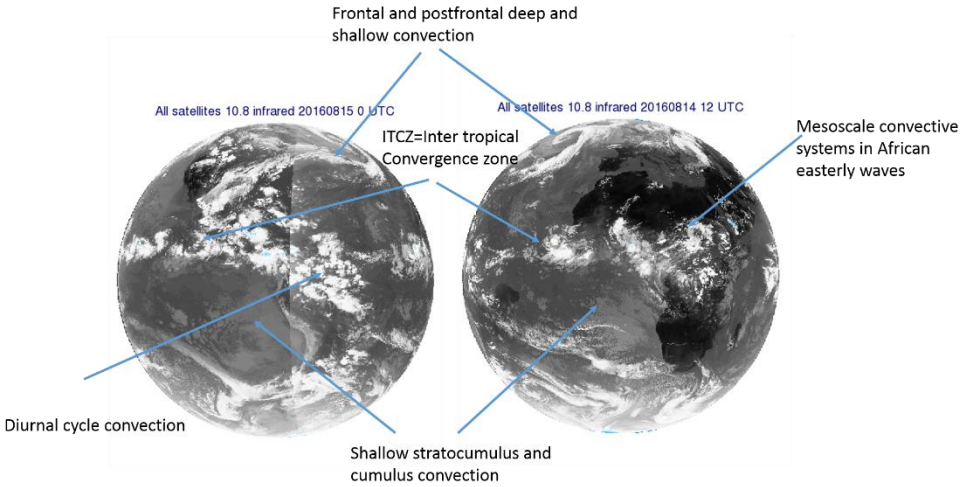

1.2 Tropical Meteorology and Climate

An analysis of the global energy cycle shows that convection is the main physical process that generates kinetic energy in the atmosphere (Steinheimer et al. 2008). The net release of heat (precipitation that reaches the ground) in deep convection implies a perturbation to the atmosphere that must be evacuated. This occurs via fast propagating gravity waves (typically with speeds on the order of 30 m s^{-1}), similar to what is happening when a stone is thrown in a lake. A detailed description of the adjustment process and the wave equations cannot be given here - the interested reader is referred to a few examples for the (wave-like) adjustment process (return to equilibrium) that are provided in the **Appendix** - further recommended articles are Bretherton and Smolarkiewicz (1989), Mapes (1997), Sobel et al. (2001) or Eitzen and Randall (2005). However, the fundamental difference between the Tropics and the midlatitudes resides in the radius of influence over which this perturbation spreads, which is given by the Rossby radius $Ro=N\,H\,f^{-1}$, where N, the Brunt Väisälä frequency ($N^2 = g\vartheta^{-1}\,d\vartheta/dz$, with g the gravitational constant, and ϑ the potential temperature) is a measure of the vertical stability, f is the Coriolis parameter, and H the tropopause height. As in the Tropics f tends to zero Ro tends to infinity, which means that perturbations in the Tropics affect the whole tropical belt, whereas Ro in midlatitudes is on the order of a few thousand kilometers ($f \sim 10^{-4} s^{-1}$, H=8-15 km, $N \sim 0.1\ s^{-1}$, g=9.81 m s^{-2}). We still have a lot to learn about the interaction of convective perturbations with the larger-scale circulations ("the chicken and egg") using observations high-resolution large-domain numerical simulations of tropical convection together with "spectral" analysis

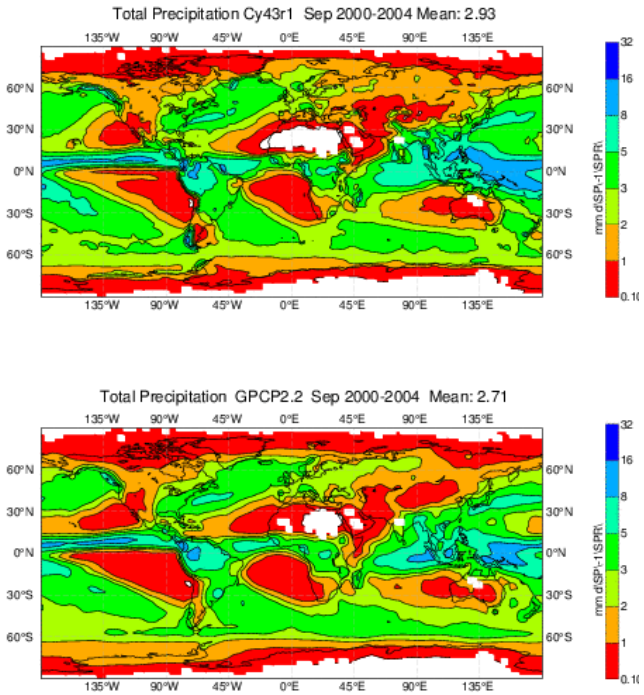

Figure 1.2: Global annual distribution of surface rainfall (mm/day) from the GPCP data set version 2.2 (a combination of surface observations + satellite derived rain rates), and simulated by the IFS cycle 43R1 (autumn 2016) at resolution T255 (80 km) and 137 levels for the period September 2000 to August 2004. Evaluations can be accessed under http://www.ecmwf.int/en/forecasts/charts/physics/

methods (e.g. Grist 2002; Grabowski 2003; Yano et al. 2005, Nasuno et al. 2006, Lin et al. 2008). In particular, Shutts (2008) and Herman et al. (2016) "isolated" Kelvin waves and demonstrated the interaction (energy conversion) of convection with the large-scale wave through a positive correlation between the convective heating in the upper-troposphere and the positive temperature anomaly of the wave. Here only a description of the main meridional and zonal circulations is given.

1.2.1 Precipitation and radiative convective equilibrium

The global annual distribution of rainfall for 2000/2001 from the GPCP project (a combination of satellite derived rainfall rates and surface observations) and those from a one-year integration of the ECMWF Integrated Forecasting System (IFS) are depicted in Figure 1.2. The global average daily rainfall rate is around 3 mm day^{-1}, but most of the precipitation occurs in the tropical belt with a rate of 5-7 mm day^{-1}. The dry subtropical anticyclonical areas to the west of the continents are also apparent as well as the midlatitude storm tracks.

It might appear counterintuitive, but the tropical convection is driven by the radiative (clear sky) cooling of the atmosphere which together with warm sea surface temperatures or surface heating over land provides the necessary vertical destabilization of the troposphere for convection to occur. Note that a cooling rate of 2 K day^{-1} in the lowest 15 km of the troposphere corresponds to a surface precipitation rate of 5 mm day^{-1}. The radiative convective equilibrium is illustrated in Figure 1.3, where the profiles of the different physical tendencies (radiation, dynamics, convection, clouds, and boundary-layer diffusion) averaged over the tropical belt 20°N-20°S have been obtained from the IFS. The distinction between clouds, convection and boundary-layer diffusion is somewhat arbitrary as these tendencies are only available through parameterization, but the main point is that there is on average a radiative cooling of 1-2 K day^{-1} that is balanced by strong heating from precipitating convection and dynamical cooling, which represents the ascending branch of the Hadley cell. For humidity there is drying of the free troposphere (above 850 hPa) by convective precipitation and moistening by dynamical ascent, whereas the moisture in the boundary-layer has been evaporated over sea and advected from the subtropics.

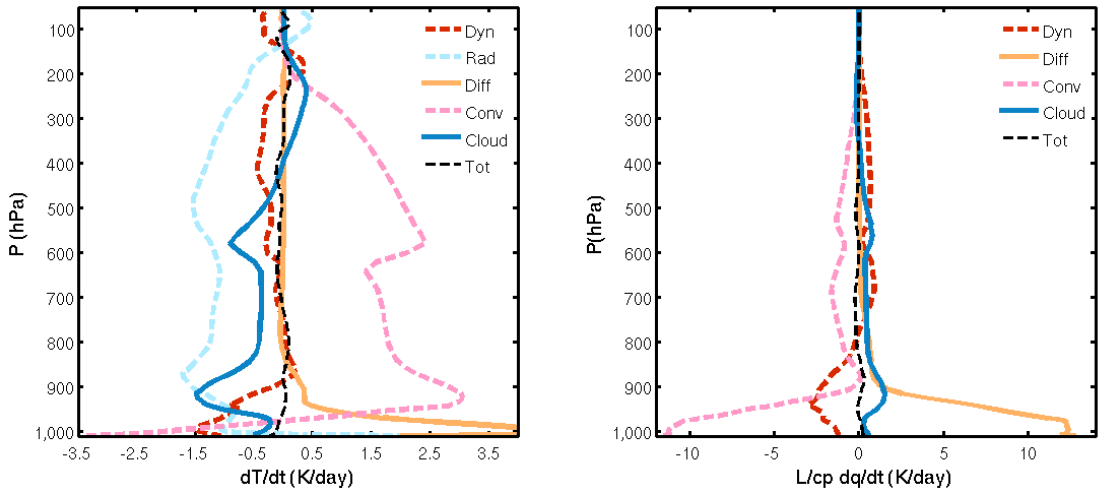

Figure 1.3: Tendencies from the different physical processes as computed in the IFS and averaged over the tropical belt between 20N-20S. Dyn denotes the dynamical tendency (horizontal + vertical advection), Diff the contribution from the boundary-layer diffusion scheme, Conv the contribution from shallow and deep convection, Cloud the large-scale condensation/evaporation processes, and Rad the radiation, the black line corresponds to the sum of all individual contributions.

1.2.2 Cloud distributions

The global distribution of convective clouds can be inferred from satellite observations. As a proxy for these observations the annual frequency of occurrence of deep convective clouds (defined as having a thickness exceeding 200 hPa and positive buoyancy) and shallow convective clouds (defined as "convective" - meaning is explained later) but having a thickness < 200 hPa) as obtained from the IFS convection parameterization are shown in Figure 1.4. A comparison of these distributions with independent satellite observations measuring e.g. the liquid water path (SSMI), the radiation budget (CERES) etc. shows that the distributions in Figure 1.4 are reasonable, and certainly sufficient for the main points we wish to make: deep convective clouds are a prominent feature of the tropical belt, whereas shallow convective clouds are an ubiquitous feature of the subtropical anti-cyclonic regions, where they are called "trade wind cumuli".

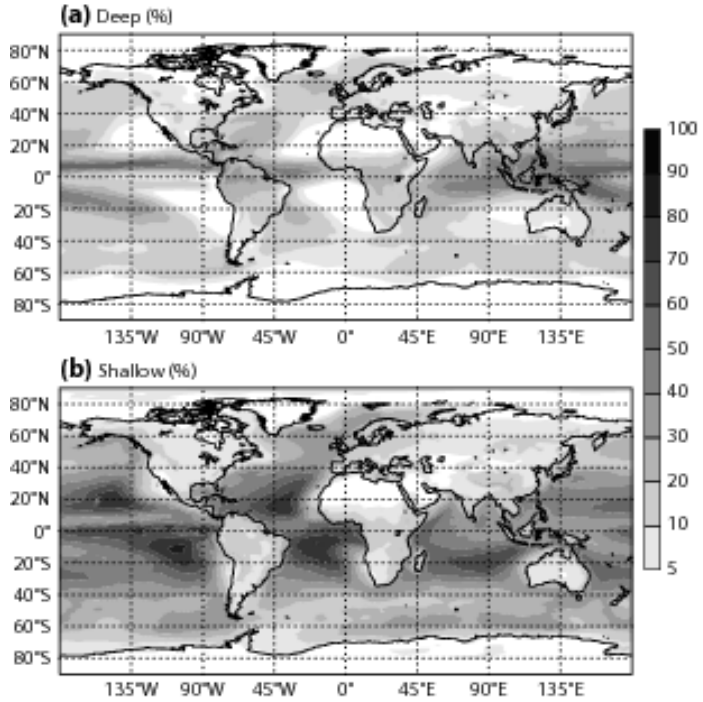

Figure 1.4: Mean annual frequency of occurrence of (a) deep and (b) shallow convective clouds as obtained with IFS Cy40r1.

Trade wind cumulus

As shallow convective clouds are already extensively treated in the "Boundary-Layer Course", the detailed processes that lead to their formation will not be treated in this Course. Instead, a brief discussion is included here about trade wind cumulus in the context of large-scale equilibrium. In Figure 1.5 are depicted the different layers that compose the troposphere in the subtropics, i.e. the subcloud layer, the cloud layer, the inversion layer, and the free troposphere. In the troposphere there is equilibrium between clear sky radiative cooling and subsidence, in the inversion layer subsidence warming compensates evaporative cooling at cloud tops, whereas in the cloud layer mean subsidence and "cumulus induced subsidence" (this term will be explained thoroughly later in the course) balance radiative cooling that mainly occurs in the clear sky part of the domain - trade wind cumuli generally occupy less than 10% of the domain. Finally, in the subcloud layer there is balance between the surface heat fluxes and the heat flux out of the subcloud layer.

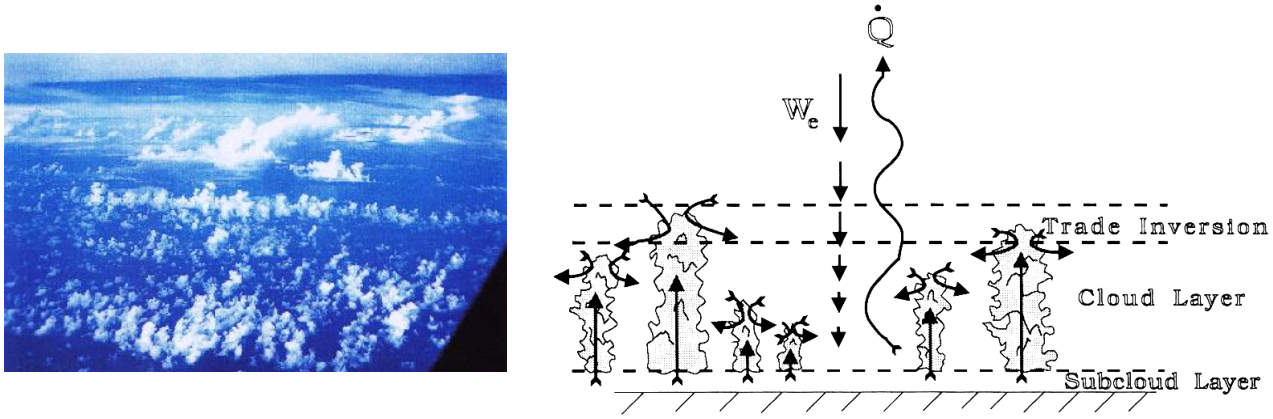

Figure 1.5: Photo of trade wind cumuli, and schematic of equilibria in trade wind boundary layers. (After Emmanuel)

Three modes of convection

Actually one can distinguish three prominent modes of convection (Figure 1.6), shallow convection that penetrates to the trade inversion layer or, more generally, to the boundary-layer inversion layer, deep precipitating convection that reaches the tropopause or some tropopause inversion layer, and cumulus congestus that penetrate to the melting layer, a thin stable layer at the zero degree isotherm (in the Tropics located around 500 hPa) that is maintained by melting of ice phase precipitation. As discussed in numerous studies (e.g. Johnson et al. 1999, Redelsperger et al. 2002), cumulus congestus can make up to 50% of all convective clouds over the tropical Western Pacific. Therefore, they play an important role in the overall energy and mass budget, but also in a moistening = preconditioning of the middle troposphere for subsequent deep convective events. As in tropical regions shallow cumulus and cumulus congestus generally do not penetrate the zero-degree isotherm, their dynamical and microphysical properties necessarily differ from that of deep convective clouds.

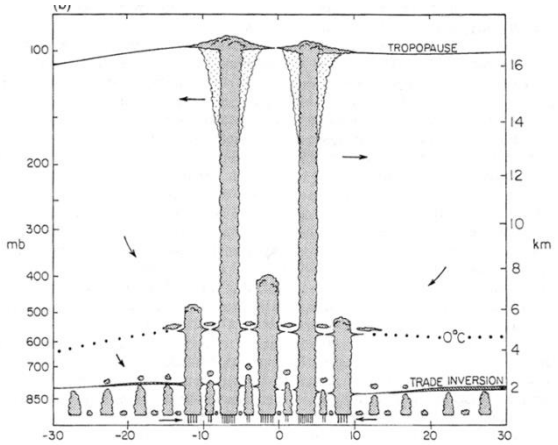

Figure 1.6: The three-modal structure of convection, deep, shallow, and cumulus congestus, and prominent tropospheric inversion layers. (After Johnson et al. 1999)

1.3 Tropical Circulations

1.3.1 The Hadley and Walker circulation

The most prominent tropical meridional circulation is named after the 18th century Englishman George Hadley. As already mentioned it has its ascending branch over the ITCZ (which typically is at 5-10°N over the Pacific Ocean, but strongly migrates over the continents) and its descending branch over the subtropics. As the deep Tropics land and water masses absorb the majority of the solar energy of the globe and transfer it to the atmosphere, and the infrared energy radiated back to space varies only little with latitude, a meridional temperature gradient exists, and heat must be exported from the Tropics to the higher latitudes. This is the thermally direct Hadley cell. But keep in mind that this description is simplistic as we have not mentioned the dynamic (geostrophic) constraints on this circulation. An idealized picture of the Hadley circulation is illustrated in Figure 1.7 showing a cross section over the Pacific with the rising and descending branches of the Hadley cell, the associated increase of the cloud top height toward the Equator with increasing sea surface temperature and decreasing subsidence, and the low-level return flow from the subtropics to the Tropics in the boundary-layer. An estimate of the magnitude of the subsiding motion above the boundary-layer in the subsiding branch of the Hadley cell can be obtained assuming an equilibrium between radiative cooling and heating by subsidence: $w\, d\vartheta/dz = d\vartheta/dt\_rad$. With $d\vartheta/dt\_rad = -1\text{-}2$ K day^{-1} (Figure 1.3), and $d\vartheta/dz$~0.5 K/100 m, one obtains w~ -0.5 cm s^{-1}.

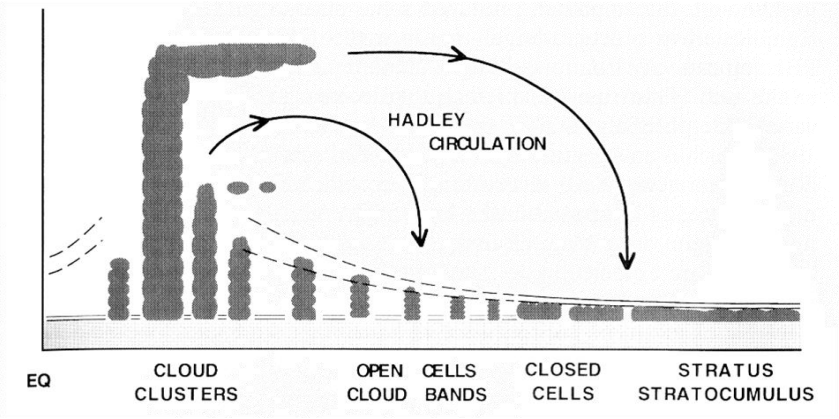

Figure 1.7: Schematic NE-SW cross section over the northeastern Pacific or Atlantic from 40N to the Equator showing the characteristic increase of cloud top height and boundary-layer inversion height with increasing sea surface temperatures and decreasing subsidence. The deep tropical cumulus clouds denote the ascending branch of the Hadley cell, shallow cumuli and stratocumulus clouds can be found in the descending branch.

However, the pattern of convection in the equatorial regions exhibits strong departures from zonal symmetry. This was recognized by G. T. Walker who explained the particular significance of the east-west overturning along the Equator (Figure 1.8), and in particular between the Indonesia region, where under normal condition most of the rainfall occurs (see also Figure 1.2), and the eastern Pacific. The migration of the ascending branch and associated deep convection to the east (El Niño phase) is related to sea-surface temperature variations by wind-driven ocean currents.

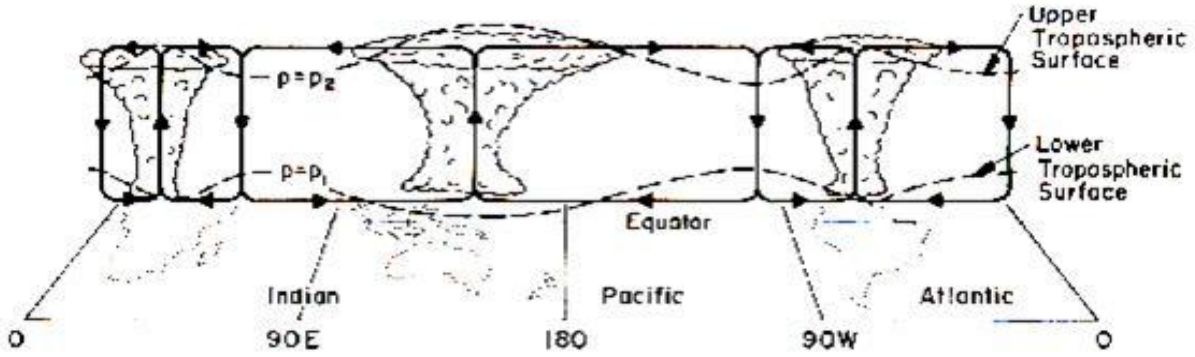

Figure 1.8: Illustration of the zonal Walker circulation for normal conditions. (After Webster and Chang 1988)

1.3.2 Tropical Waves

Taking a spectral view of the tropical motions, one can identify wave motions, so called convectively coupled waves that are eastward and westward propagating disturbances trapped about the Equator. The existence of these waves can be shown analytically using e.g. the linearised momentum and continuity equations in Cartesian coordinates on a β-plane (the Coriolis parameter varies in the latitudinal=*y* direction), specifying the mean horizontal motion *u*, setting the mean meridional motion *v* to zero, and searching for the solution of the perturbation velocity *v'* which generally will be a function of wavenumber *k* and frequency υ. Recall that waves are dispersive if υ is a function of *k*, where υ/k is the phase speed, and $\partial\upsilon/\partial k$ the group speed, i.e. the speed with which the wave energy propagates. The reader interested in a detailed derivation of these equations, the specific dispersion relations, and the stability criteria for damped or growing wave motion is referred to e.g. Holton (pp. 394 ff.), Cho and Pendlebury (1997), Verkley and van der Velde (2010); for an identification of these waves from satellite data and analysis the reader is referred to Wheeler and Kiladis (1999), Yang et al. (2003), and Cho et al. (2004), Žagar et al. (2005). The forcing of stationary wave motion by diabatic heating is explained in Simmons (1982). Experimentally one can identify tropical waves from satellite observations, mainly the outgoing long-wave radiation, and analysed wind and height fields, after having subtracted the background field (or "noise") via appropriate filtering methods. A few simple techniques to derive linear wave types and practical examples are provided in the **Appendix**.

1.3.3 The equatorial Kelvin and Rossby wave

Among the most important equatorial wave types are the Kelvin and the Rossby wave as illustrated in Figure 1.9. The Kelvin wave is a Gaussian function centred on the Equator with a positive (eastward) phase speed of about 18 m s^{-1}. As can be seen from Figure 1.9a the Kelvin wave is 50% rotational and 50% divergent, and forms some eastward propagating dipole like a shallow water gravity wave.

The equatorial Rossby wave (Figure 1.9b) is a westward propagating wave with a phase speed of around 5 m s^{-1}, and is also symmetric to the Equator. Its kinetic energy is larger than the potential energy, with the kinetic energy being at maximum at the Equator and the potential energy being at maximum off the equator.

These waves (modes) can be extracted from real data by either using a filtering in the wavenumber frequency domain (e.g. Wheeler and Kiladis (1999), this however requires long time series, or by projection of the 3D data at a given time onto the normal modes as developed by Žagar et al. (2015) . Results from the latter method are displayed in Figure 1.9c showing the ECMWF analysis of the horizontal wind and geopotential at 850 hPa and its decomposition into the zonal wave number 1 Kelvin mode and the zonal wave number 1-2 rotational (Rossby) modes. Interestingly, a strong MJO (see next paragraph) is present in the equatorial West Pacific which seems to be dominated by the Rossby modes.

All these modes are an integral part of the Hadley and Walker circulations.

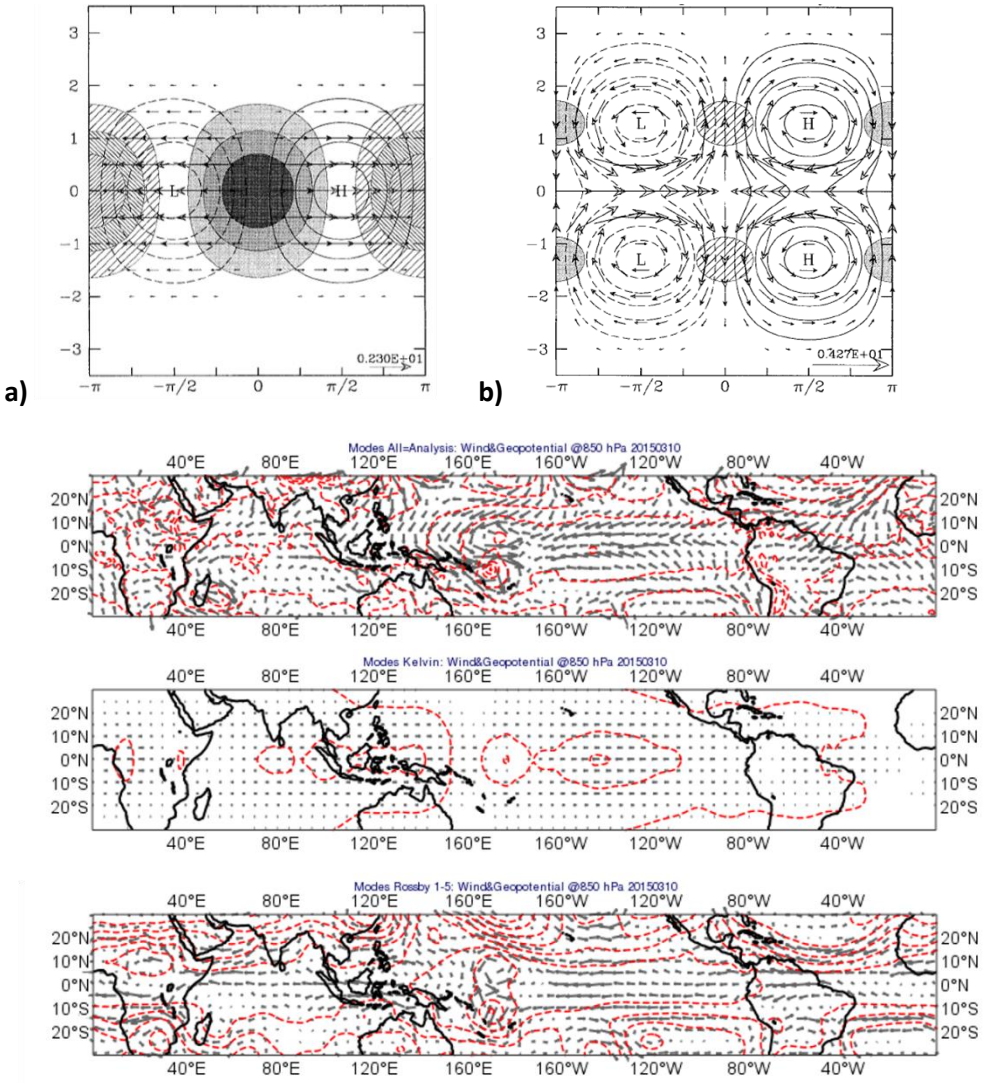

Figure 1.9: Schematic of (a) an equatorial Kelvin wave and (b) a Rossby wave. The Kelvin wave composite makes use of outgoing long-wave radiation (OLR) , height and wind perturbations at 200 hPa, whereas the OLR, stream function and wind field at 850 hPa have been used for the Rossby wave. (Wheeler et al. (2000)). (c) shows a "real" wave decomposition of the ECMWF wind and geopotential analysis for 9 March 2015 at 850 hPa into zonal wavenumber 1 Kelvin and zonal wavenumber 1-5 rotational (Rossby) modes using the software developed and described in Žagar et al. (2015).

1.3.4 African easterly waves

A very distinct type of tropical waves occurs over Africa, in particular north of the Equator between June and October, the so called African easterly waves. This wave type is very important as most of the precipitation in West and Sub-Saharan Africa is associated with mesoscale convective systems forced by these waves (Mohr and Thorncroft, 2006). African easterly waves have periods of 2-6 days, typical wavelengths of about 2500 km and westward propagation speeds around 8 m s^{-1} (Diedhiou et al. 1999, Grist 2002, Nicholson and Grist 2003, Hsieh and Cook, 2005). The particularity of the tropical meteorology in Africa is the existence of a Jet stream in boreal summer at around 600-700 hPa, the African Easterly Jet (AEJ), between the humid and relatively cool equatorial regions and the very hot and dry Sahara. It therefore results from the thermal wind balance in response to the strong meridional temperature gradient. Note that due to small temperature gradients (typically <1 K/1000 km) the tropical regions are generally void of Jet streams, with the notable exceptions of a weak low-level Jet over South America, and an upper-tropospheric Jet around 100-200 hPa between India and Africa, the Tropcial Easterly Jet (TEJ). The TEJ forms in the outflow region of the Indian Monsoon as a result of *quasi-geostrophic adjustment* (the adjustment of the geostrophic wind and height field to the convective heating). The African easterly waves are thought to form as a result of the *barotropic* and *baroclinic* instability of the Jet, where barotropic represents the meridional shear of the Jet and baroclinic the vertical shear of the Jet - like in midlatitude synoptic perturbations. The instability condition for the AEJ (see references given above) requires the quasi-potential vorticity ξ gradient to become negative

$$\frac{\partial \xi_g}{\partial y} = \underbrace{\beta - \frac{\partial^2 \bar{U}}{\partial y^2}}_{barotropic} \underbrace{- f_0^2 \frac{\partial}{\partial p}\left(\frac{1}{S}\frac{\partial \bar{U}}{\partial p}\right)}_{baroclinic}; \quad S = -\frac{1}{\rho\bar{\theta}}\frac{\partial \bar{\theta}}{\partial p} \tag{1.1}$$

where U is the mean zonal wind, β represents the meridional variation of the Coriolis parameter, f *is* the Coriolis parameter at a given latitude, an d S a stability parameter ; ξ is thoroughly explained in Section 1.4.

Luckily, one can visualise African wave activity from analysis or forecasts without filtering. In Figure 1.10 are plotted the mean sea level pressure, the meridional velocity v for 29 September 2005 18UTC, as well as the precipitation in the previous 6 hours from an 18h operational forecast. One clearly identifies the Saharan heat low, the undulations in the wind and pressure field between 10 and 18°N, as well as the precipitation systems south of these undulations. As shown in Figure 1.11 the waves and their zonal propagation are readily identified with the aid of a time-longitude plot (Hovmöller diagram) of the meridional wind, or

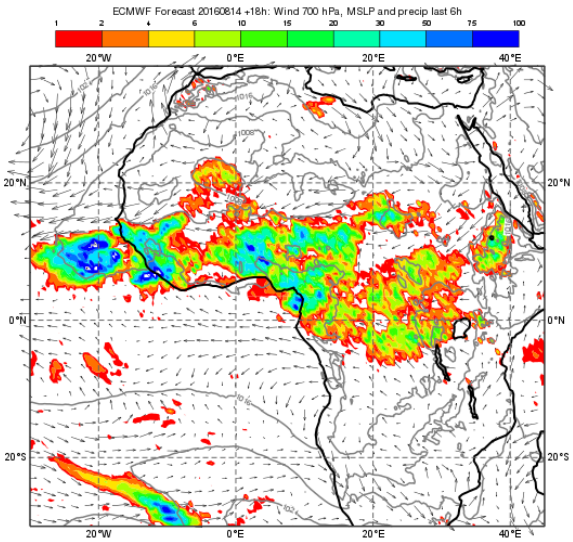

Figure 1.10: Mean sea level pressure (hPa), precipitation rate (mm/day), and 700 hPa wind vectors over Africa from an 18h operational forecast with the IFS for 14 August 2016.

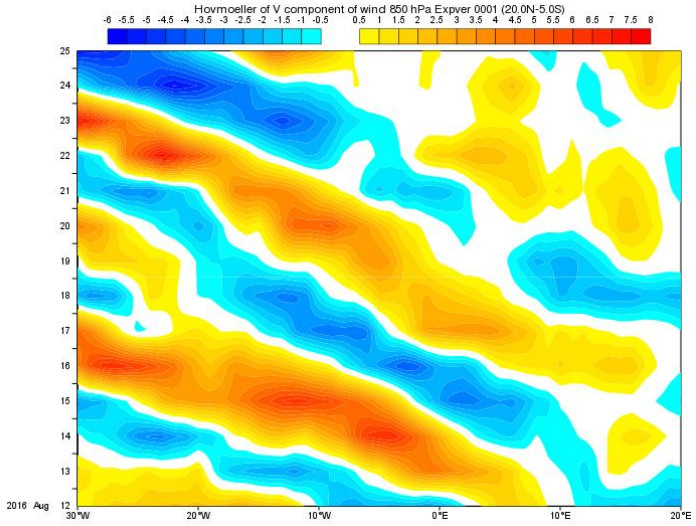

Figure 1.11: Hovmöller longitude-time plot of 6-hourly analysed ECMWF 850 hPa v velocities averaged over 5S-20N between 10 August and 9 September 2005.

alternatively the OLR. The ECMWF analysis between 10 August 2005 and 9 September 2005 has been used and all fields are averaged over latitudes 5°S-20°N. The waves in Figure 1.11 originate near 20°E or 0°E, and with typical periods of 4 days, and westward propagation speeds between 7-10 m s^{-1}, they correspond to the classical picture of Rossby-type waves and are called African easterly waves.

1.3.5 Tropical waves and the MJO

The Madden-Julian Oscillation (MJO) identified by Madden and Julian (1971)- see the review paper by Zhang (2005) as well as Matthews (2008), and Vitart and Molteni (2010) for a more thorough description and teleconnections)- is a massive area of convection composed of several tropical wave types, often developing in the Indian Ovean and then propagating eastward at a speed of roughly 5 m s^{-1}. The MJO is strictly not an oscillation as it can be sporadic, but has maximum spectral power in the 20-80 day frequency range. A strong MJO observed on 27 November 2011 is shown in Figure 1.12, where are also superposed in a schematic way the characteristic Equator symmetric wind gyres at 850 and 200 hPa, given by the ECMWF analysis. As a result of these gyres strong low-level westerlies occur behind the area of main convection whereas easterly inflow occurs ahead of the convection.

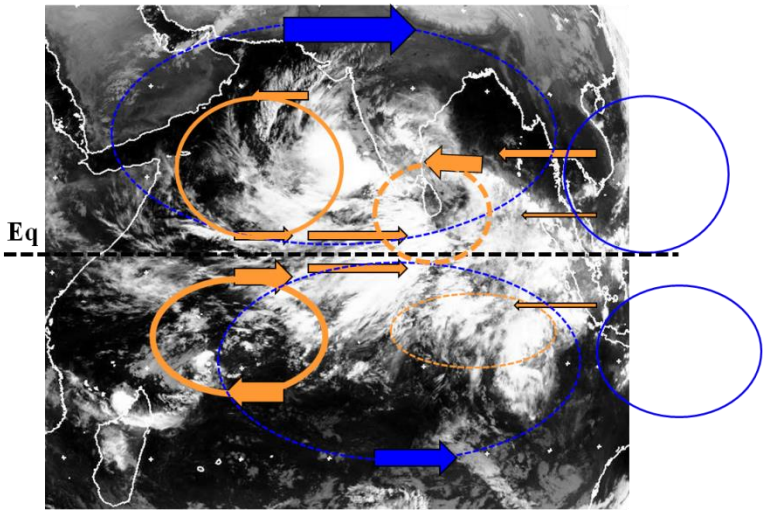

Figure 1.12: A strong MJO event over the Indian Ocean observed the 27 November 2011. In schematic form are superposed the 850 hPa winds (orange) and 200 hPa winds (blue) form the ECMWF operational analysis showing the characteristic equatorially symmetric gyres. The MJO is tilted with height to the West, with low-level westerly flow behind and easterly flow ahead, and these gyres are in an idealised case counter rotating – but in the present case the low-level dashed gyre pair also showed positive vorticity.

Finally, a convenient way to analyse all tropical waves/oscillations consists in computing so called wavenumber-frequency diagrams (Wheeler and Kiladis 1999) with the aid of a double discrete Fourier transform over time and space. The practical difficulty however, consists in subtracting an appropriate reference wave spectrum in order to filter out the significant modes. Typical variables analysed with this method are the Outgoing Longwave Radition (OLR which is also available from satellite observations), the wind components or the smoother fields of the velocity potential and/or the streamfunction which are the inverse Laplacian of the divergence and the vorticity, respectively. The wavenumber-frequency diagram for the tropical OLR from NOAA satellite is depicted in Figure 1.13a . The westward propagating Rossby modes and eastward propagating Kelvin modes become easily apparent. The maximum amplitude of the eastward propagating modes is at wavenumbers one and two, and with frequencies between 20 and 60 days this signal is often referred to as the MJO.

Figures 1.13b,c show the corresponding wave-number frequency spectra from an ensemble of 1-year T159 integrations with the IFS cycles 31r1 (2006) and Cy38r1 (2012/13). Until 2007 the IFS had problems in simulating the tropical wave spectra and in particular the eastward propagating Kelvin waves and the MJO. However, since cycle 32R3 (operational 6 November 2007) that contains revisions to the convection parametrization (entrainment and closure in Bechtold et al. 2008a,b) the IFS is able (Figure 1.13c) to realistically represent the wave spectra, in particular it reduces the amplitude of the Rossby waves and now also represents the eastward propagating Kelvin waves and the MJO.

1.3.6 Summary of tropical motions and scales

There are still uncertainties concerning our knowledge about the interaction between convective and synoptic scales in the Tropics.

Horizontal temperature fluctuations in the Tropics are small <1K/1000 km; and in the absence of precipitation the vertical motions (subsidence) tend to balance the cooling through infrared radiation loss:
$w\, d\theta/dz = d\theta/dt\_rad = -1-2\ \mathrm{K\,day^{-1}} \Rightarrow w \sim -0.5\ \mathrm{cm\,s^{-1}}$.

- In the absence of condensation heating, tropical motions must be barotropic (density variations are only a function of pressure and not of temperature) and cannot convert potential energy in kinetic energy. Therefore they must be driven by precipitating disturbances or lateral coupling with midlatitude systems.
- When precipitation takes place, heating rates are strong; e.g. 100 mm day^{-1} precipitation correspond to an energy flux of 2900 W m^{-2} or an average 30 K day^{-1} heating of the atmospheric column, implying an ascent rate w ~ 8.6 cm s^{-1}. However, this positive mean motion is composed of strong ascent of order w~1 m s^{-1} in the Cumulus updrafts and slow descending motion around ("compensating subsidence").
- When analysing the vorticity equation it appears that in precipitating disturbances the vertical transport of vorticity (momentum) through Cumulus is important to balance the divergence term. On average, cumulus convection tends to slow down the horizontal winds what is often called "cumulus friction", where horizontal momentum is conserved, but not kinetic energy.

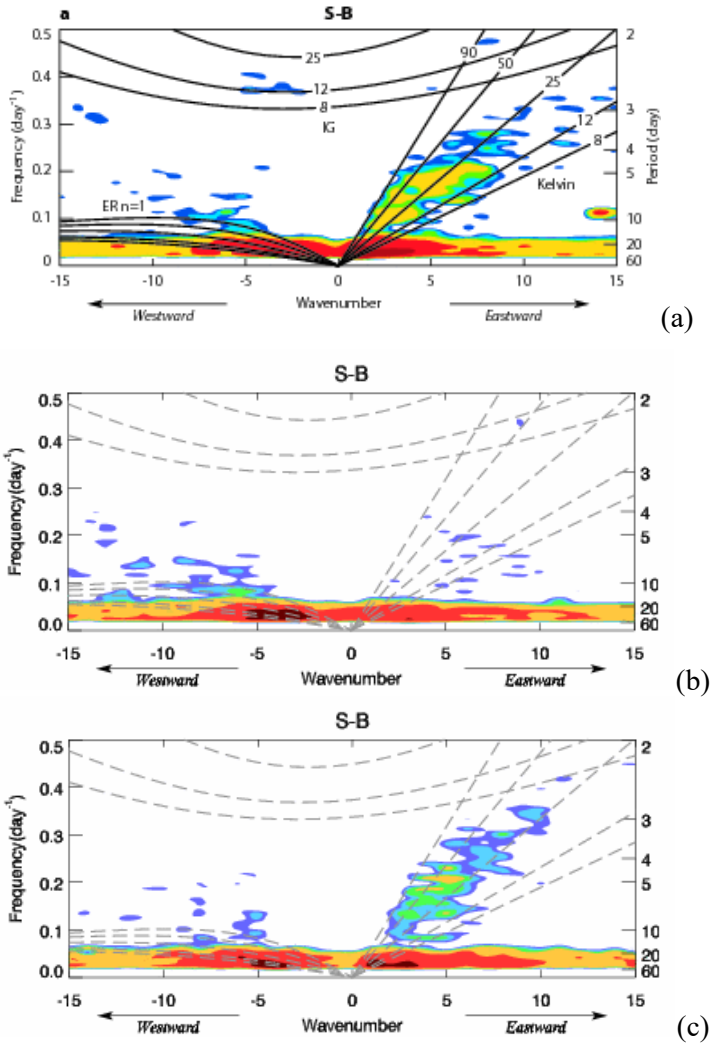

Figure 1.13: Power in the frequency and wavenumber space for the symmetric component of the tropical OLR from (a) NOAA satellite observations, and from an ensemble of 1-year integrations with (b) the IFS cycle 31R1 (operational in 2006 and used in the ERA-Interim), and (c) Cy38r1 (operational 2012/13) with among other things a thoroughly revised convection . "Symmetrical tropical" means here that the quantity has been averaged over the 15S-15N latitude band. Also superposed are the theoretical dispersion curves as function of equivalent depth h (see Appendix) for westward moving equatorial Rossby waves (ER), eastward moving Kelvin waves, and inertia-gravity waves (IR). Kelvin waves behave like gravity waves, where the phase speed $c=\omega/k=(g\ h)^{1/2}$. Wave program courtesy King-Fai Li.

1.4 Midlatitude Convection and its synoptic and orographic forcing

The title obviously implies that midlatitude precipitating convection is synoptically forced which is certainly not the whole truth, but a good starting point. The reason is that the occurrence of intense precipitating convection requires the continuous conversion of potential energy in kinetic energy of the convective draughts, where the potential energy can only be supplied by continuous large-scale destabilization (lifting) of the atmosphere, or to a smaller extent by strong surface fluxes, e.g. when very cold air is advected over warm seas.

A climatology of central southern European rainfall as provided by Frei and Schär (1998) indicates that most intense precipitation with values above 3 mm day^{-1} or 1000 mm $year^{-1}$ occurs in the vicinity of high

orography, especially around the Mediterranean (Figure 1.14a). A large part of the precipitation in these regions is due to synoptically forced mesoscale convective systems (MCSs), principally during autumn. A study by Morel and Sénési (2001) using infrared satellite imagery to identify the regions where deep convective systems, covering a certain area, form (are "triggered") confirms the role of the orography. However, intense convection only occurs under favourable synoptic conditions, where the orography only provides some additional lifting or elevated heating to overcome possible stable layers near cloud base (see later discussion in Section 1.5).

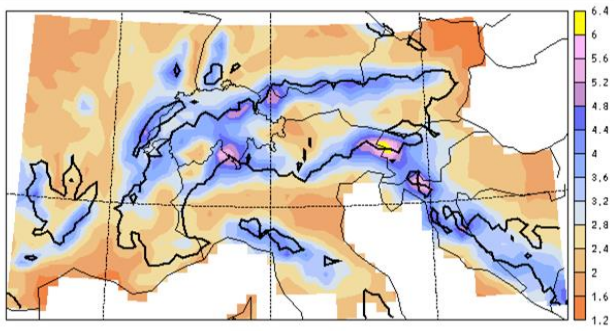

Figure 1.14:a Rainfall climatology (mm day^{-1}) for the south central European region as established by Frei and Schär (1998).

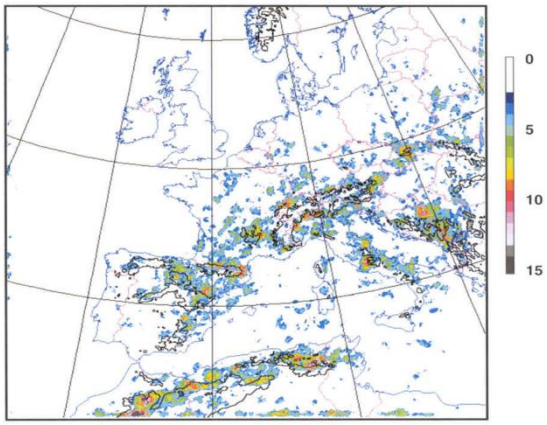

Figure 1.14: b Density map of the triggering of mesoscale convective systems as obtained from satellite infrared imagery by Morel and Sénési (2001).

The synoptic forcing of convection in midlatitudes can be described with the aid of two concepts, the potential vorticity (PV), and the Jets and associated circulations. Both concepts/quantities also prove extremely useful for forecasters in identifying and forecasting convective activity on synoptic charts. The concept of PV defined as

$$PV = (\xi + f)\frac{\partial \theta}{\partial P}, \tag{1.2}$$

where ξ is the relative vorticity, has first been developed by C. Gustav Rossby and colleagues in 1938, and later extended by Hoskins et al. (1985). PV has the following useful properties: i) it is conserved in frictionless and adiabatic motion, where on constant θ surfaces it is advected like a passive tracer, and ii) its field shows more structure than the more "traditional" but equivalent approach of considering the geopotential height on constant pressure surfaces.

An upper-tropospheric positive vorticity anomaly, typical for northern hemispheric synoptic perturbations is illustrated in Figure 1.15. As we know from synoptic meteorology there is ascent (positive vorticity advection, ascending branch of ageostrophic circulation) to the east of the trough (Figure 1.15a), and therefore a favorable area for convective forcing. But also, as seen from Figure 1.15 the region below the anomaly ("inside the trough") has a less stable stratification with relatively warm air in the lower layers and relatively cold air in the mid- and upper troposphere. Therefore, despite weaker dynamical forcing this region will also be conducive to convective development, especially in the presence of strong surface fluxes over relatively warm ocean waters.

PV anomalies are often associated with Jets. However, it is important to consider separately the strong forcing that Jet dynamics associated with the thermal wind balance or horizontal temperature gradient provide for convection. A Jet stream with colder air to the left and warmer air to the right of its axes is depicted in Figure 1.16. Furthermore, the ageostrophic vertical circulations at the entrance and exit region of the Jet have also been depicted. These can be simply explained as follows: at the entrance/exit region of the Jet an acceleration/deceleration takes places which is given by the ageostrophic wind: $du/dt = f\left(v - v_g\right) = fv_a$, where u is the wind component along the Jet axes, and v_a is the ageostrophic wind perpendicular to the Jet axes. Another interesting explanation is to interpret the ageostrophic circulations as the conversion of potential energy in kinetic energy of the Jet in the entrance region, and from kinetic energy in potential energy in the exit region. The two ascending branches of the ageostrophic circulations (marked by + signs in Figure 1.16), i.e. the right entrance region and the left exit region of the Jet constitute favourable regions for deep convection to occur. However, the strongest forcing of convection occurs in the left exit region, where the ageostrophic circulation is thermally direct, i.e. from warm to cold at low levels.

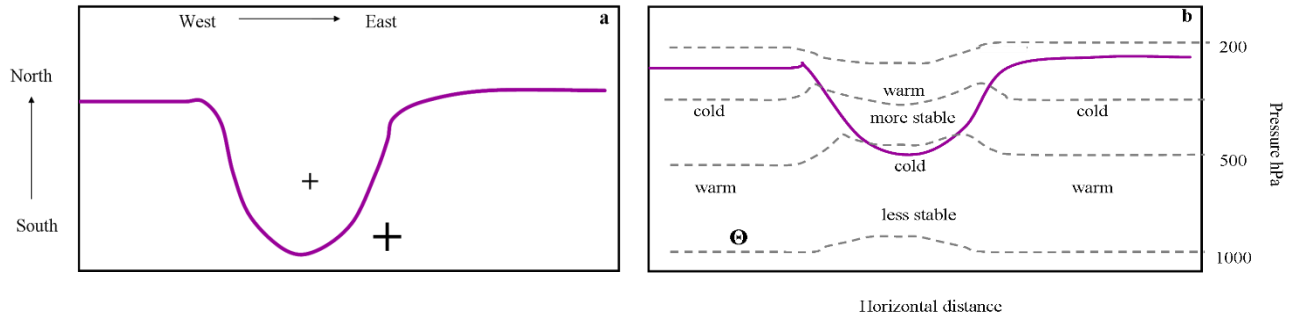

Figure 1.15: Schematic of an upper-level positive PV anomaly in the northern hemisphere in (a) a horizontal plane on a constant θ surface (typically 330 K is used), and in a vertical section (b). Favorable areas for convection are denoted by the + signs in (a), and by the "cold and less stable" area in (b), where the thick solid line can be considered as a PV isocontour and the tropopause height. (Adapted from Bluestein)

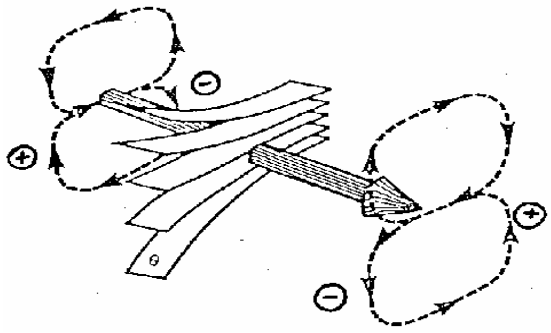

Figure 1.16: Schematic of a Jetstream and associated ageostrophic circulations at the entrance and exit regions. The cold air is to the left of the Jet axes and the warm air to the right, regions of potential convective forcing are denoted by + signs.

The forcing mechanisms of midlatitude deep convection discussed so far should become clearer when looking at case studies of convective events. Two severe deep convective events are shown in Figure 1.17, one that occurred over south-eastern France 9 September 2002 bringing 800 mm rain in 24 h (Figure 1.17a, b), and one that occurred over central North America 5 June 2003 and was associated with several MSCs producing Tornadic storms (Figure 1.17c,d). Infrared satellite images have been overlaid with analysis of PV

at 330K, horizontal wind at 250 hPa (Figure 1.17a,c), or horizontal wind at 925 hPa and equivalent potential temperature $\theta_e = \theta \exp\left(L_v q / c_p T\right)$ at 850 hPa (Figure 1.17b,d). Note that in the definition of θ_e, L_v is the latent heat of vaporisation, $L_v(T = 273K) = 2.5008 \times 10^6$ K J kg^{-1}, q is the specific humidity, c_p= 1004.71 J kg^{-1} is the specific heat of dry air, and T is temperature (to be very precise it would be the temperature at cloud base level).

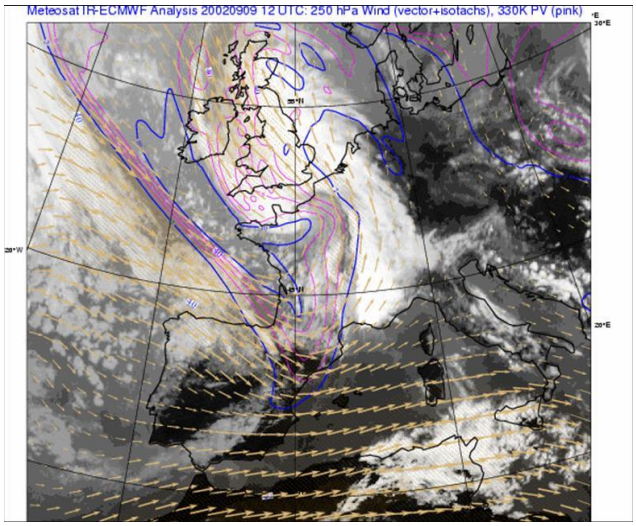

Figure 1.17a Meteosat infrared image for western Europe from 9 September 2002 12 UTC, and ECMWF analysis: PV at 330 K (pink and blue isolines) and 250hPa wind vectors and isotachs (shaded beige)

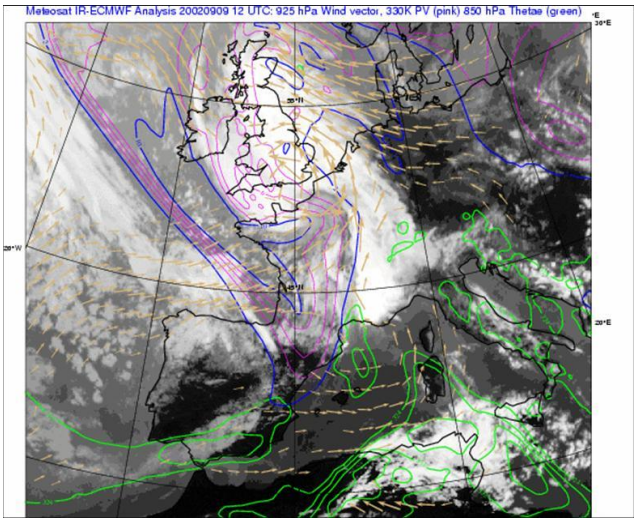

Figure 1.17b. Same as 1.16a but with analysis of 925hPa wind vectors and 850 hPa θe (green isolines).

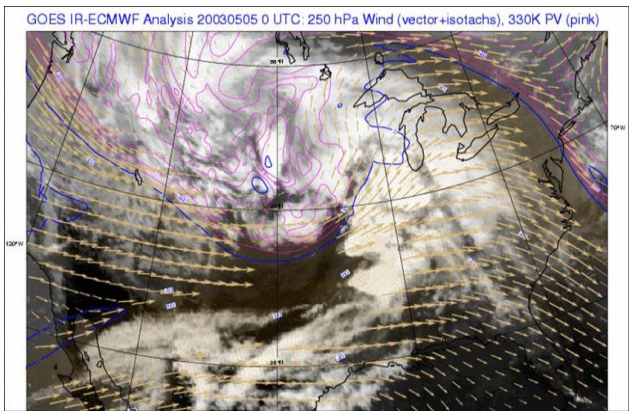

Figure 1.17c GOES infrared image for North America from 5 May 2003 00 UTC, and ECMWF analysis as in Figure 1.14.

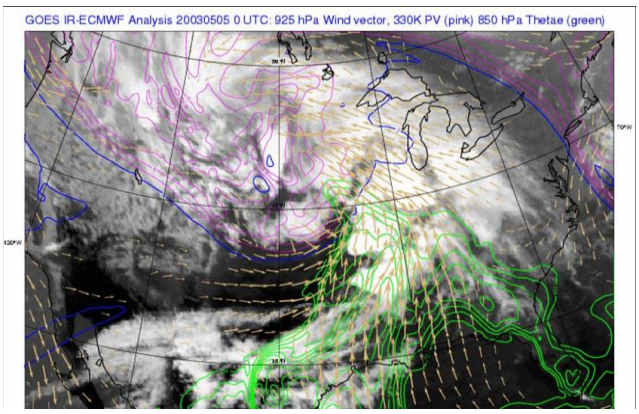

Figure 1.17d Same as Figure 1.14c, but with analysed fields as in Fig. 12b.

In both cases there is a strong PV anomaly or PV "streamer" with an upper-level Jet at the western flank of the anomaly. Furthermore, in both cases the southern dip of the anomaly coincided with the exit region of a weak subtropical Jet in Figure 1.17a, and a very strong subtropical Jet in Figure 1.17c. The intense convection organized in MSCs forms at the south-eastern flank of the anomaly below the upper-level divergent zone of the Jet; weaker convection is found in the centre of the anomalies. At the same time at low levels there is strong convergence and advection of moist and humid air from Africa/Mediterranean

(Figure 1.17b), and from the Mexican Golf (Figure 1.17d), respectively that together with the upper-level cold advection and divergence forms the classical picture of strong synoptic forcing of intense midlatitude convection. More on these cases can be found in the *ECMWF Newsletter* summer 2003.

1.5 The diurnal cycle of convection

Another important feature of the convection is a pronounced diurnal cycle in the tropics and the middle latitudes during the summer season. The diurnal cycle is primarily controlled by a change of vertical stability and moisture that arises as solar insolation heats the earth's surface, and subsequently the atmosphere through diurnal variations in the surface fluxes, leading to the development of convection. Over land most observational studies, and also experimental studies using e.g. cloud resolving models, show that precipitation tends to occur in the afternoon or late evening. A typical diurnal evolution of surface latent and sensible heat fluxes and precipitation as a function of local solar time is depicted in Figure 1.18. Whereas the surface heat and moisture fluxes show a sinusodial curve peaking around local noon, the peak in surface precipitation occurs in the (late) afternoon. As discussed in e.g. Chaboureau et al. (2004) or Bechtold et al. (2014) the reasons for the roughly three hour delay between the surface flux and precipitation peaks might be explained as follows: shallow cumulus clouds already form in the early morning, followed by deeper still non-precipitating cumulus congestus around noon that transport moisture from the boundary-layer in the lower free troposphere. Once these clouds have sufficiently moistened the lower free troposphere, which in cases of a marked diurnal cycle is only weakly synoptically forced and therefore marginally stable, more and more and larger penetrating updraughts might develop. However, it will take further time of O(1000 s) until these updraughts grow to a precipitating stage, and further time until precipitation reaches the surface. Cold pool dynamics also play a role in the later stages of convective systems.

The diurnal cycle can be globally assessed using either infrared satellite observations of the OLR (cold cloud tops) or retrievals from the Tropical Rainfall Measurement Mission (TRMM) precipitation radar or microwave radiometer. The phase and amplitude of the diurnal cycle can be evaluated from a 1-hourly

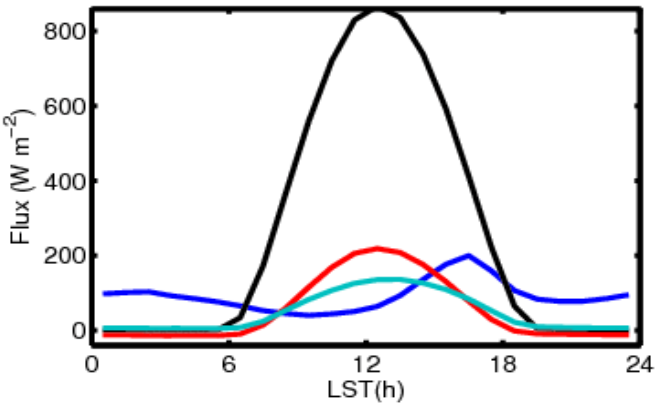

Figure 1.18: Typical daily evolution over Sahel region during JJA of surface insolation (black), latent (light blue) and sensible (red) heat fluxes and the total precipitation (dark blue line) as function of local solar time. All units are in W m^{-2}.

binned diurnal composite dataset by fitting a sine wave. Figure 1.19a shows the amplitude of the diurnal cycle (mm day^{-1}) over the tropics. The amplitude, while being much stronger over land with values exceeding 10 mm day^{-1} the amplitude, is significant both over tropical ocean and land. The phase is plotted in Figure 1.20. Over land, in particular the Amazonia, tropical Africa, India and Indonesia, radar derived rainfall rates (Figure 1.20a) indicate maximum rainfall that roughly occurs during late afternoon, early

evening though exhibiting important regional variability. In contrast, maximum rainfall rates over the tropical oceans occur during the late night and early morning hours (cloud radiative effects with infrared cooling of cloud tops and cloud base heating by surface fluxes), but again showing significant regional variations in particular close to major land masses (convective systems advected from inland), but probably also variations related to the main monsoon systems (see also Yang and Slingo, 2001).

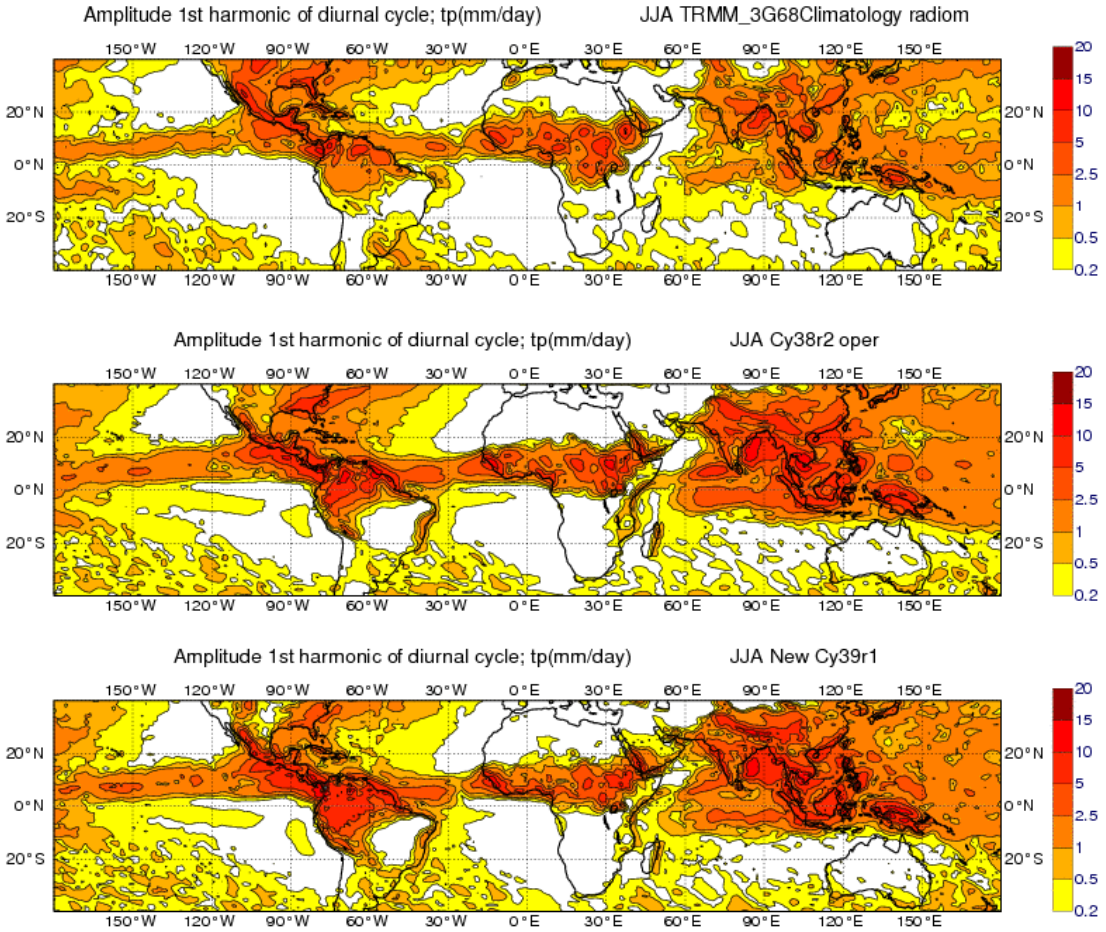

Figure 1.19: Amplitude of the diurnal cycle of precipitation (mm/day) for JJA as obtained from a 15-year climatology with the TRMM radar (courtesy Yukari Takayabu and colleagues), and as obtained from a 4-member ensemble of seasonal T159 integrations with Cy38r2 (operational 2012/13) and the experimental forthcoming Cy39r1. Amplitude and phase are computed from the first harmonic of a Fourier decomposition (courtesy A. Beljaars for the diurnal cycle software). More model against observation comparisons on:
http://www.ecmwf.int/products/forecasts/d/inspect/catalog/research/physics_clim/

Global models using convective parametrizations tend to reasonably represent the amplitude of the diurnal cycle, but have problems with the phase over land (Slingo et al. 1992; Bechtold et al. 2004; Clark, 2007) in that they typically produce maximum precipitation in phase with the surface fluxes (amplitude and phase) peaking around local noon. In contrast, cloud resolving models with horizontal resolutions of O(1 km) are able to correctly reproduce the phase of the diurnal cycle over land (Petch et al. 2002; Clark et al. 2007).

Figures 1.19b and 1.20b show that while the operational IFS in 2013 reasonably reproduces the amplitude of the diurnal cycle, it produces maximum precipitation over land that leads the observations by 4-5 hours. Is there a solution to this problem? A lot of trials have been made in the past on entrainment, prognostic formulations etc. And yes, as described in Bechtold et al. (2014) and also Chapter 3.7 there is a simple and elegant solution as an extension to the current IFS convection scheme that allows for a largely improved representation of the diurnal cycle (Figures 1.19c and 1.20c).

This formulation became operational in November 2014. Representing the dynamics of convective systems during night remains however a problem with convection parametrizations.

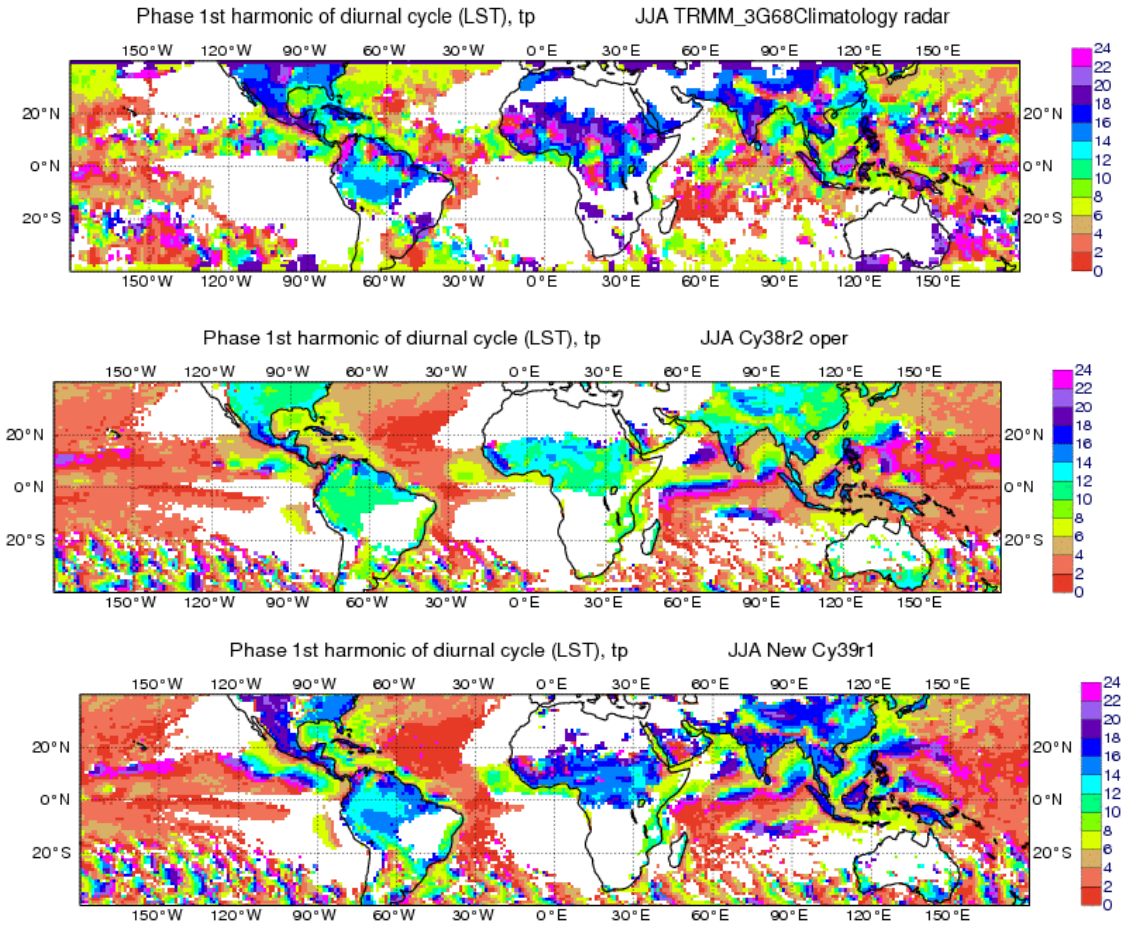

Figure 1.20: Same as in Figure 1.19, but for the phase (LST).

1.6 Buoyancy and the parcel or plume method

So far a synoptic view of convection has been developed, and it is now time to present the basic tools that allow for a more quantitative description of convective processes and their feedback on the large-scale.

1.6.1 Buoyancy

Convective motions have been defined as buoyant motions in a stratified fluid. The force on a parcel immersed in a fluid under the action of gravity can be simply derived from Figure 1.21, where we assume that both the parcel and the fluid do not move. With $A = \Delta x \Delta y$ the hydrostatic pressure force on the top surface of the cubic parcel is $F_{top} = -g\rho_2 h_1 A$, and the pressure force at its bottom is $F_{bot} = g\rho_2 h_2 A$. The total force on the parcel is the sum of the pressure and gravity forces

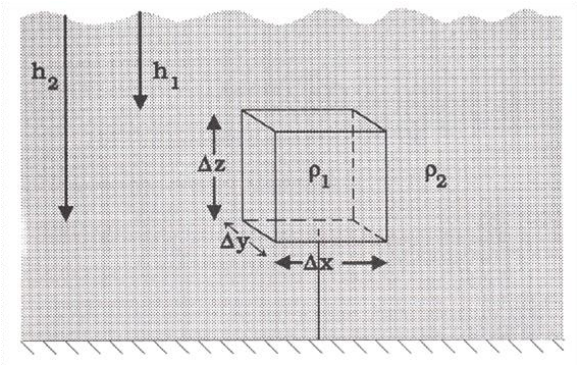

Figure 1.21: Parcel immersed in a fluid with different

$F_{tot} = F_{top} + F_{bot} + F_{grav} = g\rho_2(h_2 - h_1)A - g\rho_1 \Delta z\, A$, so that the acceleration of the parcel is given by

$$\frac{F_{tot}}{m_1} = \frac{g(\rho_2 - \rho_1)A\Delta z}{A\Delta z \rho_1} = \frac{g(\rho_2 - \rho_1)}{\rho_1}. \tag{1.3}$$

This is called the buoyancy acceleration.

Turning now to the full vertical momentum equation of a fluid parcel

$$\frac{dw}{dt} = -\frac{1}{\rho}\frac{\partial p}{\partial z} - g, \tag{1.4}$$

and splitting the pressure and the density in a basic state hydrostatic contribution denoted by overbars, and perturbations denoted by primes, i.e.

$$p = \bar{p} + p'; \quad \rho = \bar{\rho} + \rho'; \quad \frac{\partial \bar{p}}{dz} = -\bar{\rho} g \tag{1.5}$$

one obtains

$$\frac{dw}{dt} = -\frac{1}{\bar{\rho} + \rho'}\frac{\partial(\bar{p} + p')}{\partial z} - g \approx \frac{1}{\bar{\rho}}\frac{\partial \bar{p}}{\partial z} - \frac{1}{\bar{\rho}}\frac{\partial p'}{\partial z} - g + \frac{\rho'}{\bar{\rho}}\frac{1}{\bar{\rho}}\frac{\partial \bar{p}}{\partial z} + \frac{\rho'}{\bar{\rho}}\frac{1}{\bar{\rho}}\frac{\partial p'}{\partial z}, \tag{1.6}$$

where it has been assumed that

$$\frac{1}{\bar{\rho} + \rho'} \approx \frac{1}{\bar{\rho}}\left(1 - \frac{\rho'}{\bar{\rho}}\right). \tag{1.7}$$

As the first term of the rhs in (1.6) is equal to *g* it cancels with the third term; and if we neglect the last term as it includes a product of perturbations we get the simplified momentum equation

$$\frac{dw}{dt} = -\frac{1}{\bar{\rho}}\frac{\partial p'}{\partial z} - \frac{\rho'}{\bar{\rho}}g, \tag{1.8}$$

where the first term of the rhs is an acceleration due to a non-hydrostatic pressure force, and the second term is the buoyancy acceleration *B*. Now, in the case of a parcel corresponding to dry air the buoyancy acceleration itself contains a contribution due to pressure and one due to temperature as follows from the ideal gas law

$$\rho = \frac{p}{R_d T} \rightarrow \rho' = \frac{p'}{R_d \bar{T}} - \frac{\bar{p}T'}{R_d \bar{T}^2} \rightarrow \frac{\rho'}{\bar{\rho}} = \frac{p'}{\bar{p}} - \frac{T'}{\bar{T}}, \tag{1.9}$$

where R_d = 287.06 J kg^{-1} K^{-1} is the gas constant for dry air. In general, the pressure perturbation term is much smaller than the temperature perturbation term (precisely if the air parcels speed is much less than the speed of sound) so that we can further simplify the vertical momentum equation to

$$\frac{dw}{dt} \approx -\frac{1}{\bar{\rho}}\frac{\partial p'}{\partial z} - \frac{T'}{\bar{T}}g. \tag{1.10}$$

Finally, in order to obtain the buoyancy acceleration in the case of moist air one has to replace the temperature by the virtual temperature $T_v = T(1+\alpha q - q_l)$, with q and q_l the specific humidities of water vapour and total condensate, respectively, and $\alpha = (1-\varepsilon)/\varepsilon = 0.608; \varepsilon = R_d / R_v$ with R_v = 461.525 J kg^{-1} K^{-1} the gas constant for water vapour. Then one approximately obtains

$$B = -g\frac{\rho'}{\bar{\rho}} \approx -g\left(\frac{T'}{\bar{T}} + \alpha q' - q_l\right). \tag{1.11}$$

To give an idea of the magnitude of the different terms in (1.11), a temperature perturbation of 1 K is equivalent to a moisture perturbation of 5 g kg^{-1} or a change in the condensate loading of 3 g kg^{-1}. The approximate equilibrium in (1.10) between the non-hydrostatic pressure gradient acceleration and the buoyancy is illustrated in Figure 1.22. In short, a positively buoyant upward moving parcel experiences a non-hydrostatic pressure force that is directed downward, as its pressure perturbation is positive on its upper side and negative at its lower side.

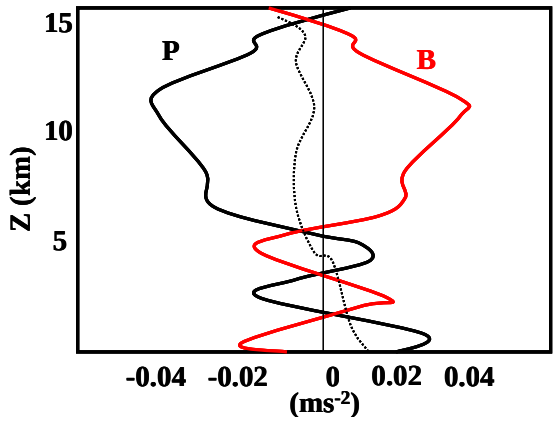

Figure 1.22a. Equilibrium between buoyancy and pressure gradient acceleration as obtained from CRM simulations of deep convection. (After Guichard 1998)

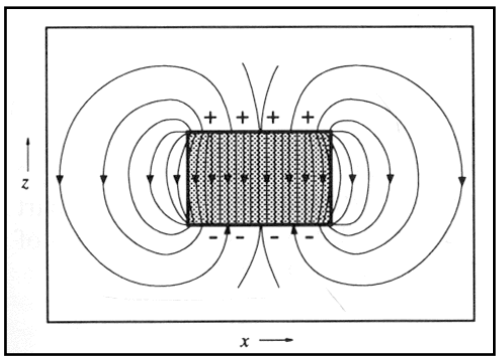

Figure 1.22b. Vector field of the buoyancy pressure gradient force .(After Houze 1993).

1.6.2 Convective Available Potential Energy (CAPE)

The Convective Available Potential Energy is defined as the vertical integral of the buoyancy between cloud base and cloud top

$$CAPE = \int_{base}^{top} B dz = \int_{base}^{top} g \frac{T_v^c - T_v^e}{T_v^e} dz = \int_{P_{top}}^{P_{bot}} R_d (T_v^c - T_v^e) d \ln p, \tag{1.12}$$

where superscripts *c* denote cloudy values and superscripts *e* denote environmental values, respectively. (1.12) expresses CAPE in both height and pressure vertical coordinates is given (R_d is the gas constant of dry and not moist air as the moist effects are already accounted for in T_v). If one wants to estimate CAPE from a thermodynamic diagram *T(p)* as in Figure 1.23, the formulation in pressure coordinates is particularly useful. CAPE is then obtained as the area enclosed by the moist adiabat through cloud base which corresponds to the lifting condensation level (LCL), and the environmental temperature profile. It is often observed that the level of free convection (LFC) lies above the LCL, as there is some area of stable stratification or convective inhibition (CIN) near cloud base. This stable layer near cloud base is an essential feature of moist convection as it allows CAPE to be stored above, without being immediately removed through mixing by convective draughts. Furthermore, as CAPE represents the potential energy a parcel, lifted to its LFC acquires during ascent to the level of neutral buoyancy (LNB), i.e. the level where its virtual temperature becomes smaller than that of the environment (Figure 1.23), the corresponding kinetic energy or updraught velocity of the parcel can be estimated from the one-dimensional momentum equation as follows

$$\frac{dw}{dt} = w\frac{dw}{dz} = \frac{1}{2}\frac{dw^2}{dz} \approx g\frac{T_v^{'}}{\overline{T}_v} \approx g\frac{T^c - T^e}{T^e}, \tag{1.13}$$

where for simplicity T_v has been replaced by T. Integrating over z one obtains

$$\int_0^z \frac{1}{2}\frac{dw^2}{dz} dz = \frac{1}{2} w^2(z) = \int_0^z g\frac{T^c - T^e}{T^e} dz = CAPE \tag{1.14}$$

$$w = \sqrt{2CAPE}.$$

To fix the ideas assume the environmental temperature, and the cloud environment temperature perturbation constant, i.e. T^c =250 K, $T^c - T^e$=5K, and z=10 km which gives w=60 m s^{-1}. But this is a very high value that has been only observed in extreme events like Tornadic storms; updraught velocities are more likely to be in the range between 5 and 25 m s^{-1}, so what is wrong? This is investigated in the next subsection.

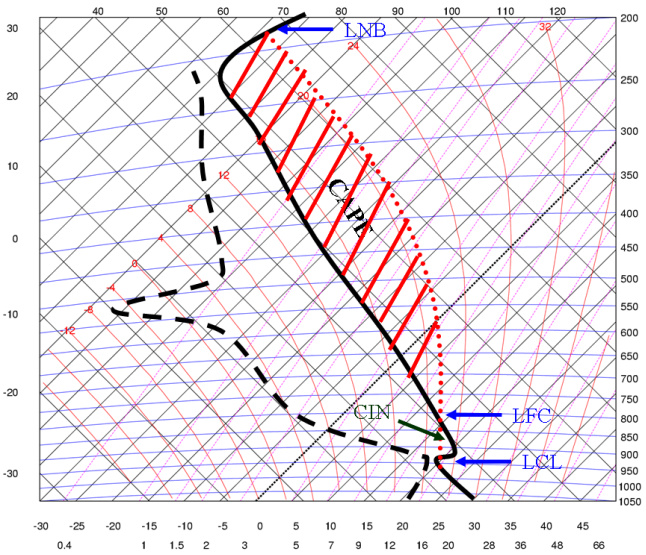

Figure 1.23: CAPE in Tephigram as obtained as the area between the moistadiabat through cloud base and the environmental T. LCL denotes the lifting condensation level, LFC the level of free convection, CIN is the convective inhibition= "negative CAPE between the LCL and the LFC ", and LNB is the level of neutral buoyancy.

Before, let us briefly consider an alternative and efficient way to estimate CAPE making use of $\theta_e(T,q,p) = \theta \exp(L_v q / c_p T)$ a quantity that is conserved during moist adiabatic ascent (and also when precipitation processes are involved) and $\theta_{es}(T,p) \approx \theta \exp(L_v q_s(T) / c_p T)$, the saturated equivalent potential temperature (Betts and Dugan, 1973) , which at a given pressure level is a function of *T* only. Note that even if not necessary for our applications, strictly speaking c_p and θ should be replaced by their values for moist air in the definitions of θ_e and θ_{es}, i.e.

$c_{pm} = c_p + r c_{pv} = (1-q)c_p + q c_{pv}$; $R_m = (1-q)R_d + qR_v$; $\theta = T(p_0 / p)^{R_m / c_{pm}}$, with c_{pv} =4 R_v =1846.1 J kg^{-1} the specific heat for water vapour, and *r* the vapour mixing ratio.

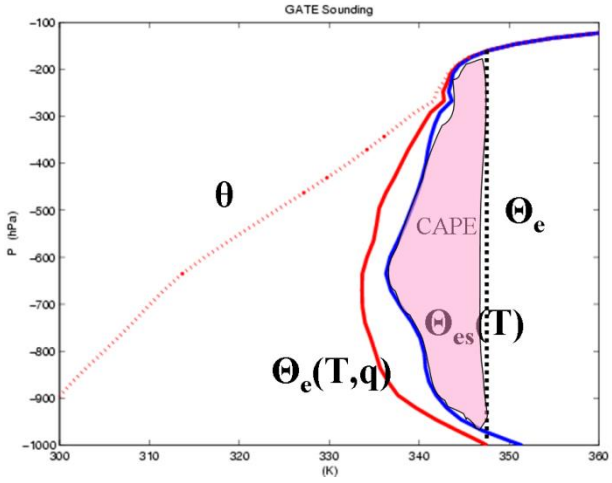

Figure 1.24: Convective sounding from the GARP Atlantic Tropical Experiment (GATE) with θ_e (red solid line), θ (dotted red line) and θ_{es} (blue line). CAPE corresponds to the area laying between θ_e from the subcloud layer (black line) and θ_{es}.

In Figure 1.24 are drawn profiles of θ, θ_e, and θ_{es} during an active convective period of the GARP Atlantic Tropical Experiment (GATE). An important characteristic of the tropical troposphere is that both θ_e, and θ_{es} are minimum in the mid-troposphere. The CAPE of the sounding in Figure 1.24 is obtained as the area between the constant ϑ_e line of an air parcel originating in the boundary-layer, conserving its ϑ_e, and the ϑ_{es} profile of the environment

$$CAPE \approx \int_{base}^{top} g \frac{\theta_e^b - \theta_{es}^e}{\theta_{es}^e} dz, \tag{1.15}$$

where θ_e^b is constant and represents θ^e at the parcels departure level; typically an average value over the lowest 100 or 500 m or 20 to 60 hPa of the boundary-layer is used. Note that (1.15) produces values that are roughly 25% larger than those obtained with (1.12). With the aid of Figure 1.24 one can easily recognize another important feature of oceanic convection in particular, i.e. there is no or only very small CAPE for parcels departing above the boundary-layer - in the present case parcels departing above 900 hPa have θ_e lower than 338 K which is lower than the minimum mid-tropospheric θ_{es}.

In the definitions (1.14) and (1.15) of CAPE no mixing of the parcels with the environment has been taken into account, i.e. the ascent is supposed to be adiabatic (no mass and energy is exchanged with the environment). Also, the effect of water loading is included in (1.12) but not in (1.14)-(1.15), where it is assumed that all condensed water falls out as precipitation, i.e. the process is assumed to be pseudo-adiabatic - a reasonable approximation. Overall, the processes of mixing and water loading will decrease the CAPE, whereas the inclusion of processes related to freezing of drops and sublimation (implicitly accounted for in the computation of T^c in (1.12), but not in (1.15) and also not accounted for in a Tephigram) generally produces slightly higher CAPE values .

1.6.3 Mixing

The most important process affecting the parcel properties is the mixing, or the exchange of mass between the air parcel and the environment. The mixing occurs through the engulfment of environmental air into the cloud as a result of turbulent motions, thereby increasing the mass of the cloud. As the environmental air is generally drier than the ascending plume, evaporation and evaporative cooling results from the mixing (entrainment) process, and then might further enhance the turbulent motions. The mixing of the cloud with the environment through turbulent flow is clearly visible in high-resolution numerical simulations of cumulus clouds (Figure 1.25a). Whereas the cloud base region in Figure 1.25a appears quasi flat, the two main ascending towers are strongly distorted by the flow. Note also that only the left updraught appears to be connected to ascending motion below cloud base, whereas the right updraught appears to be “disconnected” from the motions in the subcloud layer.

In the past different idealised schemes have been utilized to account for the mixing process in simple one-dimensional models representing a single or multiple cumulus updraughts. The principal mixing representations are illustrated in Figure 1.25b with from left to right: an undiluted ascent, a plume that is entraining all its way to the equilibrium temperature level or cloud top level, a plume that is only entraining at cloud top, and last multiple plumes where at each level mixing takes place leading to new updraughts. Recent numerical simulations, however, (e.g. Heus et al. 2008) suggest that actual mixing occurs laterally in form of turbulent mixing across the cloud edges (causing evaporation and sinking motion) and dynamically driven organized mixing (inflow) behind the “head” of the rising plume as also evident from Figure 1.25a.

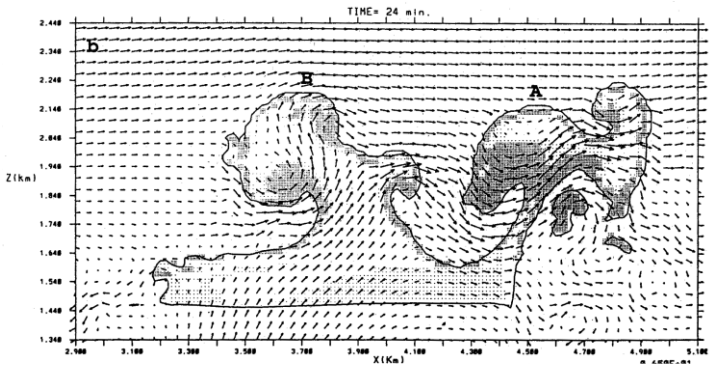

Figure 1.25a. Very high resolution simulation of a cumulus cloud. (After Vaillancourt et al. 1997.

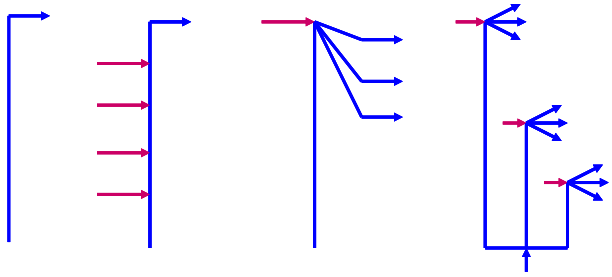

Figure 1.25b. Idealized models of an ascending cloudy plume and the mixing with the environment. From left to right: undiluted ascent, entraining plume, cloud top entrainment, stochastic mixing.

Finally, the effect of mixing on the pseudo-adiabat through cloud base and the CAPE is illustrated in Figure 1.26. Mixing not only reduces the temperature difference between the cloud and the environment it can also reduce the maximum height to which a parcel can ascent or even suppress convection entirely if the environment is very dry (Zhang and Mc Farlane 1991). Therefore, via the effect of mixing and buoyancy moisture acts as a strong regulator on atmospheric convection (Tompkins 2001; Redelsperger et al. 2002).

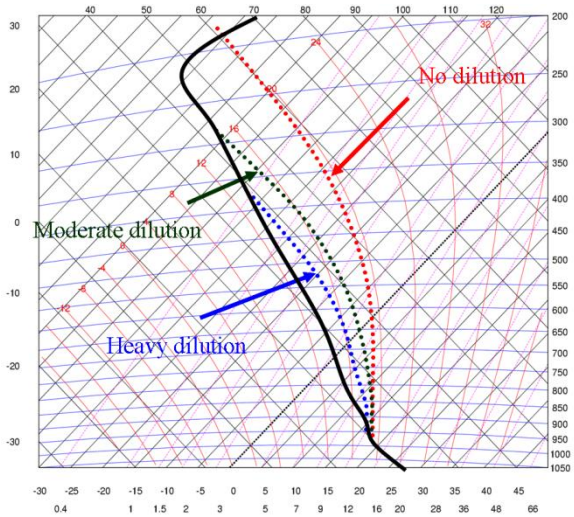

Figure 1.26: Tephigram showing the influence of mixing on the pseudo-adiabats through cloud base, and the height of the level of neutral buoyancy.

1.7 Large-scale effects of convection

1.7.1 Q1,Q2 and Q3

Convection implies motions that are highly variable in space and time. It is therefore difficult to "measure" convection. However, one can measure, and also parameterize, the ensemble effect of the convective motions on the large-scale.

Following Yanai et al. (1973) the ensemble or bulk effect of convection on the large-scale can be conveniently derived from the basic equations of motion in pressure coordinates using the dry static energy $s = c_p T + gz$, and specific humidity *q;* recall that *s* is approximately conserved in dry adiabatic hydrostatic motions. The basic thermodynamic and dynamic equations write

$$\begin{aligned}
&\frac{\partial s}{\partial t} + \nabla\vec{v}_h s + \frac{\partial \omega s}{\partial p} = Q_R + L_v(c-e),\\
&\frac{\partial q}{\partial t} + \nabla\vec{v}_h q + \frac{\partial \omega q}{\partial p} = -(c-e)\\
&\frac{\partial \vec{v}_h}{\partial t} + \nabla\vec{v}_h\vec{v}_h + \frac{\partial \omega \vec{v}_h}{\partial p} + \nabla\Phi + f\,k\times\vec{v}_h = 0
\end{aligned} \tag{1.16}$$

where $\vec{v}_h$ is the horizontal wind vector, ω is the vertical motion in pressure coordinates, Q_R is the radiative heating rate, Φ is the geopotential, and *c* and *e* represent the condensation and evaporation rates, respectively. Averaging these equations over an area *A* such that

$$\bar{\chi} = \frac{1}{A}\int_A \chi dA; \quad \chi = \bar{\chi} + \chi' \tag{1.17}$$

one obtains

$$\begin{aligned}
&\underbrace{\frac{\partial \bar{s}}{\partial t} + \bar{\vec{v}}_h\nabla\bar{s} + \bar{\omega}\frac{\partial \bar{s}}{\partial p}}_{\text{large-scale}\quad\text{observable}} = \bar{Q}_R + \underbrace{L_v(\bar{c}-\bar{e}) - \frac{\partial \overline{\omega' s'}}{\partial p}}_{\text{subgrid}\quad\text{convective}}\\
&\underbrace{\frac{\partial \bar{q}}{\partial t} + \bar{\vec{v}}_h\nabla\bar{q} + \bar{\omega}\frac{\partial \bar{q}}{\partial p}}_{\text{large-scale}\quad\text{observable}} = \underbrace{-(\bar{c}-\bar{e}) - \frac{\partial \overline{\omega' q'}}{\partial p}}_{\text{subgrid}\quad\text{convective}}\\
&\underbrace{\frac{\partial \bar{\vec{v}}_h}{\partial t} + \bar{\vec{v}}_h\nabla\bar{\vec{v}}_h + \bar{\omega}\frac{\partial \bar{\vec{v}}_h}{\partial p}}_{\text{large-scale}\quad\text{observable}} = \underbrace{-\frac{\partial \overline{\omega'\vec{v}_h'}}{\partial p}}_{\text{subgrid}\quad\text{transport}},
\end{aligned} \tag{1.18}$$

where the lhs represent the large-scale or observable quantities, and the terms of the rhs represent the subgrid-scale motions and microphysical processes, respectively that in convective regions will be dominated by convection[1]. Correlations implying fluctuations of the horizontal wind have been neglected in (1.18). Equations similar to (1.18) can also be derived for momentum. Historically, the rhs of these equations have been given the denominations

[1] The equation for *s* is not exact as *s* is energy and therefore production of kinetic energy should be included; a more accurate form of the energy equation is obtained replacing *s* by θ.

$$
\begin{aligned}
Q_1 &\equiv Q_R + L_v(\overline{c} - \overline{e}) - \frac{\partial \overline{\omega' s'}}{\partial p} \\
Q_2 &\equiv L_v(\overline{c} - \overline{e}) + L_v \frac{\partial \overline{\omega' q'}}{\partial p} \\
\vec{Q}_3 &\equiv -\frac{\partial \overline{\omega' \vec{v}_h'}}{\partial p},
\end{aligned}
\tag{1.19}
$$

where Q_1 is called the *apparent heat source*, Q_2 is called the *apparent moisture sink*, and Q_3 the apparent momentum source - attention for historical reasons Q_2 is defined as L_v times the negative of the rhs of the q tendency. The heat sources are called "apparent" because they generally cannot be observed, but as one can measure the large-scale budget (lhs of (1.18)) with the aid of a radiosonde array, they are entirely determined. Useful is also the relation defining the apparent source for the moist static energy $h = s + L_v q$

$$
Q_1 - Q_R - Q_2 = -\frac{\partial \overline{\omega' h'}}{\partial p}. \tag{1.20}
$$

where only the transport term remains. Integrating (1.19) over the vertical between the surface and the top of the atmosphere can be done easily as the flux divergences represent perfect differentials. This leads to the following important budget constraints

$$
\begin{aligned}
\int_{Pt}^{Ps} Q_1 \frac{dp}{g} &\equiv \int_{Pt}^{Ps} Q_R \frac{dp}{g} + L_v \,\mathrm{Pr} + \rho_s c_p (\overline{w'T'})_{P=Ps} = \int_{Pt}^{Ps} Q_R \frac{dp}{g} + L_v \,\mathrm{Pr} + HS \\
\int_{Pt}^{Ps} Q_2 \frac{dp}{g} &\equiv L_v \,\mathrm{Pr} - \rho_s L_v (\overline{w'q'})_{P=Ps} = L_v \,\mathrm{Pr} - HL \\
\int_{Pt}^{Ps} Q_3 \frac{dp}{g} &= F_{Ps}^{frict} - F_{Pt}^{frict} = F_{Ps}^{frict},
\end{aligned}
\tag{1.21}
$$

where *Pr* denotes the surface precipitation flux (kg m^{-2} s^{-1}), *HS* the surface sensible heat flux, *HL* the surface latent heat flux, and ρ_s is the near surface air density. In (1.21) it has been assumed that all fluxes except the radiative fluxes vanish at the top of the atmosphere and $-g^{-1}\left(\overline{\omega' s'}\right)_{P=Ps} \approx \rho_s c_p (\overline{w'T'})_{P=Ps}$. The physical meaning of (1.22) is that i) column integrated heat can only be changed through radiation, surface sensible heat flux, and precipitation, ii) column integrated water vapour can only change through removal by surface precipitation and input by surface moisture flux, iii) total momentum is only changed through surface friction (an external force), therefore convective transport conserves momentum (not kinetic energy !). Furthermore, the constraints (1.22) must be fulfilled by the large-scale measurements to be consistent. Therefore they are also used as strong constraints in variational data assimilation procedures to derive consistent values of Q_1-Q_R, Q_2, Q_3 from large-scale measurement campaigns.

A final word on "convective forcing" in relation to the apparent heat sources is necessary. Generally, it is understood that the "large-scale forcing of convection" only comprises the large-scale advective tendencies, i.e. the last two terms of the rhs of (1.18), and not the Eulerian time derivative of the quantity

$$\left.\frac{\partial \bar{T}}{\partial t}\right|_{forc} = \frac{1}{c_p}\left(\bar{\vec{v}}_h \nabla \bar{s} + \bar{\omega}\frac{\partial \bar{s}}{\partial p}\right) = \frac{1}{c_p}\left(Q_1 - \frac{\partial \bar{s}}{\partial t}\right)$$
$$\left.\frac{\partial \bar{q}}{\partial t}\right|_{forc} = \bar{\vec{v}}_h \nabla \bar{q} + \bar{\omega}\frac{\partial \bar{q}}{\partial p} = -\frac{1}{L_v}Q_2 - \frac{\partial \bar{q}}{\partial t}. \qquad (1.22)$$

Deep convection

Average profiles of Q_1, Q_2 Q_R as obtained during GATE phase III are shown in Figure 1.27. These profiles vary strongly as a function of convective activity. However, the characteristic features of these profiles for deep convective periods in tropical regions are the quasi parabolic shape of Q_1 with a maximum in the middle tropical troposphere around 500 hPa, and a maximum of Q_2 that occurs at lower altitudes around 700-850 hPa. The latter is simply due to the fact that the water vapour content of the troposphere decreases with height so that most condensate is produced in the layers near cloud base. Similar profiles to Figure 1.27 have also been obtained over the tropical West Pacific. Average profiles over the whole tropical belt can be estimated from Figure 1.3 by simply adding the contributions due to convection, turbulent diffusion and "stratiform" clouds.

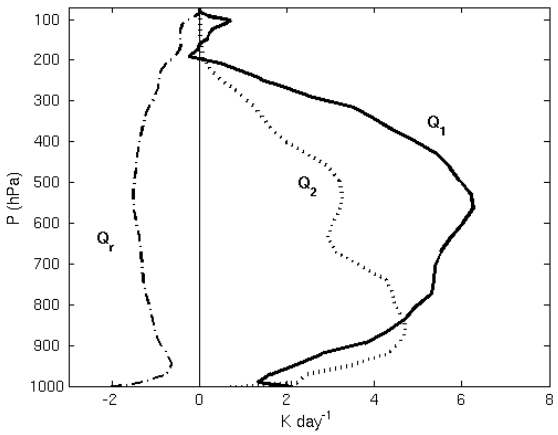

Figure 1.27: Average profiles of Q_1, Q_2 and Q_R from GATE phase III.

Shallow convection

Apparent heat and moisture source profiles for shallow convection in the trade wind region have been derived e.g. by Nitta and Esbensen (1974) for the Barbados Oceanographic and Meteorological Experiment (BOMEX). These are depicted in Figure 1.28 together with modelling results obtained with the IFS. The two plots qualitatively agree in that there is a strong negative peak in Q_2 corresponding to a moistening of the upper part of the cloud layer due to moisture transport and evaporation of cloud water. The evaporation of cloud water also leads to the negative peak of Q_1 in the upper part of the cloud layer, whereas in the sub-cloud layer there is heating due to surface fluxes. The two plots mainly differ in the sub-cloud layer for Q_2, where one expects moistening due to surface fluxes and drying due to upward turbulent moisture transport - the results in Figure 1.28 for this region should therefore be regarded as uncertain.

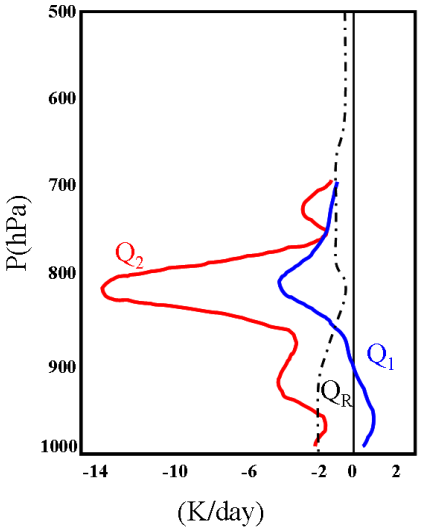

Figure 1.28a Apparent heat and moisture sources as derived by Nitta and Esbensen (1974) for BOMEX cumuli.

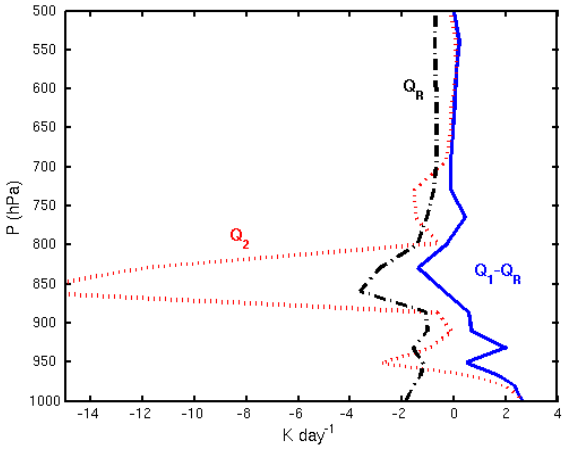

Figure 1.28b. Same as (a), but derived from IFS single column model simulations of BOMEX.

Condensation and transport

Following (1.19) convection affects the large-scale environment through condensational (evaporation) heating (cooling), and transport. The contribution of each process can be readily evaluated with the aid of CRM simulations, e.g. the condensational heating/cooling rates are obtained as the domain average microphysical tendencies of the model, and the transport terms are derived as divergence of the "eddy" or "convective" fluxes computed as

$$\overline{\omega'\chi'} \approx -g\bar{\rho}\sum_{i=1}^{n}\left(w^i-\bar{w}\right)\left(\chi^i-\bar{\chi}\right), \tag{1.23}$$

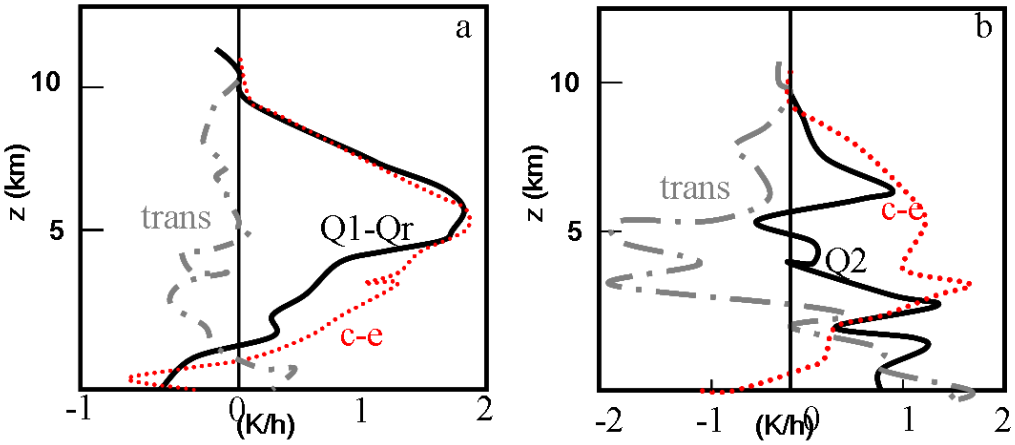

Figure 1.29: Contribution of the transport and condensation-evaporation to the Q_1-Q_R and q2 budgets for the case of a squall line. (Reproduced after Caniaux et al. 1994).

where bars denote horizontal domain averages, *n* the total number of horizontal grid points, and *w* the vertical velocity in z coordinates as used by most CRMs. Using a similar procedure Caniaux et al. (1994)

computed the contribution of the transport and condensational heat to the Q_1 and Q_2 budget, respectively for a squall line case (Figure 1.29). The important information from Figure 1.29 is that the Q_1 budget is dominated by the condensational heating, meaning that convective draughts are driven by condensational heating, whereas the transport term is small for temperature. However, the contributions for transport and condensation are equally important and of opposite sign in the Q2 budget, implying a lower (mid- and upper) tropospheric drying (moistening) through water vapour transport, and apart from low-level rain evaporation, a general drying of the troposphere through rain out.

1.7.2 Mesoscale convective systems

Regions with active convective draughts that is draughts that are buoyant and in the case of updraughts are saturated, cover only very small fractional areas of *O*(1-5%). However, convection is often organized in larger clusters or systems, so called mesoscale convective systems, that consist of an active convective region of *O*(1-10 km), or in the case of squall lines a narrow convective band, and a large trailing stratiform region of *O*(10-500 km). Such a system, consisting of a leading convective part with strong updraught/downdraught motion, and a mesoscale ascent (descent) in the upper (lower) half of the trailing stratiform region, is schematically illustrated in Figure 1.30 (see also Figure 1.17 for satellite images).

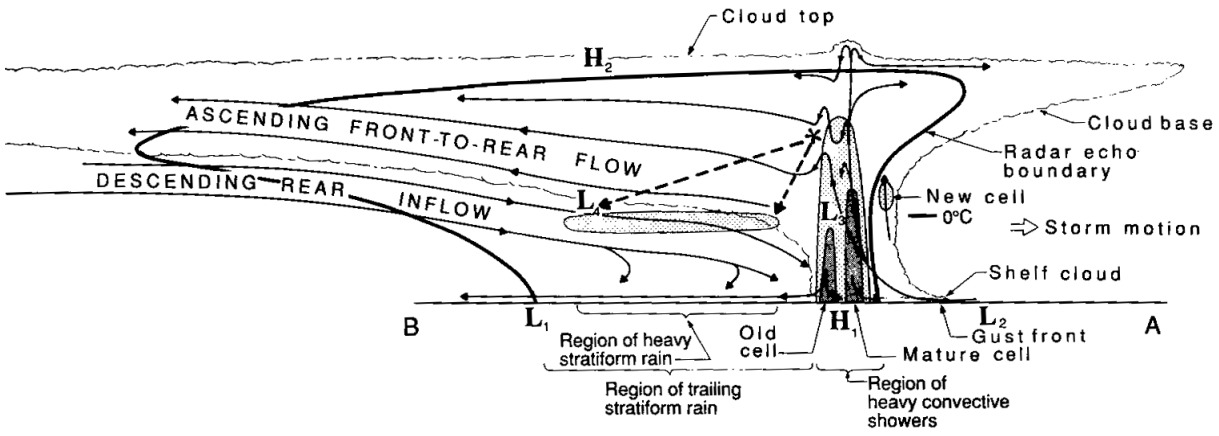

Figure 1.30: Schematic of a mesoscale convective system (squall line) moving to the right, with convective and stratiform precipitating areas. (After Houze 1993).

Both, the convective and stratiform region contribute significantly to the dynamics and the precipitation produced by the system. Large-scale measurements of Q_1-Q_3 do not allow distinguishing between the convective and stratiform contributions to the apparent sources, and strictly speaking such a distinction is not possible as there is no clear scale separation in nature between the convective and large scales. However, common practice among observers and forecaster is to estimate (define) stratiform and convective contributions to the precipitation based on distinct radar reflectivities or rain rates (e.g. Steiner et al. 1995), with convective areas are typically defined as areas with surface precipitation rates > 10 mm hr^{-1}. The Cloud Resolving Model (CRM) community (see e.g. Xu et al. 2002) often uses conditional sampling to estimate convective and stratiform contributions to Q_1-Q_3: either define convective model columns as columns with rain rates or alternatively, as columns that contain liquid water or ice and have updraught velocities > 1 m s^{-1} or downdraught velocities <-0.5 m s^{-1}; the remaining cloudy columns are then being defined as stratiform. With the aid of a CRM the convective and stratiform contributions to the heat budget of the mesoscale convective system or the domain averaged heat budget in general, can be simply

obtained as the sum over all "convective" or "stratiform" columns, e.g. using an equidistant grid, the simplest form is

$$Q^c = \frac{1}{nc}\sum_{i=1}^{nc} Q^i; \quad \Pr{}^i \rho_l > 10\, mm/hr \quad Q^{strat} = \frac{1}{ns}\sum_{i=1}^{ns} Q^i \quad 0.2 < \Pr{}^i \rho_l < 10\, mm/hr;$$
$$Q = a^c Q^c + a^s Q^s + (1 - a^c - a^s) Q^{clear}; \quad a^c = \frac{nc}{n}, \quad a^s = \frac{ns}{n} \tag{1.24}$$

where *n* is the total number of grid columns of the domain, *nc* the number of "convective" columns, *ns* the number of "stratiform" model columns, a^c and a^s are the fractional convective and stratiform areas, respectively, superscript *clear* denotes cloud free columns, Q^i is computed as either the lhs or rhs of (1.18), *Pr* is the surface precipitation flux (kg s^{-1} m^{-2}), and ρ_l is the density of liquid water.

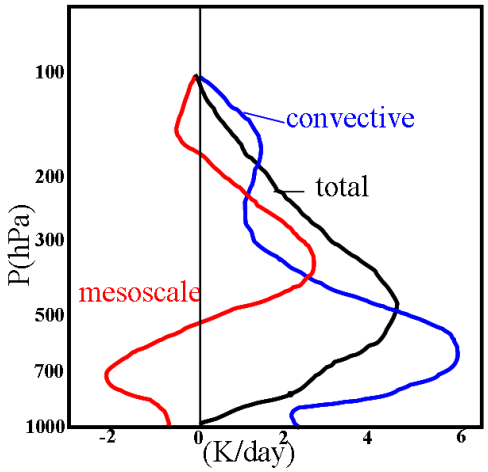

Figure 1.31a. Partition of heat source in convective and mesoscale = stratiform contribution. (After Yanai and Johnson 1997).

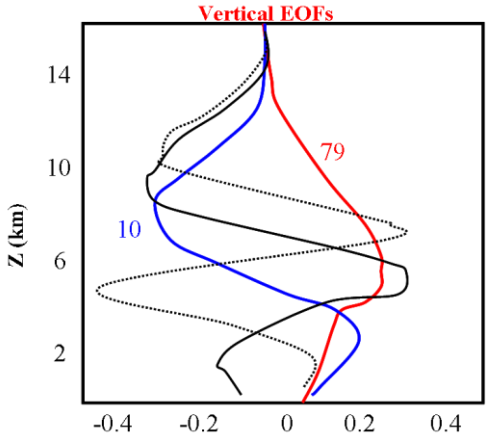

Figure 1.31b. EOF decomposition of Q_2 from CRM data of TOGA-COARE. The red and blue EOFs explain 79 and 10.5 %, respectively of the total variance.

As an example, an estimation of a characteristic "convective" and "mesoscale=stratiform" partition of Q_1 during GATE phase III is provided in Figure 1.31a as produced by Yanai and Johnson (1997). The main point is that the actual parabolic shape heating profile with maximum heating around 500 hPa, consists of a convective contribution with a strong peak further down, at around 600-700 hPa, and a mesoscale heating/cooling couple with upper-level heating due to the condensation in the elevated mesoscale ascent, and low-level cooling driven by the evaporation of stratiform rain.

For the sake of wider interest in spectral methods, an alternative method using Empirical Orthogonal Functions (EOFs) (see e.g. Toumazou and Cretaux (2001) for a description of the numerical method) has been used to decompose CRM data of convective situations (see also Lin and Arakawa 2000). As an example in Figure 1.31b is depicted a decomposition of Q_2 into the first 4 leading EOFs[2], each explaining a different degree of variance - the CRM data represents a time series of three-dimensional snapshots of convection during the Tropical Ocean and Global Atmosphere Coupled Ocean-Atmosphere Response

[2] The EOFs have been computed as horizontal (patterns) and vertical (profiles) eigenvectors from a series of three-dimensional snapshots of convective fields. Here only the leading vertical EOFs (eigenvectors that explain most of the variance) are plotted.

Experiment (TOGA-COARE). Obviously, the shape of these profiles is determined by the orthogonality constraint; however the first two leading EOFs could be interpreted as some mean and stratiform contributions, respectively.

1.7.3 Quasi-equilibrium

So far the last notion we need to introduce is "Quasi-equilibrium" which is one of the fundamental concepts that together with the CAPE is used in convective parameterizations. This concept, as first advocated by Arakawa and Schubert (1974), basically states that the convective activity (stabilization) is in quasi-equilibrium with the large-scale forcing (destabilization) of the atmosphere, so that the resulting rate of change in CAPE is small (see also Brown and Bretherton 1997). Therefore, this notion provides a simplified but tractable description of the convective activity or the overall interaction between the convection and the large-scale environment. An illustration of convective quasi-equilibrium is provided in Figure 1.32 showing a 20-day time series of Q_1 and ω as observed during GATE phase III. Obviously, Q_1 and ω are strongly correlated with positive/negative peaks in Q_1 corresponding to heating/cooling, and negative/positive peaks in ω corresponding to large-scale ascent with cooling, and large-scale subsidence warming, respectively. Furthermore, the main peaks of either Q_1 or ω in with periods of 2-4 days are actually associated to the passage of African easterly waves (see Section 1.3.4).

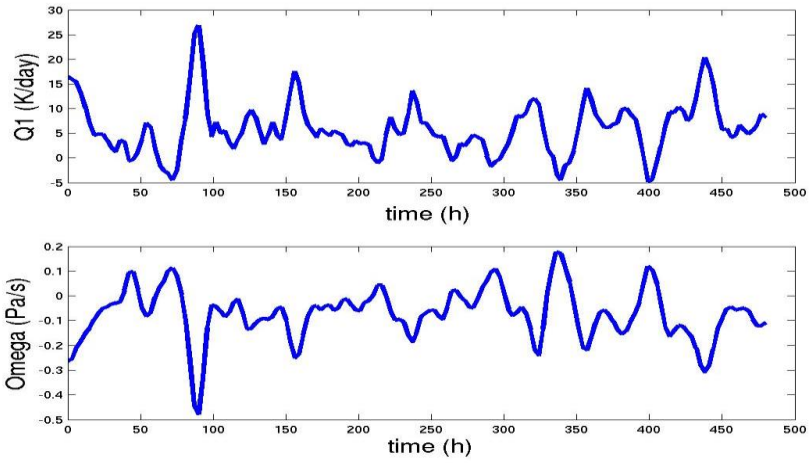

Figure 1.32: Evolution of Q_1 (K day^{-1}) at 500 hPa and ω (Pa s^{-1}) during GATE phase III.

1.8 Summary

- Convection is of crucial importance for the global energy and water balance
- Convection generates and/or influences a number of phenomena important to forecasting (thunderstorms, heavy precipitation, hurricanes, shallow convection and boundary-layer properties)
- On large horizontal scales convection is in quasi-equilibrium with the large-scale forcing (midlatitude synoptic disturbances, tropical waves)
- An important parameter for the strength of convection is CAPE
- Convection affects the atmosphere through condensation / evaporation and eddy transports
- Shallow convection is present over very large (oceanic) areas, it is controlled by the surface fluxes but also controls the surface fluxes as a results of heat and mass transport out of the subcloud

layer. In the trades takes place the transport of vapor and momentum from the subtropics to the ITCZ.

- Q_1, Q_2 and Q_3 are quantities that reflect the time and space average effect of convective transport and precipitation ("unresolved scale") and stratiform heating/drying ("resolved scale").

2 Parametrization of Convection

Roughly 40 years have now passed since the pioneering work by Manabe and Stricker (1964), Kuo (1965), and Ooyama (1971) who first recognized the need to include some kind of convective parameterization in numerical models in order to represent "subgrid" convective activity, and to avoid grid-scale saturated ascents that could quickly lead to numerical instability (see also Arakawa (2004) for a review on "past present and future of cumulus parameterization").

At that time the horizontal grid resolution of global models was something of *O*(400 km). Nowadays the horizontal resolution of global Numerical Weather Prediction models (NWPs) is of *O*(40 km) - in the IFS it is 25 km since February 2005 - and will reach resolutions of 10 km in the coming decade. Furthermore, current and next generation limited area versions of NWPs will use horizontal resolutions of O(1-3 km), and therefore can resolve at least deep convection with reasonable accuracy. But there is also the venue of the multi-scale modelling approach for climate models (Randall et al. 2003), where a CRM is nested in each grid column of the global host model in order to represent explicitly deep convection and the cloud radiation interaction, and then feedback the corresponding subgrid tendencies to the host model, acting as some kind of "super" parameterization scheme.

The reader might wonder if it is still up to date or necessary to learn about and to use "traditional" convective parameterization. Our answer is Yes, first of all, it is and will be in the next decade still too costly to run medium range (global) weather prediction and assimilation systems at resolutions that allow for an explicit representation for deep convection. Second, even CRMs still require parameterization schemes for shallow convection as shallow convective clouds have typical radius of *O*(100 m). Third, it is not yet clearly proven that higher horizontal resolution and explicit representation of convection produces better medium range forecasts than current forecasts using classical convection parameterizations, as higher resolution means more small-scale "noise" and uncertainty in the forecasts (in this case ensemble forecasts with an increased number of ensemble members would be necessary, further increasing the numerical burden). Classical convection parameterizations do generally efficiently stabilize the atmosphere and damp numerical noise. And last, but not least, classical convective parameterization schemes allow to "understand" or "constrain" convection in some easy manner; learning about these concepts and schemes is instructive and constitutes a good exercise.

2.1 Aims of convective parametrization

The task a convection parameterization scheme has to fulfil is to calculate the collective effects of an ensemble of convective clouds in a model column as a function of grid-scale variables. Recall that these are represented by the Q_1-Q_R, Q_2, Q_3.

In practice convection parameterization includes three steps:

i. Determine the occurrence and localisation of convection - this is often named as "Trigger of convection"
ii. Determine the vertical distribution of heating, moistening and momentum changes - this task is generally done with the aid of a cloud model
iii. Determine the overall amount of convective precipitation = energy conversion - this is the final step in a convection parameterization and is called "Closure".

However, as a convection parameterization is supposed to be globally applicable, requirements on the scheme include: remove convective instability and produce subgrid-scale convective precipitation (heating/drying) in unsaturated model grids, maintain a realistic vertical thermodynamic and wind structure, produce a realistic mean tropical climate, maintain a realistic variability on a wide range of time-scales, produce a realistic response to changes in boundary conditions (e.g. sea surface temperature, orography), be applicable to a wide range of scales (typical 10 – 200 km) and types of convection (deep tropical, shallow, midlatitude and front/post-frontal convection), and finally, be simple and efficient for different model forecast configurations (high-resolution deterministic forecast, 4D-Var assimilation mode, Ensemble Forecast System, and monthly and seasonal forecast systems).

2.2 Types of convection schemes

Available parameterization schemes can be regrouped in three classes (the reference list is far from exhaustive and should only be taken as indicative)

- Schemes based on moisture budgets
  - Kuo (1965, 1974)
- Adjustment schemes
  - moist convective adjustement: Manabe (1965)
  - penetrative adjustment scheme: Betts and Miller (1986), Betts-Miller-Janic
- Mass flux schemes (bulk+spectral)
  - multiple plumes , spectral model: Arakawa and Schubert (1974), Fraedrich (1976), Moorthi and Suarez (1992), Neggers et al. (2002), Cheinet (2004), Chikira and Sugiyama (2010), Park (2014)
  - single entraining/detraining plume - bulk model: e.g. Bougeault (1985), Tiedtke (1989), Gregory and Rowntree (1990), Kain and Fritsch (1990), Donner (1993), Bechtold et al (2001, 2008, 2014), Piriou et al. (2007), Gerard (2015).
  - episodic mixing- Emanuel (1991)

Currently, most NWPs and climate models use mass flux schemes, but a variant of the Betts and Miller (1986) scheme is still used at the National Centre of Environmental prediction (NCEP). In the following, each class of schemes will be discussed, with particular emphasis on the mass flux approach.

2.3 The "Kuo" scheme

The basic assumption of the "Kuo" scheme is that convective activity that is the convective precipitation is linked to large-scale moisture convergence

$$\mathrm{Pr} = (1-b)\int_0^{top}\left(\frac{\partial\bar{\rho}\bar{q}}{\partial t}\right)_{ls} dz, \tag{2.1}$$

where *Pr* denotes the surface precipitation flux, and *b* is the "Kuo" parameter which determines the part of the integrated moisture convergence that is converted into convective precipitation. The only remaining issue is then to determine the vertical distribution of the heating and moistening, which is done by assuming that the environment adjusts to a moist adiabat through cloud base. The "Kuo" scheme has often been criticized for its fundamental assumption that convection consumes water, instead of consuming potential energy, and therefore can lead to a positive feedback loop, where more convection mean more moisture convergence, and so on. However, it proofed useful and was one of the first convection schemes available.

2.4 Adjustment schemes: the Betts-Miller scheme

Representative for the class of adjustment schemes the Betts and Miller (1986) scheme is discussed here. The scheme says that if the atmosphere is unstable to a parcel lifted from the boundary-layer, and if there is a deep moist layer (for deep convection), adjust the atmospheric state back to a reference profile over some time scale. The convective tendencies for *T* and *q* produced by the scheme are then simply given by

$$\left.\frac{\partial T}{\partial t}\right|_{conv} = \frac{T^{ref}-\bar{T}}{\tau}; \quad \left.\frac{\partial q}{\partial t}\right|_{conv} = \frac{q^{ref}-\bar{q}}{\tau}, \tag{2.2}$$

where τ is a convective adjustment time scale which is typically set to 1 hour for deep convection and 3 hours for shallow convection. The reference profile for temperature T^{ref} is constructed as the moist adiabat through cloud base, including the effects of ice phase changes. Unfortunately, there is no universal reference profile for humidity. However, the scheme is efficient and produces convective tendencies that are very smooth in space and time.

Briefly, the procedure followed by the scheme can be described as follows. Find the most unstable layer in the lowest 200 hPa, draw a moist adiabat for this air and construct a first guess profile for *T* and compute a first-guess dewpoint adjustment profile *q* (Figure 2.1 a) - for a precise description how these reference profiles are constructed the reader is referred to the references and is also invited to consult the numerical code. Once this is done one has to check for conservation of enthalpy, i.e. the total adiabatic enthalpy change resulting from the adjustment of *T* must correspond to an equivalent change in the adjusted *q*

$$\begin{aligned} &dH = c_p dT + L_v dq_v = 0 \Rightarrow \\ &\int_{P_b}^{P_t} c_p\left(T^{ref}-\bar{T}\right)dp = -\int_{P_b}^{P_t} L_v(q^{ref}-\bar{q})dp. \end{aligned} \tag{2.3}$$

In the example in Figure 2.1 enthalpy is not conserved, and therefore the reference profiles must be shifted to the left as to conserve enthalpy. This is the final step of the procedure and is illustrated in Figure 2.2

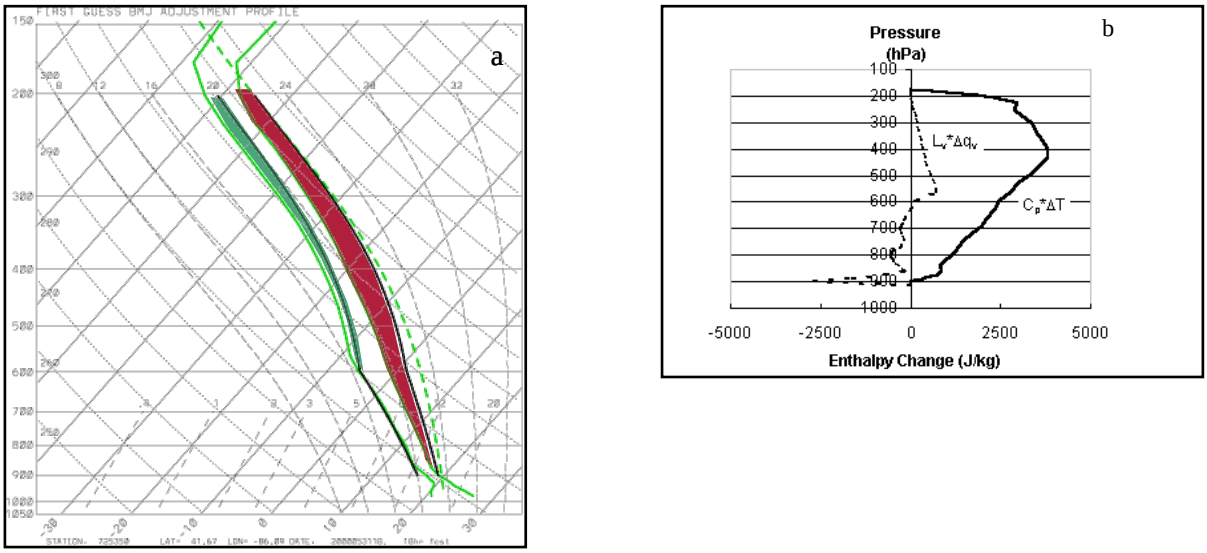

Figure 2.1 (a) Skew T(p) diagram with temperature and dewpoint sounding (solid green lines), moist adiabat (dashed green line), and reference temperature and dewpoint profiles (solid black line). The green and red areas denote the total change in enthalpy. For clarity these enthalpy changes are redrawn in (b), and demonstrate in fact a non-conservation of enthalpy. (After J. Kain, private communication)

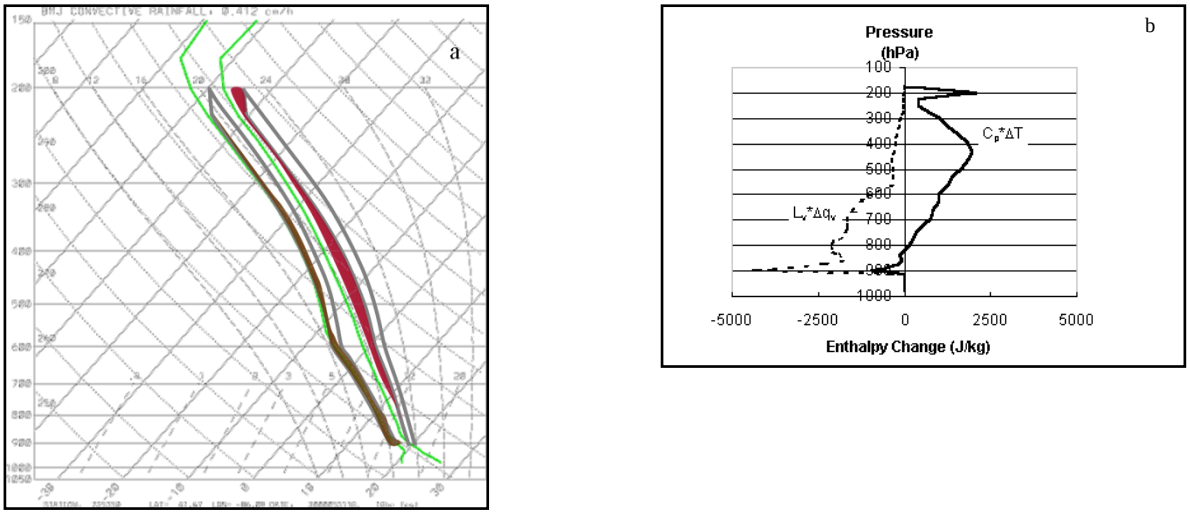

Figure 2.2: As in Figure 2.1 but with the original reference profiles (grey lines) shifted to the left in order to conserve enthalpy.

2.5 The mass flux approach

The mass flux approach is a general and quite powerful method to tackle (eddy) transport problems in fluid mechanics, in particular for convective overturning where most of the transport is done by the “large” eddy draughts that carry heat and mass upward and downward over relatively large distances.

2.5.1 Derivation of the eddy fluxes

We define the convective contribution to Q_1 as

$$Q_{1c} \equiv Q_1 - Q_R = \underbrace{L_v(\overline{c} - \overline{e})}_{condensation} - \underbrace{\frac{\partial \overline{\omega' s'}}{\partial p}}_{eddy\ \ transport} \tag{2.4}$$

and look for a simple expression of the eddy flux. Recall that the total flux is given by

$$\overline{\omega\chi} = \overline{(\overline{\omega} + \omega')(\overline{\chi} + \chi')} = \overline{\overline{\omega}\overline{\chi}} + \overline{\overline{\omega}\chi'} + \overline{\omega'\overline{\chi}} + \overline{\omega'\chi'}. \tag{2.5}$$

With the definition $\overline{\overline{\chi}} = \overline{\chi}$ and $\overline{\chi'}$ =0 the second and third term of the rhs of (2.5) vanish, and the eddy flux is obtained from

$$\overline{\omega\chi} = \overline{\omega}\overline{\chi} + \overline{\omega'\chi'}. \tag{2.6}$$

We now decompose the total domain in cumulus covered and clear sky or environmental regions (Figure 2.3)

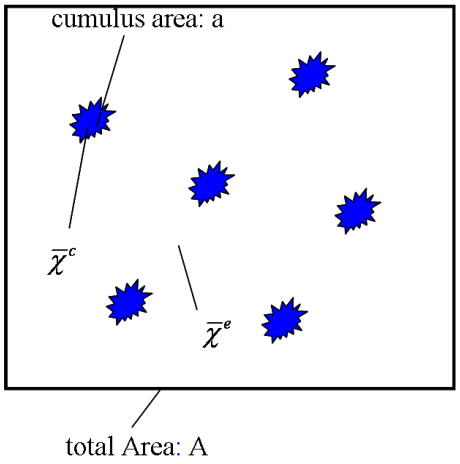

Figure 2.3: Total domain A covered by cumulus elements (blue) and clear sky environment.

and aim to represent the total flux as a sum of the flux contributions from the different areas. Defining an area average as

$$\overline{\chi} = \sigma\overline{\chi}^c + (1-\sigma)\overline{\chi}^e = \sigma\chi^c + (1-\sigma)\chi^e, \tag{2.7}$$

with superscripts *c* denoting an average over the cumulus regions and superscripts *e* denoting an average over the environmental regions, and the fractional area covered by cumulus defined as $\sigma = \frac{a}{A}$, the total flux can be written as[3]

$$\overline{\omega\chi} = \sigma\overline{\omega\chi}^c + (1-\sigma)\overline{\omega\chi}^e, \tag{2.8}$$

and the flux due to the mean vertical circulation as

[3] Note that the definition of the area averages in (2.7) and (2.8) is equivalent to a summation in an equidistant grid as defined in (1.24)

$$\bar{\omega}\bar{\chi} = \left[\sigma\omega^c + (1-\sigma)\omega^e\right]\left[\sigma\chi^c + (1-\sigma)\chi^e\right]. \tag{2.9}$$

Up to now there has been no approximation in the derivation. However, in order to easily estimate the fluxes in the convective and environmental regions in (2.8), Reynolds averaging is applied once more

$$\overline{\omega\chi}^c = \omega^c\chi^c + \overline{\omega''\chi''}^c; \quad \overline{\omega\chi}^e = \omega^e\chi^e + \overline{\omega''\chi''}^e, \tag{2.10}$$

where the double primes denote subplume variations. The first approximation consists in neglecting the subplume correlations (the second terms on the lhs of (2.10)); this is known as the "top-hat" approximation and its validity is discussed in e.g. Siebesma and Cuijpers (1995), and Wang and Stevens (2000). Then, using (2.6) and (2.8)-(2.10), and after some straightforward manipulations (left for your exercise), the eddy flux is obtained as

$$\overline{\omega'\chi'} = \overline{\omega\chi} - \bar{\omega}\bar{\chi} = \sigma(1-\sigma)\left(\omega^c - \omega^e\right)\left(\chi^c - \chi^e\right). \tag{2.11}$$

This expression can be further simplified assuming that the area covered by cumulus draughts is small, so that

$$\sigma << 1 \Rightarrow (1-\sigma) \approx 1; \quad \omega^c >> \omega^e, \tag{2.12}$$

this is called the "small area approximation". We then obtain the final result

$$\overline{\omega'\chi'} = \sigma\omega^c\left(\chi^c - \chi^e\right), \tag{2.13}$$

or, using the definition of the convective mass flux

$$M^c = \frac{-\sigma\omega^c}{g} = \bar{\rho}\sigma w^c \tag{2.14}$$

$$-\overline{\omega'\chi'} = gM^c\left(\chi^c - \bar{\chi}\right). \tag{2.15}$$

This is known as the mass flux formulation, or the mass flux approximation taking into account that we have applied the "top hat" approximation, and the "small area" approximation. Note also that the mass flux is the product of a convective scale velocity and an area fraction, and that in parameterizations schemes (not in CRM of course) it is generally only possible to determine the mass flux with reasonable accuracy, but not the individual components composing it.

For readers still interested, we wish to mention an alternative way to derive the final mass flux equations (2.15) - which is also my favourite. Using (2.8)-(2.10) we can write

$$\begin{aligned}\overline{\omega'\chi'} &= \overline{\omega\chi} - \bar{\omega}\bar{\chi} \approx \sigma\omega^c\chi^c + (1-\sigma)\omega^e\chi^e - \bar{\omega}\bar{\chi} = \sigma\bar{\omega}^c\bar{\chi}^c + (1-\sigma)\omega^e\chi^e - \bar{\chi}\left[\sigma\omega^c + (1-\sigma)\omega^e\right] \\ \overline{\omega'\chi'} &= \sigma\omega^c(\chi^c - \bar{\chi}) + (1-\sigma)\omega^e(\chi^e - \bar{\chi})\end{aligned} \tag{2.16}$$

If we now also make the "small area approximation" then $\chi^e \approx \bar{\chi}$, so that the last term in (2.16)b can be neglected, and the same result as in (2.13) is obtained.

2.5.2 Mass flux and Q_1-Q_3

Replacing the flux terms in Q_1-Q_3 by their corresponding mass flux expressions, one obtains

$$
\begin{aligned}
Q_{1c} &\equiv L(\overline{c}-\overline{e}) + g\frac{\partial\left[M^c(s^c-\overline{s})\right]}{\partial p} \\
Q_2 &\equiv L(\overline{c}-\overline{e}) - Lg\frac{\partial\left[M^c(q^c-\overline{q})\right]}{\partial p} \\
Q_3 &\equiv g\frac{\partial\left[M_c(\vec{v}^c-\overline{\vec{v}})\right]}{\partial p}
\end{aligned}
\tag{2.17}
$$

To predict the influence of convection on the large-scale with this approach we now need to describe the convective mass-flux, the values of the thermodynamic (and momentum) variables inside the convective elements and the condensation/evaporation term. This requires, as usual, a cloud model and a closure to determine the absolute (scaled) value of the mass flux.

2.5.3 Mass flux entraining detraining plume model

In order to determine the unknown quantities in (2.17), i.e. the mass flux, the in-cloud values, and the condensation rate, one applies the mass flux formalism again, but now for each individual cloud *i*. The cloud scale mass flux equations for mass continuity, enthalpy, and specific humidity then write

$$
\begin{aligned}
&\frac{\partial\sigma^i}{\partial t} + D^i - E^i - g\frac{\partial M^i}{\partial p} = 0 \\
&\frac{\partial\left(\sigma^i s^i\right)}{\partial t} + D^i s^i - E^i\overline{s} - g\frac{\partial\left(M^i s^i\right)}{\partial p} = Lc^i \\
&\frac{\partial\left(\sigma^i q^i\right)}{\partial t} + D^i q^i - E^i\overline{q} - g\frac{\partial\left(M^i q^i\right)}{\partial p} = -c^i,
\end{aligned}
\tag{2.18}
$$

where it is assumed that the cloud exchanges mass with the environment through detrainment *D* of cloud mass and entrainment *E* of environmental air. The entrainment/detrainment rates E, D [s^{-1}] are related to the classical fractional entrainment/detrainment per unit length [m^{-1}] by $E=M/\rho\,\varepsilon$, and $D=M/\rho\,\delta$. The cloud environment mass exchange is depicted in Figure 2.4.

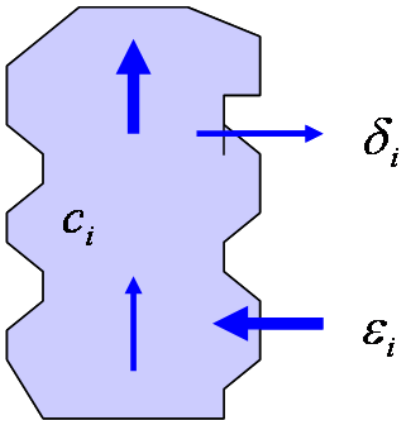

Figure 2.4: Convective cloud exchanging mass with environment through detrainment δ and entrainment ε.

Actually, equations (2.18) already constitute a simplified one-dimensional set in the vertical coordinate *p* only. They are derived from a more complete three-dimensional set of cloud-scale equations where through integrations over variable cloud boundaries, the entrainment and detrainment coefficients appear as flux divergences in the horizontal directions[4] - for a detailed derivation of (2.18) the interested reader is referred to Gregory and Miller (1989), and Siebesma (1998).

Equation set (2.18) is still rather complicated and in general the following simplifications are applied

- Steady state plumes: $\frac{\partial \chi^i}{\partial t} = 0$; most mass flux parameterizations today still use this approximation, some are however, prognostic.
- Bulk mass flux approach: $\frac{1}{M^c}\frac{\partial M^c}{\partial z} = \varepsilon - \delta \Rightarrow -g\frac{\partial M^c}{\partial p} = E - D$ with $\varepsilon = \sum_i \varepsilon^i$, $\delta = \sum_i \delta^i$. Single or "bulk" entrainment/detrainment rates are used that are supposed to represent the collective effects of a cloud ensemble.
- Spectral method: $M^c = \sum_i M^i$ or $M^c(p) = \int_0^{\varepsilon_D} m_b^c(\varepsilon)\eta(p,\varepsilon)d\varepsilon$, where m_b^c is the cloud base mass flux as function of the entrainment rate; Arakawa and Schubert (1974), Fraedrich (1976), and derivatives.

Entrainment

The mass flux method is a quite powerful and simple method, however, its weak point is the need to specify the entrainment/detrainment rates. Unfortunately, in spite of many attempts (e.g. Siebesma and Cuijpers, 1995; Lin and Arakawa, 1997, Carpenter et al. 1998) there has been so far no universally valid formulation of entrainment rates applicable to all convective situations and in all schemes. - a detailed description of the entrainment/detrainment rates as used in the IFS is given in Chapter 3.

As an alternative to the entraining plume model, the episodic mixing as proposed by Raymond and Blyth (1992) and Emmanuel (1991) is also briefly summarized. The method stems from observations that show that the entraining plume model might be a poor representation of individual cumulus clouds. The conceptual idea is that mixing is episodic, and that different parts of an updraught mix differently. The basic implementation of such a scheme might be summarized as follows: assume a stochastic distribution of mixing fractions for part of the updraught air, create N mixtures.

Version 1: find level of neutral buoyancy of each mixture.

Version 2: move mixture to next level above or below and mix again - repeat until level of neutral buoyancy is reached

Unfortunately, although physically appealing the model is very complex, and numerical very expensive (its cost is proportional to the square of the number of vertical model levels.

[4] Terms of the form $\delta\chi = \sigma\overline{\frac{\partial u\chi}{\partial x}}^c$

2.5.4 Large scale cumulus effects

For simplicity, we consider the bulk model, as it is also used in the IFS. With the simplifications given above we can rewrite (2.17) and (2.18) to obtain the set of equations

$$
\begin{aligned}
&Q_{1c} \equiv L_v(c-e) + g\frac{\partial\left[M^c(s^c-\bar{s})\right]}{\partial p} \\
&-g\frac{\partial M^c}{\partial p} = E - D \\
&-g\frac{\partial\left(M^c s^c\right)}{\partial p} = E\bar{s} - Ds^c + L_v c.
\end{aligned}
\tag{2.19}
$$

The set of equations (2.19) is closed provided that the entrainment/detrainment rates are specified, and a microphysical scheme is available to determine the condensation/evaporation term. The equation for Q_{1c} constitutes the "flux form" equation. An equivalent expression for Q_{1c} is obtained if one replaces the flux divergence term in Q_{1c} by the corresponding derivatives as given by the 2nd and 3rd equation of (2.19) to obtain

$$
Q_{1C} \equiv -gM_c\frac{\partial\bar{s}}{\partial p} + D(s^c-\bar{s}) - Le. \tag{2.20}
$$

This form is much simpler as it essentially only contains a mass flux advection term and a detrainment term, and therefore it is called the "advective" form. Note that the first equation of (2.19) and (2.20) are physically identical, but as we will see in Chapter 3 their numerical solution might in general differ slightly.

The physical interpretation of (2.20) is that convection affects the large scale environment by

- Heating through compensating subsidence between cumulus elements (term 1) - this was already recognized by Bjerknes (1938)
- The detrainment of cloud air into the environment (term 2)
- Evaporation of cloud and precipitation (term 3)

To avoid confusion, it is important to note that in the advective form (2.20) of the mass flux formulation, the condensation heating does not appear directly in Q_{1C}. It is however a crucial part of the cloud model, where this heat is transformed in kinetic energy of the convective draughts. So there is no contradiction with the discussion in Subsection 0.

2.5.5 Convective closure

The cloud model determines the vertical structure of convective heating and moistening (microphysics, variation of mass flux with height, entrainment/detrainment assumptions). The determination of the overall magnitude of the heating (i.e., surface precipitation in deep convection) requires the determination of the mass flux at cloud base. This is called the closure problem.

Deep convective closure: CAPE

Prominent closure types for deep convection assume an equilibrium that establishes over a typical time scale of one hour between the production of CAPE (or cloud work function) by the large-scale, and its

consumption by the convection. The production of CAPE by the large-scale forcing, and surface processes, as well as its consumption are schematically illustrated in Figure 2.5.

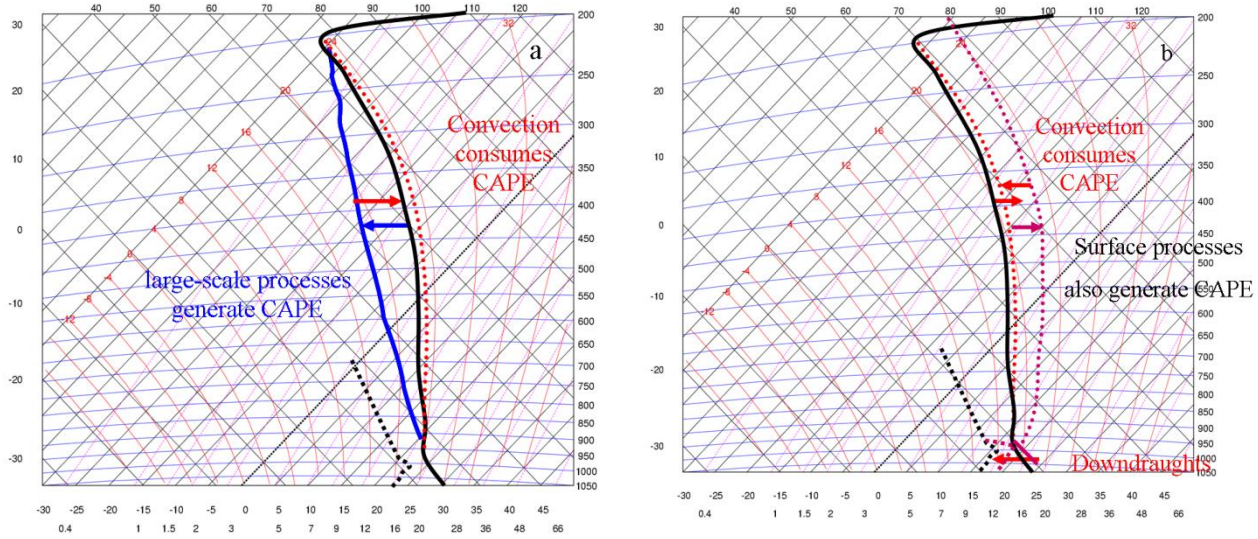

Figure 2.5: Tephigrams illustrating (a) production of CAPE through large-scale processes (blue line), and convective stabilization, and (b) production of CAPE through surface fluxes, and downdraught effects, i.e. stabilization through cooling and increase of surface fluxes .The black solid lines denote the environmental temperature profile

Shallow convective closures

As for deep convection some schemes also use some kind of CAPE adjustment for shallow convection (e.g. Betts and Miller (1986), Bechtold et al. (2001)), but with a longer adjustment time-scale of typically three hours.

Grant (2001) developed a simple equilibrium closure, where the cloud base convective mass flux is proportional to the product of the updraught fraction a and a convective scale velocity w^*, the latter being proportional to the boundary-layer or cloud base height z_{PBL} and the buoyancy flux HB

$$M_b^c = a\bar{\rho}w^*; \quad w^* = \left(\frac{g}{\bar{\theta}} z_{PBL} \frac{HB}{\bar{\rho}c_p}\right)^{1/3}; \quad HB = HS + 0.61\bar{\theta}\frac{c_p}{L}HL \tag{2.21}$$

with the convective fraction a=0.03.

The IFS model applies a boundary-layer equilibrium closure for shallow convection, and a CAPE closure for deep convection, both are in detail explained in Chapter 3.

2.6 Summary

- Convection parametrizations need to provide a physically realistic forcing/response on the resolved model scales and need to be practical.
- A number of approaches to convection parametrization exist.
- Basic ingredients to present convection parametrizations are a method to trigger convection, a cloud model, and a closure assumption.

- The mass-flux approach has been successfully applied to both interpretation of data and convection parametrization.
- The mass-flux approach can also be used for the parametrization of shallow convection.
- It can also be directly applied to compute the transport of chemical species
- The parametrized effects of convection on humidity and clouds strongly depend on the assumptions about microphysics and mixing in the cloud model --> uncertain and active research area
- For the future, alternative approaches are already available based on an explicit representation of deep convection (Multi-model approach), on wavelets (Yano et al. 2005), general spectral methods (Fournier et al. 2003), or Neural Networks (Hsieh and Tang, 1998)

3 The IFS convection parameterization

The IFS convection scheme has been originally developed by Tiedtke (1989), and in the following has been continuously further developed and improved by Gregory et al. (2000), Jakob and Siebesma (2003), and Bechtold et al. (2004).[5]

The general functioning of the scheme and the cloud (populations) it is supposed to represent are illustrated in Figure 3.1

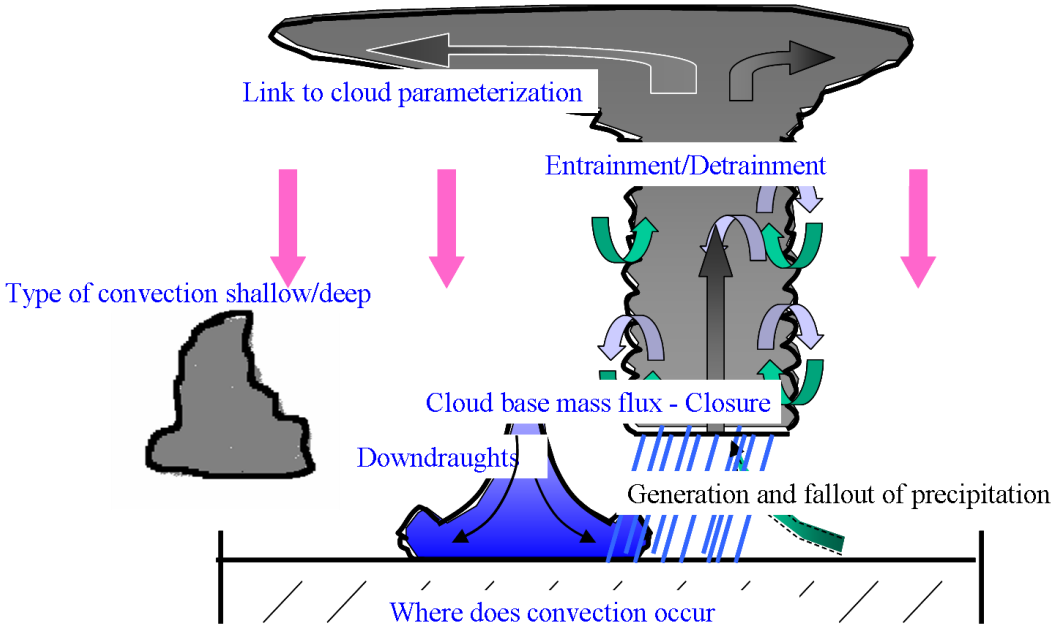

Figure 3.1: Schematic of a bulk convection scheme with a shallow and deep entraining/detraining cloudy ascending plume, and downdraught region. Further represented features are trigger of convection, environmental subsidence, microphysics and precipitation, and detrainment of cloud mass in anvils.

The main characteristics of the scheme can be summarized as follows

[5] A detailed description of the convection scheme and its numerical implementation can be obtained from http://www.ecmwf.int/research/ifsdocs/CY38r1/

- bulk mass-flux scheme
- entraining/detraining plume cloud model
- three types of convection: deep, shallow and mid-level - mutually exclusive
- trigger of convection based on parcel instability, parcel velocity, and parcel initial *t* and *q* perturbation
- saturated downdraughts
- simple microphysics scheme
- convective (cloud base mass flux) closure dependent on type of convection
    - deep: CAPE adjustment
    - shallow: PBL equilibrium
    - mid-level: large-scale omega
- strong link to cloud parameterization - convection provides source for cloud condensate

3.1 Basic large-scale convective tendencies

In contrast to the cloud environment decomposition used in the derivation of the mass flux formulation in Chapter 2, the basic equations of the IFS scheme use a more complete convective updraught-downdraught-environment decomposition. The basic equations for the large-scale tendencies due to convection for dry static energy *s*, specific humidity *q*, the horizontal wind, cloud condensate, and passive chemical tracer species C_i, written in flux form are

$$\left(\frac{\partial \bar{s}}{\partial t}\right)_{cu} = g\frac{\partial}{\partial p}\left[M^u(s^u-\bar{s})+M^d(s^d-\bar{s})\right]+L(c^u-e^d-e_{subcld})-L_f(Mlt-Fr) \tag{3.1}$$

$$\left(\frac{\partial \bar{q}}{\partial t}\right)_{cu} = g\frac{\partial}{\partial p}\left[M^u(q^u-\bar{q})+M^d(q^d-\bar{q})\right]-(c^u-e^d-e_{subcld}) \tag{3.2}$$

$$\left(\frac{\partial \bar{\vec{v}}}{\partial t}\right)_{cu} = g\frac{\partial}{\partial p}\left[M^u(\vec{v}^u-\bar{\vec{v}})+M^d(\vec{v}^d-\bar{\vec{v}})\right] \tag{3.3}$$

$$\left(\frac{\partial \bar{q}_{li}}{\partial t}\right)_{cu} = D^u q_{li}^u, \tag{3.4}$$

$$\left(\frac{\partial \overline{C_i}}{\partial t}\right)_{cu} = g\frac{\partial}{\partial p}\left[M^u(C_i^u-\overline{C_i})+M^d(C_i^d-\overline{C_i})\right] \tag{3.5}$$

where c^u denotes the condensation rate in the updraught, e^d the evaporation rate of precipitation in the downdraught, e_{subcld} the evaporation rate of rain below cloud, L_f the latent heat of melting, *Mlt* the snow melting rate, *Fr* the freezing rate of cloud water, q_{li} the total cloud condensate (liquid+ice), and D^u the mass detrainment rate. The total (liquid + ice) precipitation flux is given as

$$\mathrm{Pr} = \int_{p_{top}}^{p}\left(G^u-e^d-e_{subcld}\right)\frac{dp}{g}, \tag{3.6}$$

where *G* denotes the conversion rate from cloud condensate into precipitation.

These equations are solved at the end of the convection code, after having evaluated the mass fluxes, the values in the up- and downdraughts and the precipitation production/evaporation.

3.2 Triggering of convection

The first step in the convection algorithm consists in the selection of convective columns. The procedure as illustrated in Figure 3.2 as follows:

First test for shallow convection: add a *T* and *q* perturbation depending on the magnitude of the surface fluxes to a near surface air parcel. Do ascent with strong entrainment, check for LCL, solve w^u equation (see next Section), continue ascent until the CTL is reached, which is defined as w^u <0. If w^u (LCL)>0 and *p(*CTL*)*-*p(*LCL*)*<200 hPa , shallow convection is supposed to occur.

Now test for deep convection with a similar procedure. Start close to the surface, form a 30 hPa mixed-layer, add a temperature and humidity perturbation of 0.2 K and 1×10^{-4} kg kg^{-1}, respectively, lift it to the LCL, do cloud ascent (i.e. condensate must be present) with small entrainment + water fallout until w^u >0. The cloud is identified as deep convective if p(LCL)-p(CTL)>200 hPa. If the required cloud thickness is not attained, test subsequent mixed-layers, lift them to the LCL, test for cloud thickness etc., until a sufficiently deep cloud is found. However, for economic and physical reasons the procedure is only repeated for departure layers inside the lowest 300 hPa of the atmosphere.

If neither shallow nor deep convection is found, a third type of convection – “midlevel” – is activated, originating from any model level above 500 m, if large-scale ascent prevails and the relative humidity at that level exceeds 80%.

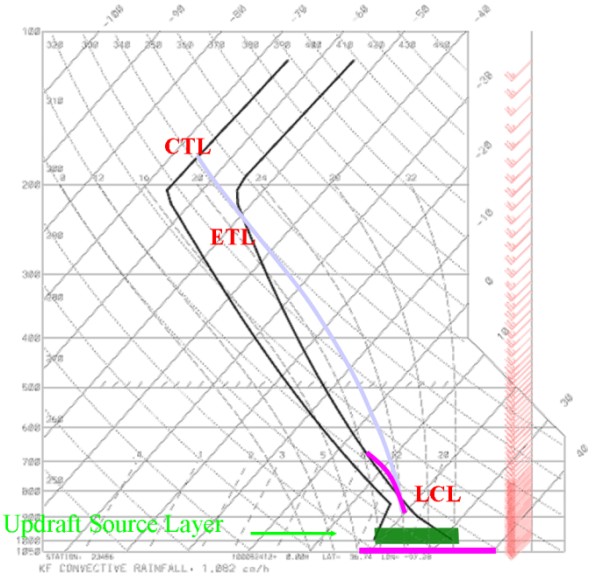

Figure 3.2: Illustration of Trigger procedure on a Skew-T diagram, including environmental profiles of temperature and dewpoint temperature (black), a near surface layer used as departure level for shallow ascent (pink), and a 30 hPa deep source layer (dark green) used for a first guess deep ascent (sky blue). If no deep ascent is found, the procedure is repeated for departure layers in the lowest 300 hPa. Note also that the cloud top level (CTL) might lie above the equilibrium temperature level (ETL), as it is determined by the level where the parcel vertical velocity vanishes, and the parcel might overshoot its ETL.

3.3 Cloud model equations: updraughts

The updraught equations describe cloud scale mass continuity

$$-g\frac{\partial M^u}{\partial p} = E^u - D^u, \tag{3.7}$$

dry static energy and specific humidity

$$-g\frac{\partial M^u s^u}{\partial p} = E^u \bar{s} - D^u s^u + Lc^u; \quad -g\frac{\partial M^u q^u}{\partial p} = E^u \bar{q} - D^u q^u - c^u \tag{3.8}$$

total cloud condensate (liquid + ice) , and precipitating specie (rain+snow)

$$-g\frac{\partial M^u q_{li}^u}{\partial p} = -D^u q^u + c^u - G^u; \quad -g\frac{\partial M^u q_r^u}{\partial p} = -D^u q_r^u + G^u - S_{fallout} \tag{3.9}$$

and cloud scale horizontal momentum

$$-g\frac{\partial M^u u^u}{\partial p} = E^u \bar{u} - D^u u^u + \underbrace{g\sigma^u\left(\frac{\partial z^u}{dx}\right)_p}_{\equiv 0}; \quad -g\frac{\partial M^u v^u}{\partial p} = E^u v - D^u v^u + \underbrace{g\sigma^u\left(\frac{\partial z^u}{dy}\right)_p}_{\equiv 0}. \tag{3.10}$$

Note that the third term of the rhs of (3.10) describing the cloud scale pressure gradient $g\sigma^u\left(\frac{\partial z^u}{dx}\right)_p = -\frac{1}{\bar{\rho}}\sigma^u\left(\frac{\partial p^u}{\partial x}\right)_z$ is actually not included in the model, but modelled through higher entrainment and detrainment coefficients for momentum. With this parameterization the model is only able to produce downgradient="diffusive" momentum transport, reducing the vertical wind shear (as observed in unorganized "popcorn" convection), but not upgradient transport, leading to an increase in vertical wind-shear (this processes might be important in organized convective systems). Much effort has been made in analysing and parametrizing the difficult cloud-scale pressure gradient term (Zhang and Cho, 1991; Kershaw and Gregory 1997; Zhang and Wu 2003). The most "handy" parameterization available is probably that of Gregory et al. (1997), where the cloud scale pressure gradient term is expressed as $-\frac{1}{\bar{\rho}}\sigma^u\left(\frac{\partial p^u}{\partial x}\right)_z = -0.7M^u g\frac{\partial \vec{U}}{\partial p}$, but tests showed that it gives similar results to the present formulation where the cloud-scale pressure gradient term is mimicked the strong entrainment and an additional perturbation velocity.

Furthermore, the updraught equations for passive (non reactive, non soluble) chemical tracer write

$$-g\frac{\partial M^u C_i^u}{\partial p} = E^u \bar{C}_i - D^u C_i^u \tag{3.11}$$

Finally, an equation for the kinetic energy (vertical velocity of the draughts) is added that ser ves to determine the cloud top and to parameterize precipitation fall out

$$\frac{\partial K^u}{\partial z} = -\frac{E^u}{M^u}(1+\beta c_d)2K^u + \frac{1}{f_t(1+\gamma)}g\frac{T_v^u - \bar{T}_v}{\bar{T}_v}; \quad K^u = \frac{\left(w^u\right)^2}{2}, \tag{3.12}$$

where Υ=0.5 is the virtual mass coefficient, and c_d =0.506 is a drag coefficient (Simpson and Wiggert, 1969), β =1.875, and f_t = 2 is introduced because the flow is highly turbulent (Cheng et al. 1980).

These equations are solved (model) level by level, starting at the LCL.

3.4 Cloud model equations: downdraughts

The downdraught plume is represented as an updraught plume taken upside down. The downdraught equations are solved starting at the estimated downdraught top, which actually is the level of free sink (LFS), defined as the level where a mixture of updraught and environmental air becomes negatively buoyant through evaporation of cloud condensate and melting of precipitation. As a rule of thumb, the level of free sink corresponds to the level of minimum $\bar{\theta}_e$ which is generally around the zero degree isotherm. Initializing the downdraught mass flux at the LFS proportional to the updraught mass flux at cloud base

$$M^d_{LFS} = -0.3 M^u_b \tag{3.13}$$

the following downdraught equations are solved

$$g\frac{\partial M^d}{\partial p} = E^d - D^d \tag{3.14}$$

$$-g\frac{\partial M^d s^d}{\partial p} = E^d \bar{s} - D^d s^d + L e^d; \quad g\frac{\partial M^d q^d}{\partial p} = E^d \bar{q} - D^d q^d + e^d \tag{3.15}$$

$$g\frac{\partial M^d u^d}{\partial p} = E^d \bar{u} - D^u u^u + \underbrace{g\sigma^u\left(\frac{\partial z^u}{dx}\right)_p}_{\equiv 0}; \quad -g\frac{\partial M^u v^u}{\partial p} = E^d v - D^d v^d + \underbrace{g\sigma^d\left(\frac{\partial z^d}{dy}\right)_p}_{\equiv 0}. \tag{3.16}$$

$$g\frac{\partial M^d C^d_i}{\partial p} = E^d \bar{C}_i - D^d C^d_i. \tag{3.17}$$

3.5 Entrainment and detrainment

Entrainment is the single most important parameter in a mass flux convection parametrization. The entrainment and detrainment rates are expressed as a sum of “mixing” (1) and “organized” (2) contributions

$$E^u = E^u_1; \quad D^u = D^u_1 + D^u_2. \tag{3.18}$$

$$E^u_1 = \varepsilon^u_1 M^u \bar{\rho}^{-1} f_{scale}; \quad D^u_1 = \delta^u_1 M^u \bar{\rho}^{-1}$$

$$\varepsilon^u_{deep} = 1.75\times 10^{-3} m^{-1}; \varepsilon^u_{shal} = 2\times\varepsilon^u_{deep} \tag{3.19}$$

$$\delta^u_1 = 0.75\times 10^{-4} m^{-1}$$

A similar expression is used for the downdraught detrainment/entrainment rates. The mixing contributions stem from a formulation by Simpson (1983) that expresses the fractional entrainment rate as being inversely proportional to the cloud radius, $\varepsilon \equiv \frac{0.2}{R_c}$. With this in mind, the values for ε^u defined in (3.19)

imply an assumed ensemble mean updraught radius at cloud base of roughly 100 m for deep convection, and 50 m for shallow convection implying a pretty strong entrainment. Entrainment is applied to positive buoyant convective clouds only. In (3.19) we have also included a vertical scaling function f_{scale} in order to mimic the effect of a cloud ensemble. As the scaling function strongly decreases with height, the mixing detrainment will eventually become larger than the entrainment, and the mass flux starts to decrease with height. The entrainment rate is further modulated by the relative humidity of the environment, so that the final entrainment formulation writes

$$E_1^u = \varepsilon_1^u \frac{M^u}{\bar{\rho}}(1.3 - RH) \quad \left(\frac{q_{sat}(\bar{T})}{q_{sat}^{base}(\bar{T})} \right)^3 \tag{3.20}$$

This turns out to be probably the simplest formulation to allow for high entrainment rates near cloud base and to account for the observation that (mid) tropospheric relative humidity controls the cloud top heights, and plays an important role in the modulation of tropical waves and the Madden-Julian Oscillation (Lin et al. 2008, Kim et al. 2011). Typical entrainment profiles produced by (3.21) for an atmosphere under constant forcing but with different values of free-tropospheric humidity are shown in Figure 3.3. The entrainment profiles closely correspond to the LES results by Derbyshire et al. (2011) (their Figure 5) and also show a clear transition with increasing mid-tropospheric humidity from shallow convection, with tops near 2 km, to deep convection. The reader is referred to the comprehensive overview on entrainment by De Rooy et al. (2012) where further typical shallow and deep convective entrainment and detrainment profiles are provided.

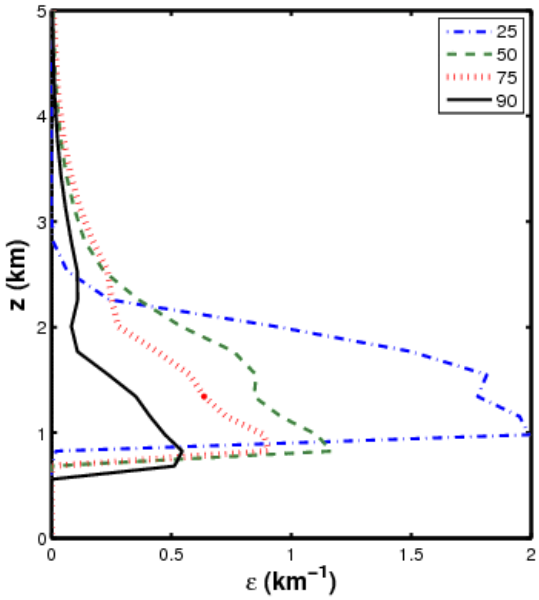

Figure 3.3: Entrainment profiles for different values of free-tropospheric relative humidity (%) from Single Column Model simulations following Derbyshire et al. (2004).

Organized detrainment is active when negative buoyancy occurs. It is then set proportional to the change in updraught kinetic energy with height

$$\frac{M^u(z)}{M^u(z+\Delta z)} = (1.6 - RH)\sqrt{\frac{K^u(z)}{K^u(z+\Delta z)}}; \quad D_2^u = \frac{\Delta M^u}{\rho \Delta z}, \tag{3.22}$$

where Δz is the corresponding model layer thickness.

3.6 Microphysics and precipitation

The updraught condensation rate is computed through a saturation adjustment

$$c^u = \frac{g}{\Delta p}\left(q^u - q^u_{sat}\right)M^u, \tag{3.23}$$

where q^u is the value of the specific humidity before the saturation adjustment, and q^u_{sat} is the specific humidity at saturation after the adjustment. The conversion from cloud condensate to precipitation is treated following Sundqvist (1978)

$$G^u = \frac{M^u}{\bar{\rho}}\frac{c_0}{0.75 w^u} q^u_{li}\left[1-\exp\left\{-(q^u_{li}/q_{lcrit})^2\right\}\right] \tag{3.24}$$

Where the auto-conversion coefficient $c_0 = 1.5\times10^{-3}$ s^{-1}, $q_{lcrit} = 5\times10^{-4}$ kg kg^{-1}, and w^u is limited to a maximum value of 10 m s^{-1}. One recognizes from (3.24) that the higher the updraught velocity, less there is precipitation fall out.

The fallout of rain/snow is parameterized as

$$S_{fallout} = \frac{g}{\Delta p} M^u \frac{V}{w^u} q^u_r; \quad V = 21.18\left(q^u_r\right)^{0.2}, \tag{3.25}$$

with *V* the terminal velocity of rain.

Concerning the evaporation of rain, it occurs i) in the downdraught, where it is supposed to keep the downdraught saturated, and ii) below cloud base following

$$e_{subcld} = \sigma\alpha_1\left(RH_{crit}\,\bar{q}_s - \bar{q}\right)\left(\frac{\sqrt{p/p_{surf}}}{\alpha_2}\frac{\mathrm{Pr}}{\sigma}\right)^{\alpha_3}, \tag{3.26}$$

where $\alpha_1 = 5.44\times10^{-4}s$, $\alpha_2 = 5.09\times10^{-3}$, $\alpha_3 = 0.577$, RH_{crit}=0.9 (0.7) over water (land) is the critical relative humidity below which evaporation is supposed to occur, and the area covered by convection is set to $\sigma = 0.05$.

3.7 Closure

3.7.1 Deep convection

Following the derivation Bechtold et al. (2014) that included earlier work by Donner and Philips (2003), Nordeng (1994) and Gregory et al. (2000), an equilibrium is assumed between the large-scale and boundary-layer forcing (generating convective available potential energy) and convection (reducing the CAPE). As a measure of CAPE (J kg^{-1}) we use the density-weighted buoyancy integral of an entraining ascending air parcel, denoted as PCAPE (J m^{-3})

$$PCAPE = -\int_{base}^{top}\frac{T_v^u - \bar{T}_v}{\bar{T}_v}dp. \tag{3.27}$$

The advantage of PCAPE over an entraining CAPE is the density scaling that more readily relates the time derivative of PCAPE to the convective mass flux. Taking the time derivative of (3.27) one can derive a prognostic equation for PCAPE and identify the different production/sink terms: the production by large-scale advection (LS), the production by boundary-layer processes (surface heat fluxes, BL) and a sink of PCAPE due to convective transport and mixing and evaporative cooling

$$\frac{\partial PCAPE}{\partial t} \approx \underbrace{-\int_{Pbase}^{Ptop} \frac{1}{\bar{T}_v}\frac{\partial \bar{T}_v}{\partial t}\,dp}_{LS+Cu} \underbrace{-\int_{Pbase}^{Ptop} \frac{1}{\bar{T}_v}\frac{\partial T_{v,u}}{\partial t}\,dp + \left.\frac{T_v^u - \bar{T}_v}{\bar{T}_v}\right|_{base}\frac{\partial p_{base}}{\partial t}}_{BL+Cu} = \tag{3.28}$$

$$= \left.\frac{\partial PCAPE}{\partial t}\right|_{LS} + \left.\frac{\partial PCAPE}{\partial t}\right|_{BL} + \left.\frac{\partial PCAPE}{\partial t}\right|_{Cu=shal+deep}$$

Knowing all the different terms we can integrate (3.28) . Here we aim for a diagnostic equilibrium solution where $\partial PCAPE/\partial t$ is small compared to the rhs terms – this is also often referred to as convective quasi-equilibrium (Arakawa and Schubert, 1974). The trick is to express the convective tendency so that this condition is fulfilled. We can either express the convective tendency by a relaxation term, assuming that convection reduces PCAPE over a time-scale τ toward a reference value $PCAPE_{bl}$, or by assuming that convection counteracts the large-scale forcing by stabilization through environmental compensating subsidence – this latter expression then brings in the convective mass flux which is the required quantity in a mass flux convection scheme

$$\left.\frac{\partial PCAPE}{\partial t}\right|_{cu,1} = -\frac{PCAPE - PCAPE_{BL}}{\tau}; \qquad \tau = \frac{H}{\bar{w}_u}$$

$$\left.\frac{\partial PCAPE}{\partial t}\right|_{LS} = \left.\frac{\partial PCAPE}{\partial t}\right|_{cu,2} = \int_{Pbase}^{Ptop} \frac{1}{\bar{T}_v}\frac{\partial \bar{T}_v}{\partial t}\,dp = -\int_{zbase}^{ztop} \frac{g}{\bar{T}_v} M \left(\frac{\partial \bar{T}_v}{\partial z} + \frac{g}{c_p}\right) dz \tag{3.29}$$

Equating the two expressions in (3.29) gives

$$-\frac{PCAPE - PCAPE_{bl}}{\tau} = -\int_{base}^{top} M \frac{g}{\bar{T}_v}\bar{\rho}\left(\frac{\partial \bar{T}_v}{\partial z} + \frac{g}{c_p}\right) dz = -\frac{M_{u,b}}{M^*_{u,b}} \int_{zbase}^{ztop} \frac{g}{\bar{T}_v} M^* \left(\frac{\partial \bar{T}_v}{\partial z} + \frac{g}{c_p}\right) dz \tag{3.30}$$

with

$$M = M^u + M^d = \frac{M_b^u}{M_b^{u*}} M^* \tag{3.31}$$

The ratio between the actual (final) cloud base mass flux and the unit (initial) cloud base mass flux M_b^u / M_b^{u*} is the convective scaling or closure factor. The initial mass flux profile *M** is known from the updraught and downdraught computation starting at cloud base with value $M_b^* = 0.1\Delta p/(g\Delta t)$, with Δt the model time step. This results in an expression for the "final" cloud base mass flux given as

$$M_b^u = M_b^{u*} \frac{PCAPE - PCAPE_{bl}}{\tau} \frac{1}{\int_{base}^{top} \frac{g}{\bar{T}_v} M^* \left(\frac{\partial \bar{T}_v}{\partial z} + \frac{g}{c_p}\right) dz}; \quad M_b^u \geq 0. \tag{3.32}$$

We still need to specify the convective adjustment time τ. In previous IFS cycles this was a constant depending only on the horizontal model resolution. However, optimal results in terms of convective

adjustment (rainfall) and convection-large-scale interaction are obtained using a convective turnover timescale $\tau = \alpha_{res}\tau_c = \alpha_{res} H / \bar{w}^u$, where τ_c is the convective turnover time scale, *H* the cloud depth, $\bar{w}^u$ is the vertically averaged updraught velocity, and α_{res} is a factor depending on the horizontal model resolution. As the large-scale forcing = horizontal divergence varies linearly as a function of horizontal resolution, so does α_{res} from a value of 1 at dx=10 km to a maximum value of 2.6 at dx=125 km.

The PCAPEbl term requires further elaboration. In model cycles prior to November 2013 this term has not been considered, implying that deep convection removes all PCAPE (Gregory et al. 2000). This assumption obviously fails in non-equilibrium situations with rapidly varying boundary-layer forcing such as the diurnal cycle of convection and the convection tied to advective boundary-layers. As shown in Shutts and Gray (1999) deep convection scales with the surface buoyancy flux and therefore for convection rooting in the boundary-layer (lowest 50 hPa) Bechtold et al. (2014) have expressed the departure from equilibrium by PCAPEbl but using the integrated tendencies instead of the surface flux

$$PCAPE_{bl} = -\tau_{bl}\frac{1}{T*}\int_{surf}^{base}\left(\frac{\partial \bar{T}_v}{\partial t}\right)_{bl} dp. \tag{3.33}$$

The tendency $\partial \bar{T}_v / \partial t\big|_{bl}$ includes all boundary-layer processes other than convection, i.e. turbulent diffusion, radiation and advection; therefore the corresponding tendencies must be available before the call of the convection scheme. The temperature scale $T_* = c_p^{-1} gH$ is set to 1 and different boundary-layer time-scales are used for land and water. For land the convective turnover time-scale $\tau_{bl}=\tau_c$ is used and for water the advective time-scale $\tau_{bl} = H_b / \bar{u}_{bl}$ involving the boundary-layer depth H_b and the average wind speed in the boundary-layer.

3.7.2 Shallow convection

The closure for shallow convection aims for an equilibrium of the subcloud layer - which approximatively corresponds to the planetary boundary-layer (PBL)

$$\int_{surf}^{base}\frac{\partial \bar{h}}{\partial t} dp = 0, \tag{3.34}$$

where *h* is the moist static energy. The physical meaning of this equation is simply, what comes in at the surface must come out at the top, i.e. at cloud base. Including all other physical processes, in practice this means taking into account all tendencies of the model produced by other parameterizations, (3.34) becomes

$$\int_{surf}^{base}\left[g\frac{\partial\left(\overline{w'h'}\right)_{cu}}{\partial p} + \left(\frac{\partial \bar{h}}{\partial t}\right)_{turb} + \left(\frac{\partial \bar{h}}{\partial t}\right)_{dyn} + \left(\frac{\partial \bar{h}}{\partial t}\right)_{rad}\right] dp = 0. \tag{3.35}$$

Expressing the convective flux at cloud base by its mass flux formulation

$$\rho\left(\overline{w'h'}\right)_{base}^{cu} = M_b^u\left(h^u - \bar{h}\right)_{base}; \quad \left(\overline{w'h'}\right)_{surf}^{cu} = 0, \tag{3.36}$$

with the surface fluxes are hidden in $\left(\frac{\partial \bar{h}}{\partial t}\right)_{turb}$, we obtain the final result for the cloud base mass flux

$$M_b^u = \frac{-\int_{surf}^{base}\left[\left(\frac{\partial \bar{h}}{\partial t}\right)_{turb}+\left(\frac{\partial \bar{h}}{\partial t}\right)_{dyn}+\left(\frac{\partial \bar{h}}{\partial t}\right)_{rad}\right]dp}{\left(h^u-\bar{h}\right)_{base}}; \quad M_b^u \geq 0 \tag{3.37}$$

3.7.3 Mid-level convection

Ascents of mid-level clouds root above the PBL. Mid-level convection exists in the model when there is large-scale ascent, and the relative humidity is > 80%. The closure for mid-level convection is simply set to

$$M_b^u = \bar{\rho}\bar{w}_b \tag{3.38}$$

3.8 Numerics

The last and not least important issue we wish to treat is the numerics of the parameterization, including the vertical discretization and the numerical solution of the final tendency equations (3.1)-(3.5) that actually constitute one-dimensional advection equations.

3.8.1 Vertical discretization and conservation

The vertical discretization of the scheme is displayed in Figure 3.3. All fluxes are defined at half-model levels and basic state model variables are defined at full model levels using the basic midpoint integral theorem

$$\chi_k = \frac{1}{\Delta p}\int_{k-1/2}^{k+1/2}\chi dp; \quad \Delta p = p_{k+1/2}-p_{k-1/2}. \tag{3.39}$$

Using this discretization, the convective tendencies must satisfy the following conservation constraints

$$\begin{aligned}
&\int_{top}^{surf}\left[\left(\frac{\partial \bar{s}}{\partial t}\right)_{cu}-L_v\left(\frac{\partial \bar{q}_{li}}{\partial t}\right)_{cu}\right]\frac{dp}{g} = L_v\,\mathrm{Pr}_{surf}\\
&\int_{top}^{surf}\left[\left(\frac{\partial \bar{q}}{\partial t}\right)_{cu}+\left(\frac{\partial \bar{q}_{li}}{\partial t}\right)_{cu}\right]\frac{dp}{g} = -\mathrm{Pr}_{surf}\\
&\int_{top}^{surf}\left(\frac{\partial \bar{\vec{v}}}{\partial t}\right)_{cu}\frac{dp}{g} = 0\\
&\int_{top}^{surf}\left(\frac{\partial \bar{C}_i}{\partial t}\right)_{cu}\frac{dp}{g} = 0
\end{aligned} \tag{3.40}$$

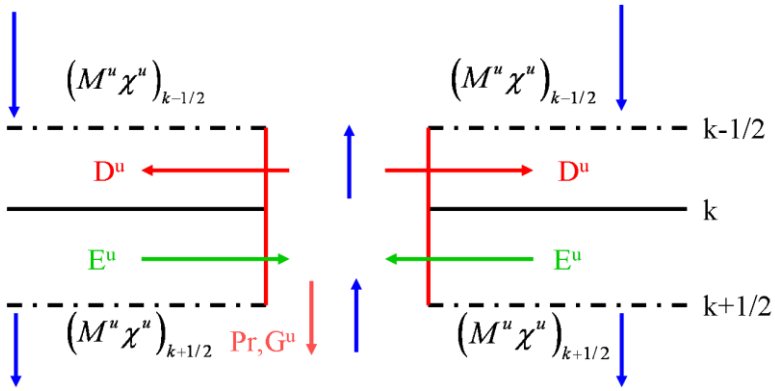

Figure 3.4. Vertical discretization of the model, with all fluxes defined at half model levels, and basic model state variables defined at full model levels k.

3.8.2 Explicit solution

The convective tendency equation for a passive tracer, or momentum is considered to explain the numerical solution of (3.1)-(3.5)

$$\frac{\partial \bar{\chi}}{\partial t} = g\frac{\partial}{\partial p}\left[M^u(\chi^u - \bar{\chi})\right]. \tag{3.41}$$

Using the discretization as in Figure 3.3 one obtains the explicit solution for the tendency

$$\frac{\partial \bar{\chi}_k}{\partial t} = \frac{\bar{\chi}_k^{\,n+1} - \bar{\chi}_k^{\,n}}{\Delta t} = \frac{g}{\Delta p}\left[M^u(\chi^u - \bar{\chi})\right]_{k-1/2}^{k+1/2}. \tag{3.42}$$

However, when this explicit centred difference solution is put back to the host model, it is known to produce unstable solutions, "zigzag" profiles in the vertical with growing amplitude. In order to obtain a stable solution the mass flux must satisfy the Courant-Friedrich-Levy (CFL) criterion

$$M^u\frac{g\Delta t}{\Delta p} \le 1; \quad \Delta t = t^{n+1} - t^n, \tag{3.43}$$

Δt is the model time step. Another numerical requirement to obtain stable solutions is to use an "upstream" formulation ("what arrives at a model level comes from above through convection induced environmental subsidence"). This can be achieved e.g. by defining shifted half-level values, e.g. $\bar{\chi}_{k-1/2} = \bar{\chi}_{k-1}$ to obtain

$$\left(\frac{\partial \bar{\chi}_k}{\partial t}\right)_{conv} = \frac{g}{\Delta p}\left[M^u_{k+1/2}\chi^u_{k+1/2} - M^u_{k-1/2}\psi^u_{k-1/2} - M^u_{k+1/2}\bar{\chi}^{\boldsymbol{n}}_{\boldsymbol{k}} + M^u_{k-1/2}\bar{\chi}^{\boldsymbol{n}}_{\boldsymbol{k-1}}\right] \tag{3.44}$$

3.8.3 Implicit solution

Implicit formulations are known to be numerically stable. The fully implicit solution of the advection equation is obtained by simply replacing the time index *n* of the rhs of (3.44) by *n+1* to obtain

$$\frac{\bar{\chi}^{\boldsymbol{n+1}}_{\boldsymbol{k}} - \bar{\chi}^{n}_{k}}{\Delta t} = \frac{g}{\Delta p}\left[M^u_{k+1/2}\chi^u_{k+1/2} - M^u_{k-1/2}\psi^u_{k-1/2} - M^u_{k+1/2}\bar{\chi}^{\boldsymbol{n+1}}_{\boldsymbol{k}} + M^u_{k-1/2}\bar{\chi}^{\boldsymbol{n+1}}_{\boldsymbol{k-1}}\right] \tag{3.45}$$

with the quantities in the convective draughts have been treated as "constants". Reordering (3.45) gives

$$(1+M^u_{k+1/2})\bar{\chi}^{n+1}_{k} - M^u_{k-1/2}\bar{\chi}^{n+1}_{k-1} = \bar{\chi}^n_k + \frac{g\Delta t}{\Delta p}\left[M^u_{k+1/2}\chi^u_{k+1/2} - M^u_{k-1/2}\psi^u_{k-1/2}\right], \tag{3.46}$$

which constitutes a simple linear bi-diagonal equation system with the unknowns $\bar{\chi}^{n+1}_{k}$ and $\bar{\chi}^{n+1}_{k-1}$ that can be easily solved in a single "downward sweep". Having evaluated the unknowns, the convective tendency is obtained as

$$\left(\frac{\partial\bar{\chi}_k}{\partial t}\right)_{conv} = \frac{\bar{\chi}^{n+1}_{k} - \bar{\chi}^n_k}{\Delta t} \tag{3.47}$$

3.8.4 The semi-lagrangien solution

In order to use the semi-lagrangian framework we have to use the advective form (2.20) instead of the flux form of the tendency equations

$$\frac{d\bar{\chi}}{dt} = \frac{\partial\bar{\chi}}{\partial t} + \underset{Adv\ veloc.}{M^u g}\frac{\partial\bar{\chi}}{\partial p} = -\frac{g}{\Delta p}\left[D^u(\chi^u - \bar{\chi})\right], \tag{3.48}$$

where for simplicity the downdraught contribution has been omitted. The convective tendency is obtained as

$$\left(\frac{\partial\bar{\chi}}{\partial t}\right)_{conv} = \frac{\bar{\chi}_{dep} - \bar{\chi}}{\Delta t} - \frac{g}{\Delta p}\left[D^u(\chi^u - \bar{\chi})\right]; \quad \bar{\chi}_{dep} = \bar{\chi}_{(P - M^u g\Delta t)} \tag{3.49}$$

where $\bar{\chi}$ is the value at the arrival point (current model level *k*), and the value at the departure point (subscript *dep*) is the environmental value a distance $M^u g\Delta t$ "back" from the current pressure level. In general the departure point lies between two model levels so that an interpolation is involved. In practice one solves (3.49) iteratively, evaluating the advection velocity first at the arrival point, and in the following iterations at the new departure points. The advantage of the semi-lagrangian method is that it is stable, the mass fluxes or time step are not subjected to the CFL stability criterion. There is, however also a stability criterion ("the iteration will not converge") for (3.49) known as the Lifschitz criterion saying that

$$g\frac{\Delta M^u}{\Delta p}\Delta t \le 1 \tag{3.50}$$

which is less stringent than the CFL as it implies only the divergence of the mass flux, and not the mass flux itself. The drawback of the semi-lagrangian solution is that it is not formally conserving (evaluating the vertical integral of (3.49) will depend on discretization and accuracy of interpolation); this is why in the IFS the preferred solution is the implicit formulation in flux form described in Subsection 3.8.3.

3.9 Tracer transport experiments

Examining tracer transport in convective situations allows to visualise, understand and evaluate convective transport. We conclude this Chapter with numerical tracer transport experiments, comparing the tracer transport as simulated with the IFS convection scheme in single-column and fully three-dimensional global mode, against corresponding CRM simulations.

3.9.1 Numerical stability

In the first experiment, single-column model (SCM) simulations forced with observed large-scale tendencies for temperature and humidity are performed for a period of continental convection observed during the ARM 1997 experiment over the Great Planes (Xu et al. 2002). The convective and total surface precipitation simulated by the model, as well as the observed precipitation are plotted in Figure 3.5. Three main precipitation events can be detected with the last one producing intensities of 80 mm h^{-1}. Generally, the precipitation events are reasonably reproduced by the IFS SCM.

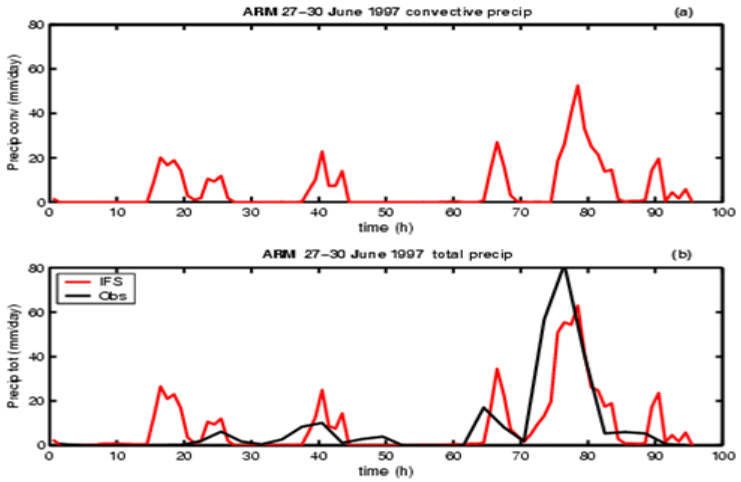

Figure 3.5: Evolution of convective (a) and total rainfall rates (mm/day) (b) as simulated by the IFS SCM and observed during the ARM 1997 experiment. The SCM is forced with observed surface fluxes, and large-scale tendencies for temperature and humidity.

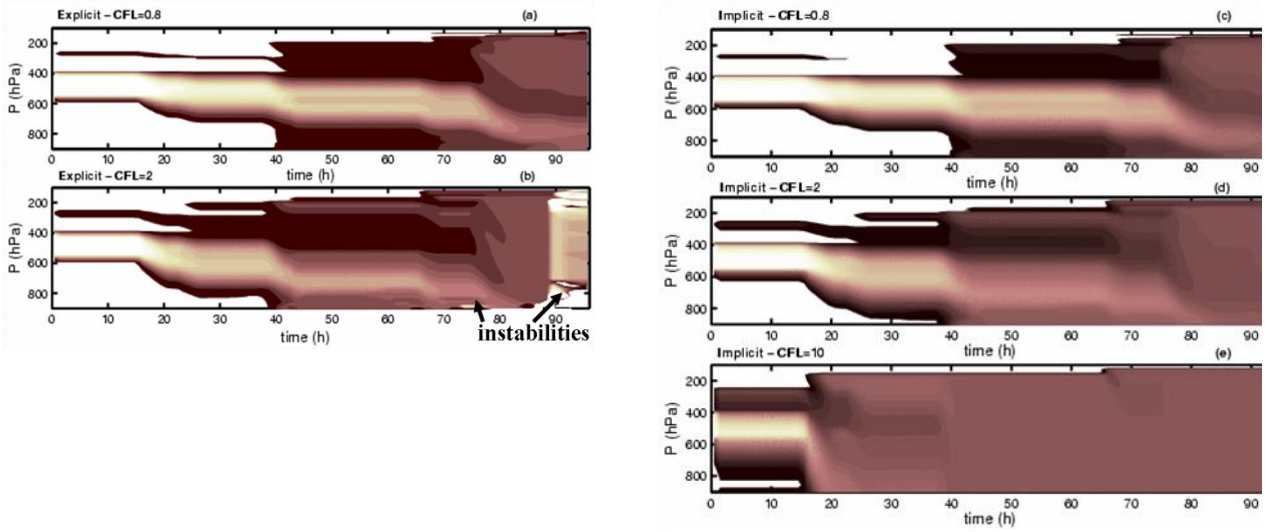

Figure 3.6: Stability tests for a mid-tropospheric tracer using explicit and implicit time integrations at different CFL numbers (3.43). The different CFL numbers are generated by scaling the mass fluxes prior to their use in the tracer routine.

In Figure 3.6 the evolution of a mid-tropospheric tracer with initial concentration one is examined using two different time integration schemes, an explicit scheme and an implicit scheme, at different CFL numbers. In order to keep the time evolution of the mass fluxes the same in each experiment, the different

CFL numbers are not obtained by changing the time step of the model, but by scaling the convective mass fluxes prior to their use in the routine that computes the convective tracer transport. We observe that for CFL=0.8 the explicit and implicit solutions barely differ. However, for CFL=2 instabilities occur in the explicit solution after t=85 hours (in fact heavily positive and negative values appear that for problems with colour shading do not readily become apparent in Figure 3.6b), whereas the implicit solution is perfectly stable even for CFL=10 (Figure 3.6c). The results for CFL=10 from the explicit are omitted as they are off scale. More information can be drawn from Figure 3.6c-d, namely that for increasing mass flux, a mass flux scheme behaves like a diffusion scheme, where all concentrations become perfectly mixed.

3.9.2 Comparison SCM, CRM and global simulations

The IFS SCM simulations forced with large-scale tendencies for temperature and humidity observed during TOGA-COARE, are evaluated against CRM simulations (courtesy J.-P. Chaboureau using the Meso-nh model) that are forced in an identical manner. Tracers are initialized in the boundary-layer and mid-troposphere. Furthermore, global simulations are performed for the same period starting from the ERA-40 year reanalysis, and using horizontally uniform tracer fields in order to mimic the absence of horizontal advection in the SCM and CRM.

Figure 3.7 shows the evolution of the convective and total rainfall rate as produced by the IFS SCM and the CRM. Reassuringly, the IFS convection scheme produces rainfall rates (and therefore also mass fluxes) that are close to the CRM results, so that the following comparison of convective tracer transport by the two models is supposed to be meaningful.

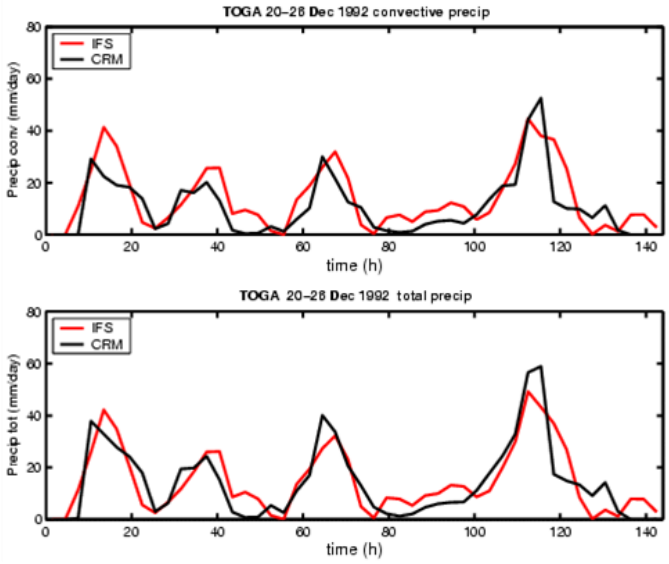

Figure 3.7: Evolution of convective (top) and total (bottom) rainfall rate as produced by the IFS SCM and the CRM.

The evolution of a boundary-layer tracer and a mid-tropospheric tracer as produced by the IFS convection parameterization and the CRM is shown in Figure 3.8. In both models, the boundary-layer tracer is rapidly transported to the tropopause in the convective draughts that have their roots inside the boundary-layer. In contrast, the mid-tropospheric tracer is moved upward, but also slowly downward due to the so called cumulus induced environmental subsidence. After a period of 3 days both the lower- and mid-tropospheric tracer becomes quasi well-mixed, even if the CRM shows somewhat less mixing the IFS SCM. The tracer

evolution obtained from the IFS global model at resolution T159 is shown in Figure 3.9 as average over the TOGA-COARE region. The results reasonably correspond to that in Figure 3.8, but the tracers go up higher due to the higher tropopause in the global run (the tropopause in the SCM and CRM runs is actually too low due to non-accurate forcing data above 14 km).

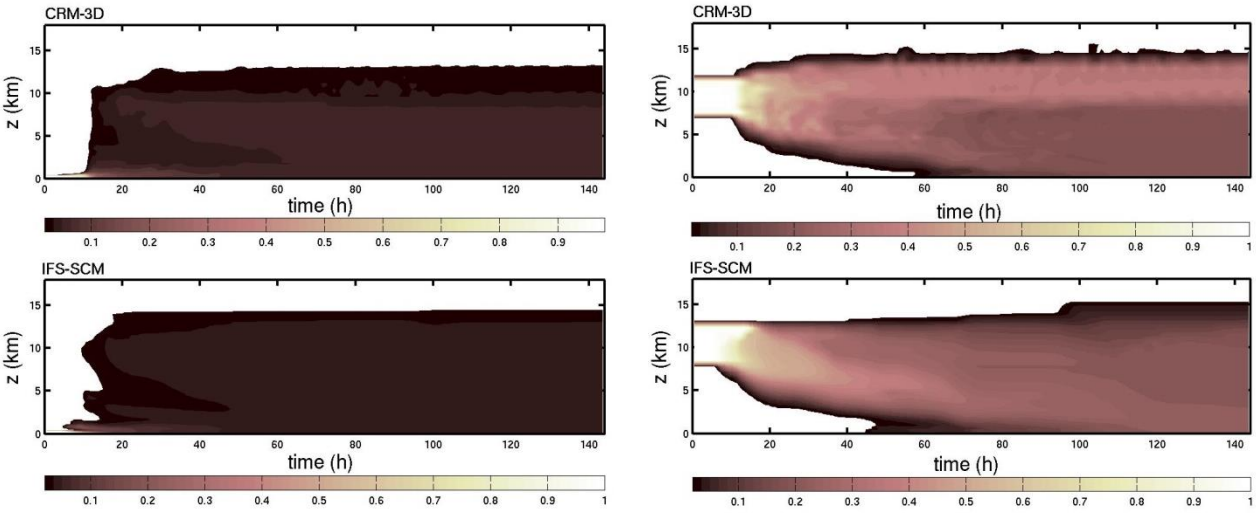

Figure 3.8: Evolution of a boundary-layer tracer (left), and a mid-tropospheric tracer (right) during a period of TOGA-COARE, as simulated by the IFS SCM, and a three-dimensional CRM (CRM data courtesy J.-P. Chaboureau)

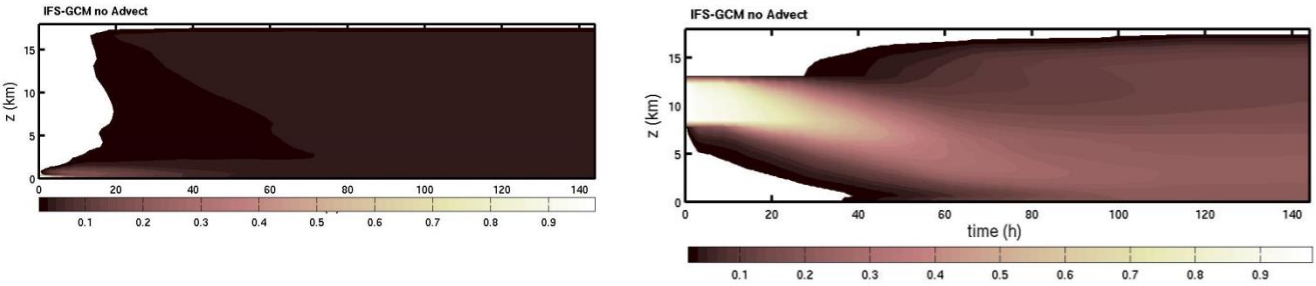

Figure 3.9: Same as Figure 3.8 but from a global IFS simulation at resolution T159 initialized with ERA40. For better comparison, the horizontal advection has been switched off for tracers.

Finally, a useful tool to represent convective mixing/transport is the Mixing Matrix. The dimensions of the matrix are *K x K*, where *K* is the number of model levels, and initially its values are zero apart from the diagonal elements that have value unity. The Mixing Matrix is universal and can be applied to any passive tracer. It is also a useful tool to verify the numerics of the convection scheme as its row values should always sum to 1, and neither be negative nor exceed 1 (monotonicity), and the vertical integral over pressure of its column values must be constant in time (conservation). In Figure 3.9 it is illustrated for the present case for day 1 and 3 of the integration. Non-zero elements in the upper-left part of the matrix indicate rapid updraught transport, elements just below the diagonal slow subsiding motions, and elements far below the diagonal rapid downdraught transport. After about 3 days the matrix becomes “full”. If one wants to perform back-tracing experiments, i.e. to determine the original profile/source of a measured

tracer concentration one could invert the mixing matrix. However, after a few time steps this becomes impossible as the matrix becomes singular, indicating that de-mixing is unphysical. The transpose or adjoint of the matrix, however, always exists and is the preferred tool for back-tracing experiments. Further experimentation showed that the adjoint is useful (there is sufficient sensitivity or information) for periods on the order of 12-48h depending on the convective events.

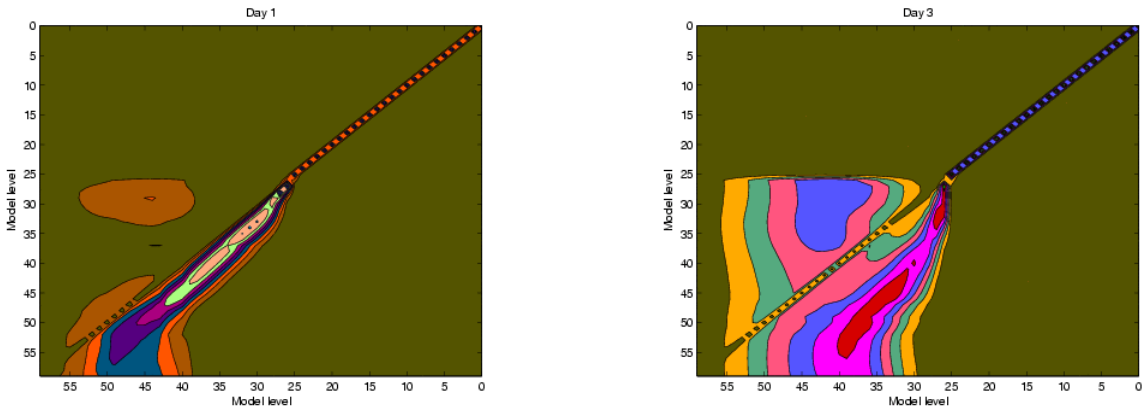

Figure 3.10. Convective mixing matrix representative for day 1 (a) and day 3 (b) of the integration in a 60-level version of the IFS. The tropopause corresponds to level 25.

4 Forecasting - case studies

We wish to conclude the course with a few case studies on deep convective situations within their synoptic environment, and to illustrate the relevant available ECMWF products.

4.1 1-4 December 2003 French flood

The synoptic situation for 3 December 2003 12 UTC is displayed in Figure 4.1. As shown by a comparison between the analyses and the 48h deterministic forecast in Figure 4.1a,b, the synoptic situation with a large PV streamer (“trough”) extending over the Iberian Peninsula and northern Africa, a strong low-level Jet between Tunisia/Sicily and south-eastern France bringing hot and humid air, is well forecasted by the

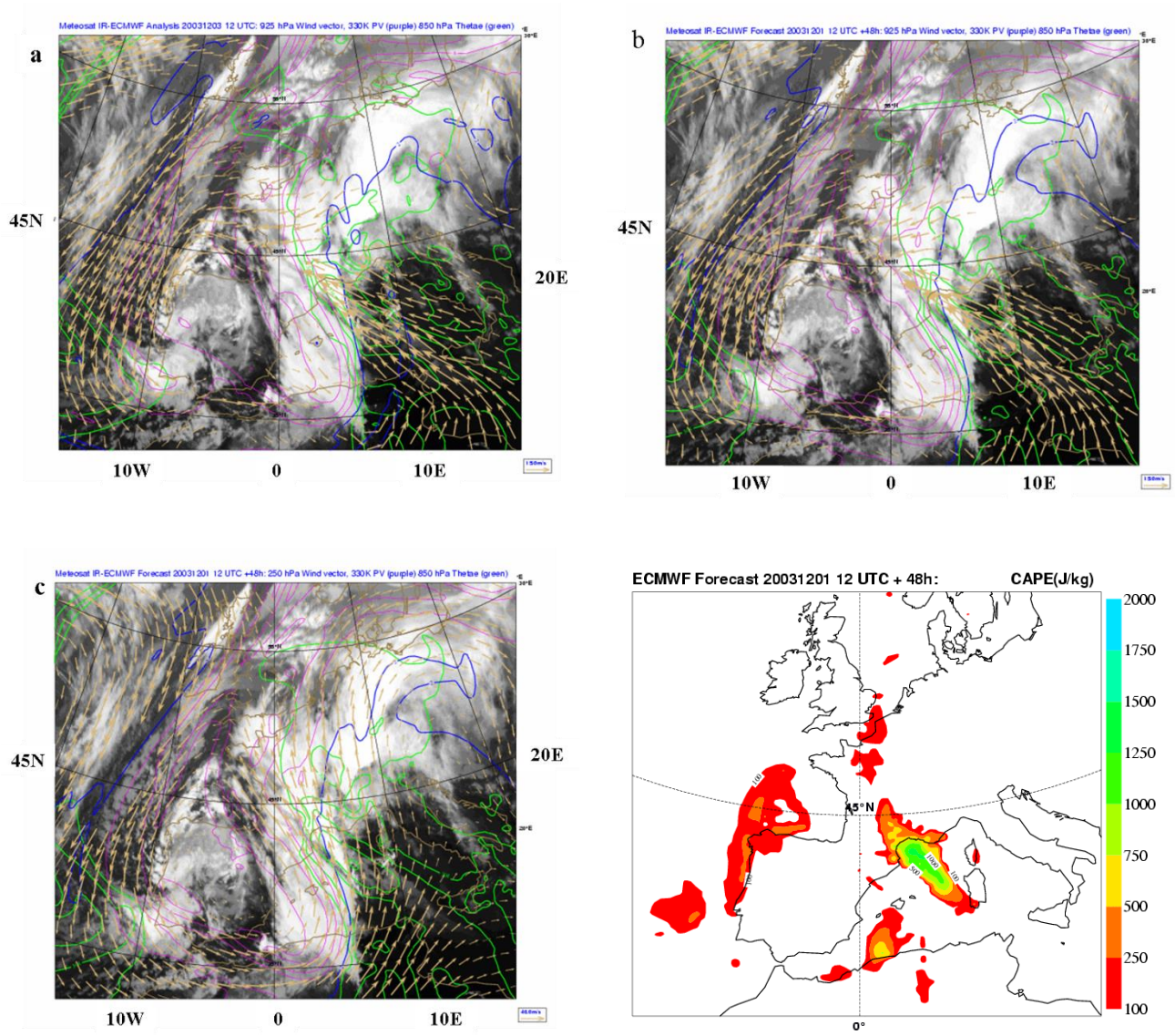

Figure 4.1: Convective systems over western Mediterranean and southeastern France for 3 December 2003 12 UTC. (a) Meteosat 7 infrared image, analysed 330 K PV (pink+blue isolines), 925 hPa wind vectors and 850 hPa θ_e. (b) same as (a) but from 48h deterministic forecast starting 1 December 12 UTC. (c) same as (b), but with 250 hPa wind vectors. (c) CAPE (J/kg) from 48h deterministic forecast. The wind unit vector for the 925 hPa winds is 15 m/s (a) and (b),, and 40 m/s/ for the 250 hPa winds (c).

deterministic system 48h ahead. Furthermore, at the 250 hPa level (Figure 4.1c) strong upper-level divergence occurs over Tunisia/northern Algeria, and further northward over the Mediterranean. Associated with the flow, two V-shaped convective systems can be identified, one over northern Algeria, and a smaller but more intense system forming between the Baleares islands and Sardinia. CAPE is rather localized but attains values of up to 2000 J kg^{-1} in the latter system (Figure 4.1d), where low-level convergence of water vapour and warm air advection attains its maximum values. Weaker convection is present off the Portuguese coast in the "cold part" of the trough or PV anomaly. The synoptic analysis is also confirmed by lightning observations, showing weaker convection around the Iberian Peninsula, but strong lightning along a southeast-northwest oriented line between Algeria and south-eastern France. Similar cases have been discussed in (Bechtold and Bazile 2001; Stein et al. 2000)

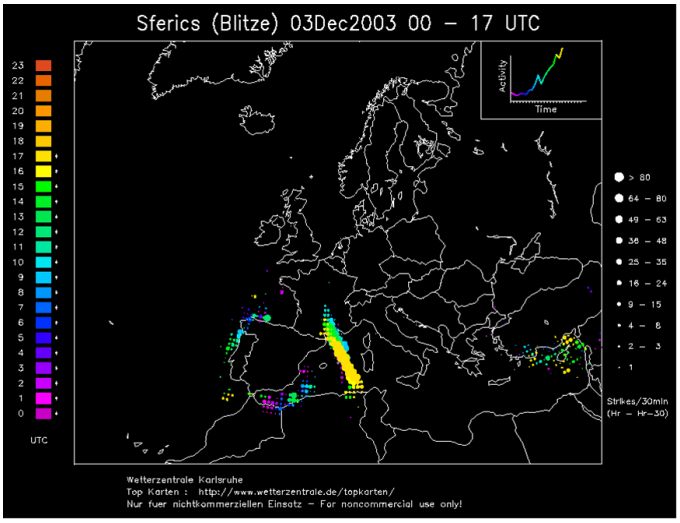

Figure 4.2: Lightning observations for Europe between 00 and 17 UTC, 3 December 2003 (Courtesy http://www.wetterzentrale.de).

Actually, the period with intense convective rains over south-eastern France lasted from 1 to 4 December 2003. To get an idea of the predictability of these synoptically forced convective rain events, the area averaged observed precipitation together with the forecasted values, obtained from forecasts with different start (base) times, is depicted in Figure 4.3. The reassuring result is that as the event approaches, the forecasts become more accurate. Experience with the current IFS system indicates that for strongly forced convection, deterministic forecasts with lead times of 48-96h can still be considered as sufficiently accurate for warnings. More information on the predictability of such events can be obtained from the Ensemble Prediction System (EPS), consisting of 50 perturbed ensemble members. As an example, the probability, as obtained from the EPS, for the 72h accumulated precipitation to exceed 150 mm is depicted in Figure 4.4 for different forecast lead times. For the current situation, an indication of an extreme precipitation event is already indicated 5 days ahead. With decreasing lead time the probabilities increase and the location becomes more accurate (this is not necessarily always like this, but the presence of orography, determining the low-level flow, makes the convection more “predictable” in the present case.

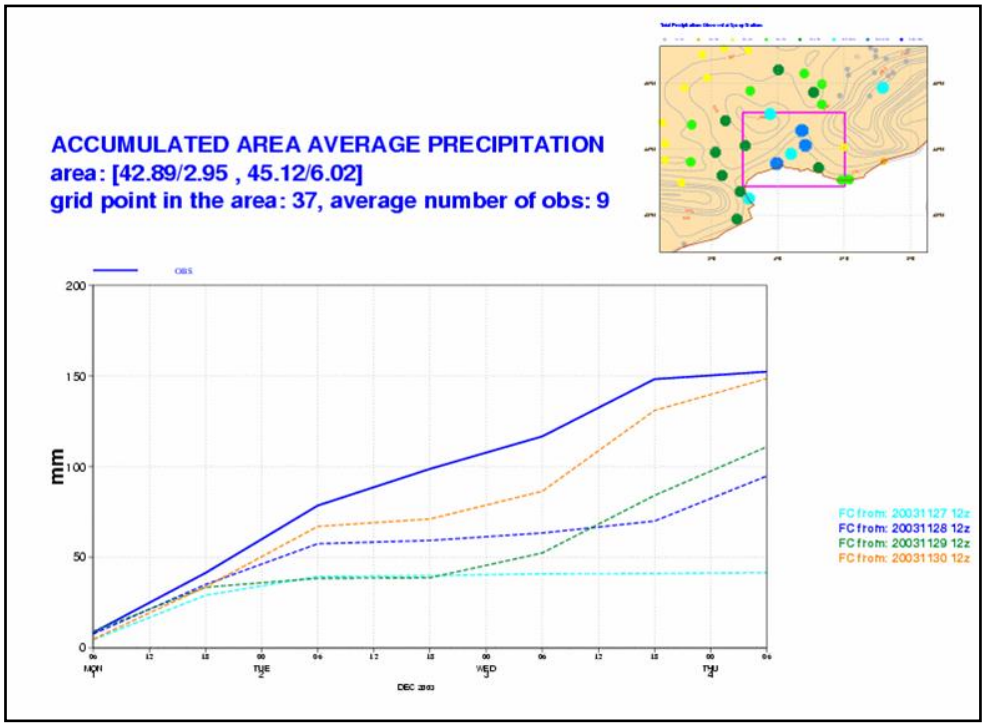

Figure 4.3: Accumulated area averaged precipitation as observed (solid blue line), and obtained from deterministic IFS forecasts starting 27, 28, 29 and 30 November 2003, respectively. The observations and the area are depicted in the small window in the upper right corner.

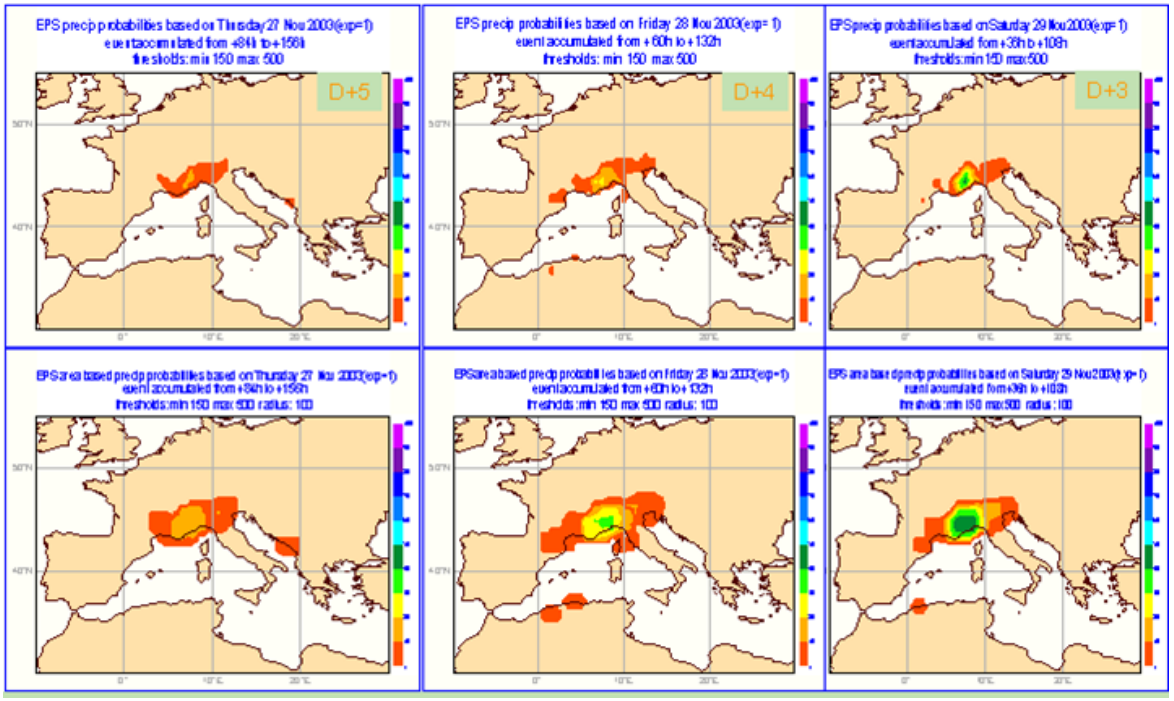

Figure 4.4: Probabilities that 72 h accumulated precipitation exceeds 150 mm, from ensemble system for different forecast lead dates. The second row means the same as the first row, but the search radius for the event to occur is 100 km, and not only limited to the grid point itself.

4.2 Convective adjustment

The next example illustrates the convective adjustment occurring in forced continental convection. The satellite picture from 4 July 2001 16 UTC (Figure 4.5), and the ECMWF analysis (Figure 4.6) from 12 UTC show a trough over the Golf of Biskaya generating advection of moist and warm air from the south-west and south-east. High low-level θ_e values, combined with upper-level divergence, and strong large-scale lifting at 700 hPa, occur over the south-west of France, where convective clusters, actually bringing hail, can be identified on satellite image. The clusters exhibit the typical south-west north-east orientation that is characteristic for northern hemisphere middle latitude convection.

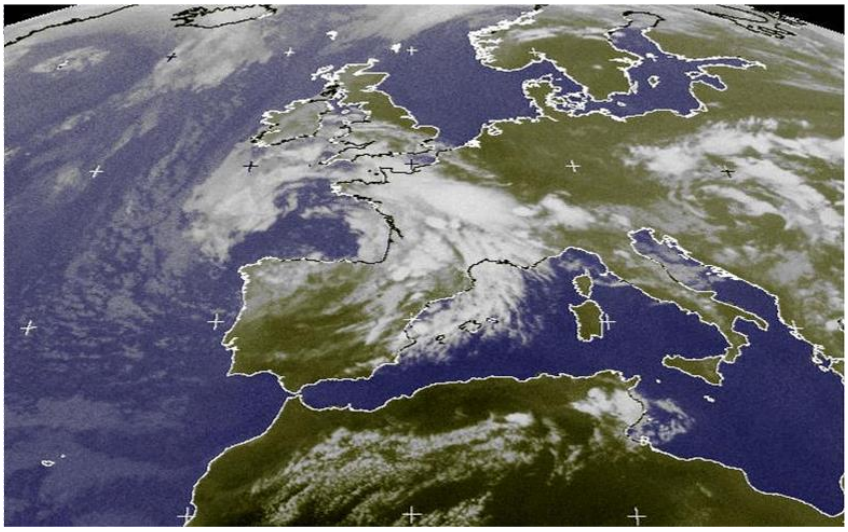

Figure 4.5: Meteosat satellite image from 4 July 2001, 12 UTC (Courtesy http://www.wetterzentrale.de).

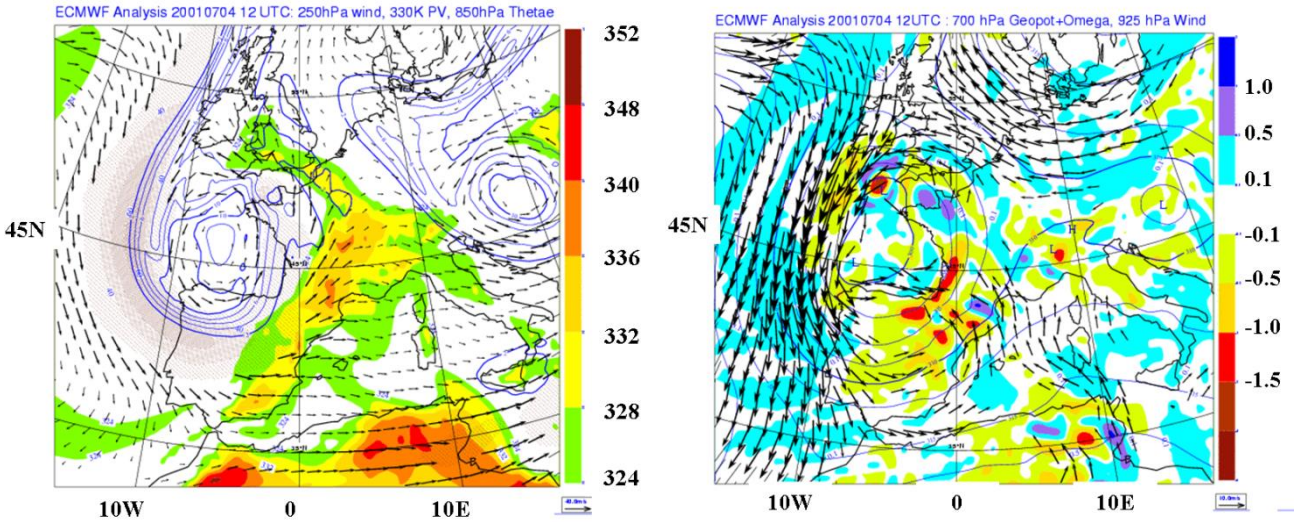

Figure 4.6: ECMWF Analysis for 4 July 2001 12 UTC Left: 330 K PV (blue isolines), 250 h wind vectors + isotachs (grey shaded), and 850 hPa θ_e (colour shaded). Right: 700 hPa Geopotential (black isolines), 925 hPa wind vectors, and 700 hPa ω (Pa/s).

In order to illustrate the adjustment process, we consider the observed soundings at Bordeaux-Merignac in southwest France for 4 July 2001 at 00 and 12 UTC (Figure 4.7). The 00 UTC sounding, prior to the convective event, shows between 850 and 600 hPa a layer with hot south-westerly flow, also the 200 hPa westerly flow is pronounced. In contrast, in the 12 UTC sounding that has been taken during or just after the convective event, this warm unstable layer of air disappeared, the lower atmosphere has been cooled by evaporation of precipitation, and advection of colder air, whereas the upper-troposphere has been moistened through convective transport and large-scale ascent in the convective regions. The resulting stratification of the troposphere is close to moist adiabatic.

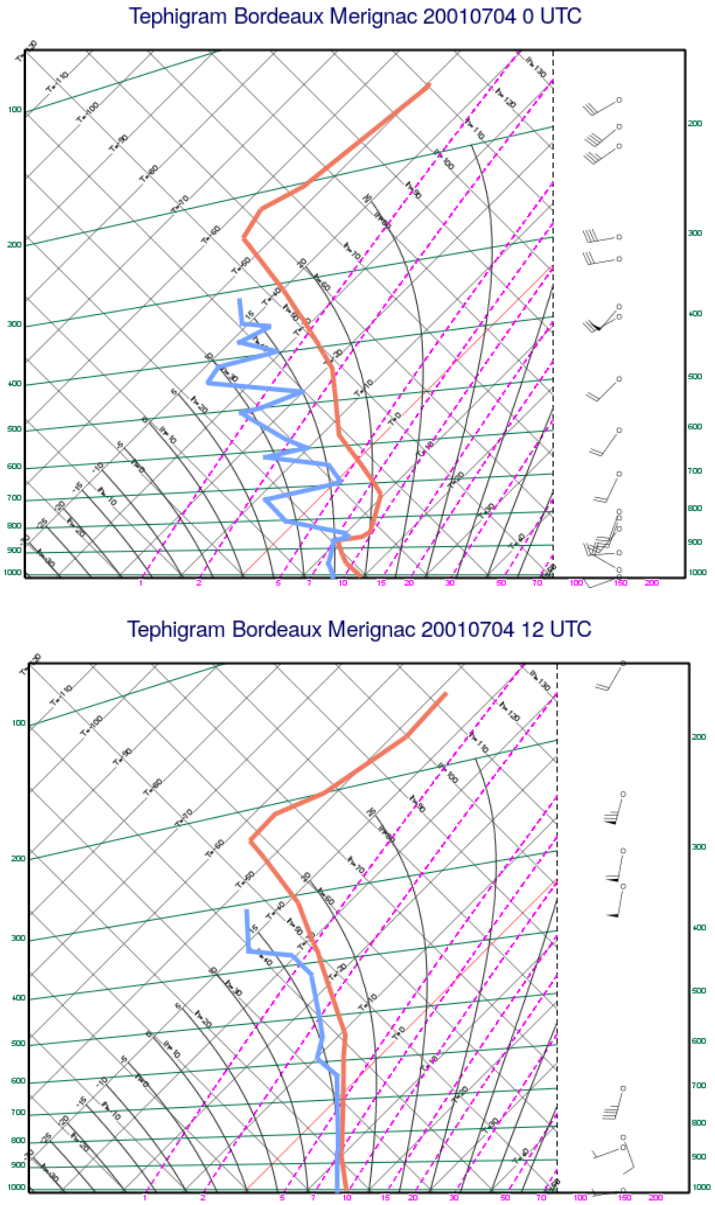

Figure 4.7: Tephigrams of observed soundings at Bordeaux-Merignac (France) for 4 July 2001 00 UTC (top), and 12 UTC (bottom): Temperature (orange-red) and dewpoint temperature (blue).

4.3 Partly orographically forced convection over Iberian Peninsula

The last example treats a case with relatively weak synoptic forcing, where the role of surface fluxes and orography becomes more important. The ECMWF analysis for 2 July 2001 6 UTC (Figure 4.8) shows a distinct PV anomaly with a strong Jet at its western flank extending from Scandinavia, over eastern Germany, to Italy. The corresponding infrared Meteosat satellite Figure 4.9a image shows frontal clouds and convection over Eastern Europe, the Balkans and Greece, below and ahead of the PV anomaly. However, a weak PV anomaly is also present over the north-western part of the Iberian Peninsula. As over this area also relatively high values of θ_e occur, it is a suspected favourable region for convection to occur. Indeed, the satellite image, and also the lightning observations confirm localized convection over this area, especially over the mountainous region (Figure 4.9).

The closest radiosonde observation station available in this area is La Coruña at the Galician coast. The radiosonde data for 2 July 2001 11 UTC (Figure 4.10) shows relatively cold air at low levels, below 900 hPa, a relatively dry, and dry-adiabatically stratified layer between 900 and 700 hPa, topped by a more moist layer between 700 and 500 hPa.. The relatively cold and moist near surface air has certainly been advected from the nearby sea.

Given the sounding, one expects convection only for air parcels departing above 900 hPa. Therefore, convection is more probable over nearby mountainous regions where the necessary parcel lifting is provided to overcome near cloud base convective inhibition. Furthermore, further inland strong surface sensible heat fluxes may sufficiently heat the lower atmospheric layers, thereby reducing the CIN, and increasing the air parcels CAPE. The observations in Figure 4.9 do support these explanations.

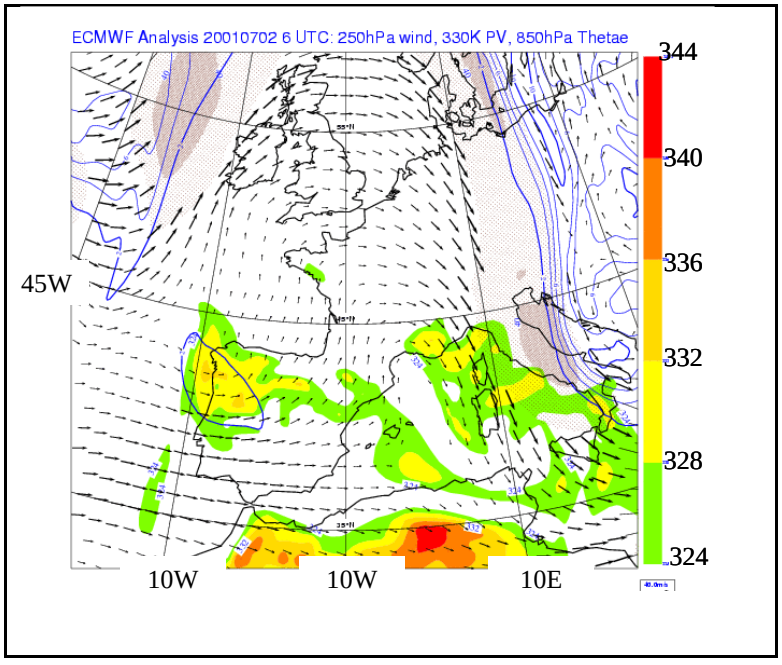

Figure 4.8: ECMWF Analysis of 2 July 2001 6 UTC with 250 hPa wind vectors and isotachs (grey shaded areas), 330 K PV (blue isolines), and 850 hPa θ_e (coulour shaded).

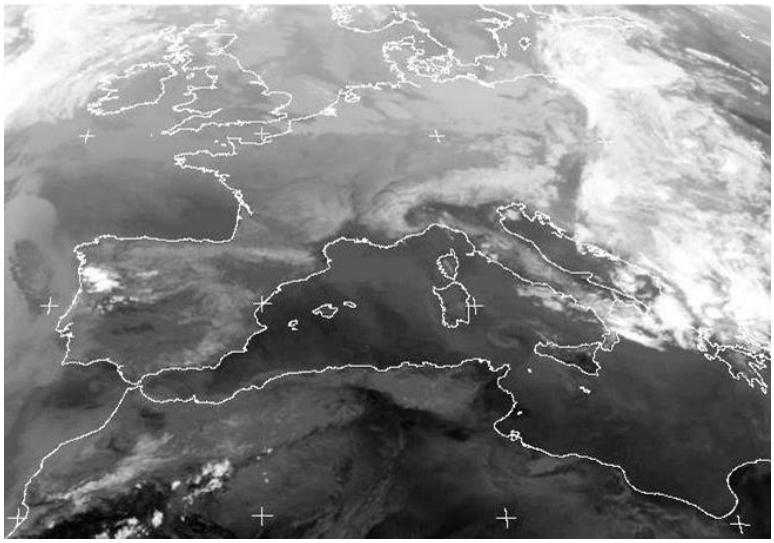

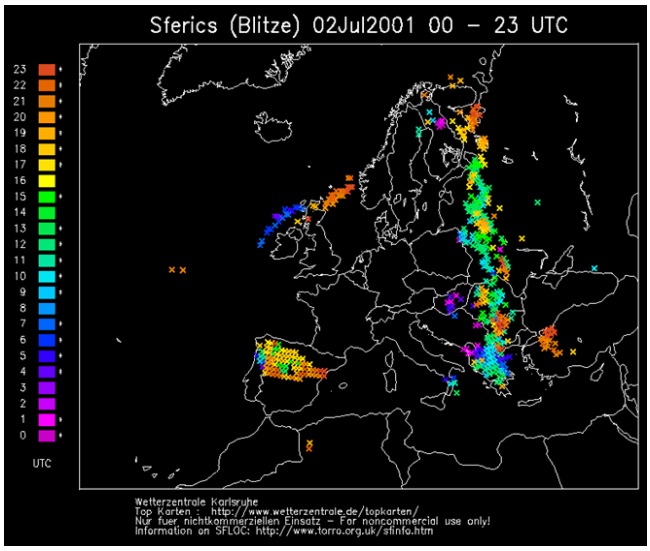

Figure 4.9: (Top) Infrared Meteosat image for 2 July 2001 (Courtesy Dundee satellite receiving station), and (bottom) lightning observations as a function of time (Courtesy http://www.wetterzentrale.de).

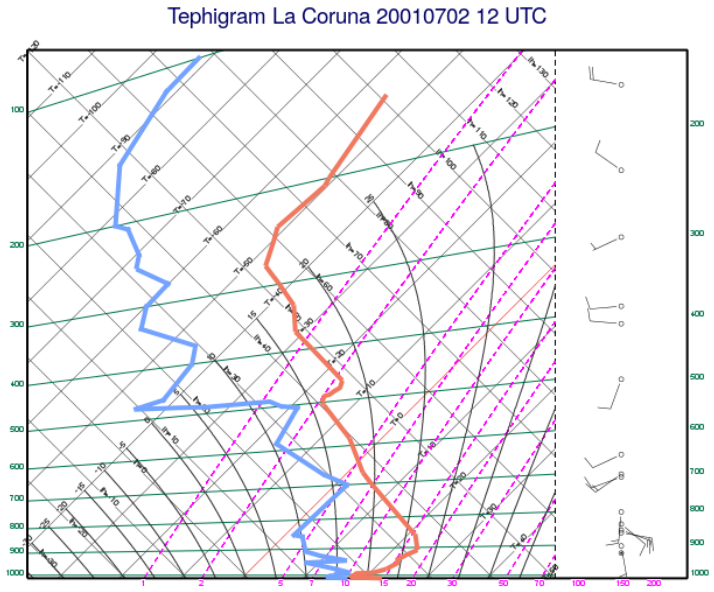

Figure 4.10: Tephigram showing radiosonde data at La Coruña for 2 July 2001 11 UTC.

4.4 Forecasted satellite imagery

Since 2005 ECMWF also provides forecasted satellite images for the first 120h of the deterministic forecast. These "synthetic" satellite images are generated with the aid of a radiative transfer model (RTTOVS = Radiative Transfer model for TOVS, ATOVS, and several other atmospheric sounders) that computes the radiation a satellite would see in a certain spectral band, given the atmosphere forecasted by the model (*p, T, q* and cloud condensate). Forecasted satellite images are only available for the water vapour and infrared spectral bands as complications would arise for the visible band due to angle geometry and unknown surface emissivities. The synthetic satellite images also allow for a very useful evaluation of the forecast in terms of clouds, cloud top heights, and cloud optical thickness (actually brightness temperatures).

As a first example is shown in Figure 4.11 a comparison between Meteosat 9 observed and forecasted water vapour images (brightness temperatures in water vapour window channel) from a short range forecast)of a record deep cyclone over the North-Eastern Atlantic on 8 October 2010. The example documents both the capability of the analysis and forecast system to represent the dry (black) and moist (grey/white) banding and filament structures in midlatitude cyclones. The model was even able to represent the cold frontal structure with embedded mesoscale convective systems off the Portuguese coast.

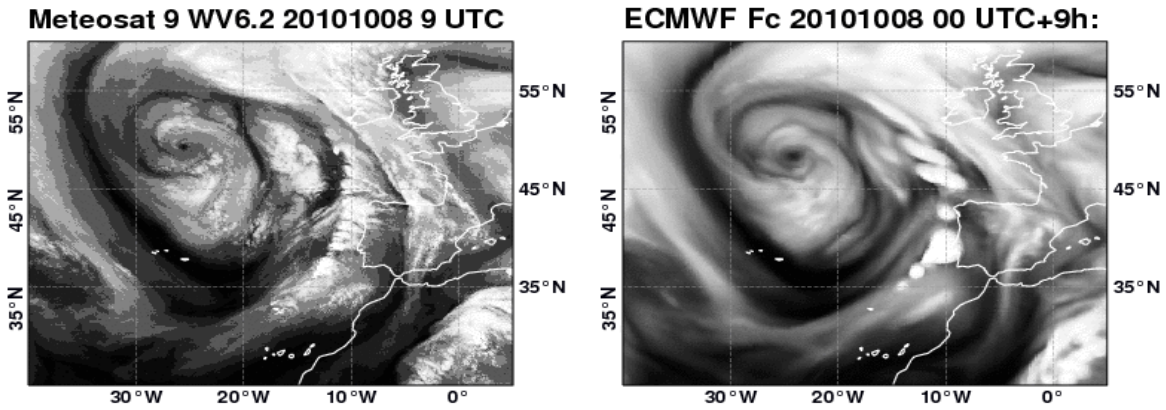

Figure 4.11: Meteosat 9 water vapor channel (left), and corresponding forecasted satellite images by the IFS T1279 operational system for 8 October 2010 09 UTC. Forecast start date is 8 October 00 UTC.

Finally, in Figure Figure 4.12 are provided in a full disk satellite view the Meteosat 9 image (SEVIRI imager at 5 km horizontal resolution) corresponding to the infrared window channel brightness temperatures for 10 January 2014 15 UTC and the forecast satellite image from the IFS T1279 (16 km) high-resolution system with the forecast starting at 00 UTC.

The model does a good job in representing the middle latitude synoptic systems as well as the oceanic trade-wind and stratocumulus area. As expected, tropical convection is more difficult as it is less 'organized' . However, the model is able to represent the gross features of the tropical rain systems including the land sea contrast and the diurnal cycle. One of the remaining weaknesses of the current forecast system is that summertime convection during evening/night dies out earlier than in observations.

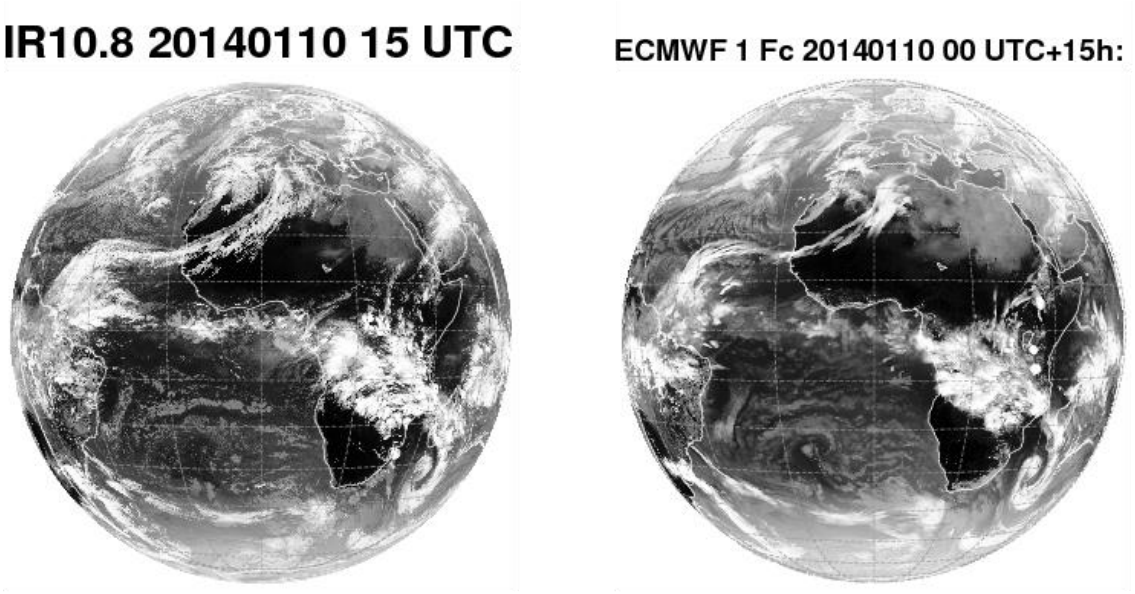

Figure 4.12: Meteosat 9 observed infrared satellite image (left) and forecasted satellite image by the IFS T1279 operational system for 10 January 2014 15 UTC, with forecast starting at 00 UTC.

Acknowledgements

I like to express my gratitude to King-Fai Li (Cal Tech), Nedjelka Žagar (Uni Ljubljana) and Michael Herman (New Mexic Institute) for the various spectral filtering softwares, Anton Beljaars for the diurnal cycle software, Linus Magnusson for climate diagnostics, J. Kain (NOAA/NSSL) for material on the Betts-Miller scheme as used at NCEP, Federico Grazzini for the precipitation analysis in Chapter 4, and Els Kooij-Connally for invaluable help in typewriting the manuscript. I also warmly thank my colleagues Martin Steinheimer and Noureddine Semane for many discussions.

5 Appendix: Simple wave types and quasi-geostrophic adjustment

The discussion of simple linear wave types and motions that play a role in convection and the convective adjustment of the atmosphere closely follows Andrews et al (1987, Holton (2004, pp. 192 ff), Wheeler and Nguyen, and Verkley and van der Velde (2010). The discussion is far from being complete, and is only intended to provide some insight and the standard technical tools.

5.1 Shallow water gravity waves

Assuming hydrostatic flow of two incompressible fluids with constant densities in a two-dimensional plane (Figure 5.1), the *x* momentum and continuity equations for the lower layer write

$$\frac{\partial u}{\partial t}+u\frac{\partial u}{\partial x}+w\frac{\partial u}{\partial z}=-\frac{1}{\rho_1}\frac{\partial p}{\partial x}=-g\frac{\delta\rho}{\rho_1}\frac{\partial h}{\partial x};\quad \delta\rho=\rho_1-\rho_2$$
$$\frac{\partial u}{\partial x}+\frac{\partial w}{\partial z}=0. \tag{5.1}$$

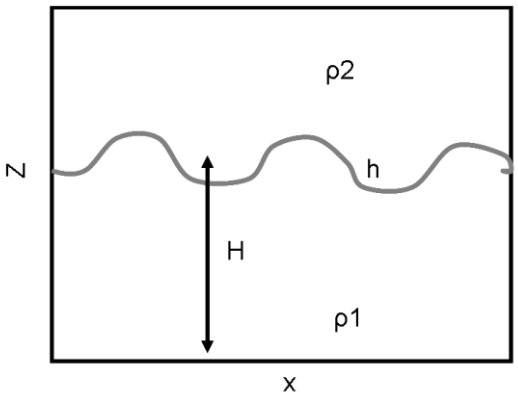

Figure 5.1: Vertical Cross section of a two-layer fluid with undulations at their interface.

As the densities are invariant, the pressure gradient is independent of height, so is *u* and the continuity equation can be integrated to

$$w(h)-w(0)=-\frac{\partial u}{\partial x}h \tag{5.2}$$

with $w(0)=0$ at the surface, and $w(h)$ corresponding to the rate of change of the upper surface

$$w(h)=\frac{dh}{dt}=\frac{\partial h}{\partial t}+u\frac{\partial h}{\partial x}=-\frac{\partial u}{\partial x}h\Rightarrow\frac{\partial h}{\partial t}+\frac{\partial}{\partial x}(hu)=0 \tag{5.3}$$

Applying now the perturbation technique around the constant basic state flow $\bar{u}$ and the average fluid height *H* (e.g. the tropopause height or the depth of a lake or the Sea)

$$u=\bar{u}+u';\quad h=H+h' \tag{5.4}$$

the equation system can be linearized (neglecting products of prime quantities) to

$$\frac{\partial u'}{\partial t}+\bar{u}\frac{\partial u'}{\partial x}=-g\frac{\delta\rho}{\rho_1}\frac{\partial h'}{\partial x}$$
$$\frac{\partial h'}{\partial t}+\bar{u}\frac{\partial h'}{\partial x}+H\frac{\partial u'}{\partial x}=0 \qquad (5.5)$$

and through elimination reduced to a single wave equation

$$\left(\frac{\partial}{\partial t}+\bar{u}\frac{\partial}{\partial x}\right)^2 h'-gH\frac{\delta\rho}{\rho_1}\frac{\partial^2 h'}{\partial x^2}=0. \qquad (5.6)$$

Searching a solution of the form

$$h'=A\exp\left[ik(x-ct)\right] \qquad (5.7)$$

the phase speed *c* is obtained as

$$c=\bar{u}\pm\sqrt{gH\frac{\delta\rho}{\rho_1}} \qquad (5.8)$$

from which follows that the deeper H the higher the phase speed, also the waves are non-dispersive as *c* is independent of *k*. In the case that the lower fluid is water (a lake or the Sea) and the upper fluid is the atmosphere ($\rho_1 \gg \rho_2$) the phase speed is $c=\bar{u}+\sqrt{gH}$ which is also the phase speed for a Tsunami wave.

5.2 Quasi-geostrophic adjustment

In addition to the previous case, we now consider larger-scale motions of the atmosphere, in particular midlatitude synoptic-scale systems where the momentum and mass distributions have been perturbed (e.g. through a strong convective heat/mass source), and the return to geostrophy is assured through excitation of waves. This problem has been first solved by G. Rossby (1930). Again for simplicity the shallow water equation system is considered, but this time on a rotating plane using a constant Coriolis parameter f_0; the background basic state wind is set to zero, and the atmospheric scale height *H=R T/g*

$$\frac{\partial u'}{\partial t}-f_0 v'=-g\frac{\partial h'}{\partial x}$$
$$\frac{\partial v'}{\partial t}+f_0 u'=-g\frac{\partial h'}{\partial y} \qquad (5.9)$$
$$\frac{\partial h'}{\partial t}+H\left(\frac{\partial u'}{\partial x}+\frac{\partial v'}{\partial y}\right)=0$$

Taking $\partial/\partial x$ of (5.9)a, and $\partial/\partial y$ of (5.9)b, and substituting into the third, one obtains

$$\frac{\partial^2 h'}{\partial t^2}-c^2\left(\frac{\partial^2 h'}{\partial x^2}+\frac{\partial^2 h'}{\partial y^2}\right)+Hf_0\varsigma'=0 \qquad (5.10)$$

with $c=\sqrt{gH}$ and $\varsigma = \partial v/\partial x - \partial u/\partial y$ is the vorticity, which constitutes an equation coupling changes in height (mass) to vorticity (wind) perturbations. However, it is possible to further simplify. Taking $-\partial/\partial y$ of (5.9)a and $\partial/\partial x$ of (5.9)b and adding them one obtains

$$\frac{\partial \varsigma'}{\partial t} + f_0 \delta = 0; \quad \delta = \frac{\partial u'}{\partial x} + \frac{\partial v'}{\partial y} \tag{5.11}$$

where δ is the divergence. Furthermore, adding (5.11) to (5.9)c gives

$$\frac{\partial}{\partial t}\left(\varsigma' - \frac{f_0}{H} h'\right) = 0 \quad \Rightarrow \varsigma' - \frac{f_0}{H} h' = cste \tag{5.12}$$

Considering now an ideal case where ς' is initially zero and the height perturbation corresponds to a step function $h' = -h_0 \mathrm{sign}(x)$ then with the aid of (5.12) $cste = h_0/H\,\mathrm{sgn}(x)$ and the specified initial condition, (5.10) writes

$$\frac{\partial^2 h'}{\partial t^2} - c^2\left(\frac{\partial^2 h'}{\partial x^2} + \frac{\partial^2 h'}{\partial y^2}\right) + f_0^2 h' = -f_0^2 h_0 \mathrm{sgn}(x) \tag{5.13}$$

As initially h' is independent of *y* it remains so, and the equilibrium solution as a function of *x* can be found from

$$c^2 \frac{\partial^2 h'}{\partial x^2} + f_0^2 h' = -f_0^2 h_0 \mathrm{sgn}(x) \tag{5.14}$$

as

$$\begin{aligned} h' &= h_0[-1 + \exp(-f_0/c\,x)]; \quad x \geq 0 \\ h' &= h_0[+1 - \exp(+f_0/c\,x)]; \quad x < 0 \end{aligned} \tag{5.15}$$

which satisfies $h'(\pm\infty) = 0$ and $h'(0) = 0$ for continuity; $c/f_0 = \sqrt{gH}/f_0$ is the Rossby radius of deformation. Finally, from (5.12) can be computed the wind perturbation

$$u' = 0; \quad v' = \int \varsigma' dx = \sqrt{g\,h_0^2/H}\,\exp\left(-f_0/c|x|\right) \tag{5.16}$$

A graphical illustration of (5.15) and (5.16) is given in Figure 5.2 using H=10^4 m, f_0=10^{-4} s^{-1} and h_0=50 m.

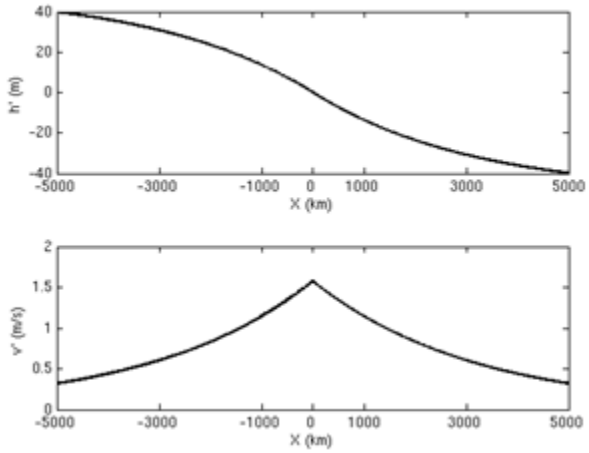

Figure 5.2: "Adjusted" height and velocity perturbations as a function of horizontal distance. Note that the gradient of the height (pressure) field is continuous but the gradient of the wind field has a discontinuity.

5.3 Tropical linear waves

Tropical linear waves can also be derived using the shallow water equation system above with zero background wind, but this time on the β-plane, where $f = 2\Omega\sin\phi = 2\Omega a^{-1}y = \beta y$ with *a* the radius and Ω the rotation rate of the Earth, and *H* is the equivalent depth

$$\begin{aligned}
&\frac{\partial u'}{\partial t} - fv' = -g\frac{\partial h'}{\partial x} \\
&\frac{\partial v'}{\partial t} + fu' = -g\frac{\partial h'}{\partial y} \\
&\frac{\partial h'}{\partial t} + H\left(\frac{\partial u'}{\partial x} + \frac{\partial v'}{\partial y}\right) = 0
\end{aligned} \tag{5.17}$$

Note that this derivation implies "dry" waves but it is also useful for convectively coupled waves which will propagate however more slowly. Seeking solutions in the form of zonally propagating waves

$$\psi' = \mathrm{Re}\{\hat{\psi}(y)\exp[i(kx-\omega t)]\};\ \psi \in (u, v, h) \tag{5.18}$$

gives

$$\begin{aligned}
&-i\omega\hat{u} - \beta y\hat{v} = -ikg\hat{h} \\
&-i\omega\hat{v} + \beta y\hat{u} = -g\frac{d\hat{h}}{dy} \\
&-i\omega\hat{h} + H\left(ik\hat{u} + \frac{d\hat{v}}{dy}\right) = 0
\end{aligned} \tag{5.19}$$

By elimination this set of equations can be reduced to a single equation for *v*

$$\frac{d^2\hat{v}}{dy^2} + \left(\frac{\omega^2}{gH} - k^2 - \frac{k}{\omega}\beta - \frac{\beta^2 y^2}{gH}\right)\hat{v} = 0 \tag{5.20}$$

The desired solution is a wave that decays away from the Equator. Solutions to this wave equation, which is similar to the one-dimensional Schrödinger equation in Physics, under the given boundary-condition are Hermite Polynomials H_n of the normalised meridional direction y^*

$$\hat{\psi}(y) = \begin{bmatrix} 1 \\ 2y^* \\ 4y^{*2} - 2 \\ : \\ H_n(y^*) \end{bmatrix} e^{-y^{*2}/2}; \quad y^* = y\sqrt{\frac{\beta}{gH}} \tag{5.21}$$

so that the dispersion relation $\omega(k)$ becomes

$$\left(\frac{\omega^2}{gH} - k^2 - \frac{k}{\omega}\beta\right)\frac{\sqrt{gH}}{\beta} = 2n+1; \quad n = 0,1,2,.. \tag{5.22}$$

which has three roots and where n is the number of nodes in the y direction. Some roots can be computed analytically by example considering only low frequencies which allows to neglect the first term of the lhs. This becomes then the dispersion relation for the westward propagating equatorial Rossby waves

$$\omega_{Rossby} \approx \frac{-\beta k}{k^2 + (2n+1)\beta/\sqrt{gH}} \tag{5.23}$$

Note that only for k<0 (westward propagation) we have ω>0.

Considering only high frequencies so that the term $-k\beta/\omega$ can be neglected one obtains the Dispersion relation for the eastward and westward propagating inertia gravity waves

$$\omega_{IG} = \pm\left((2n+1)\beta\sqrt{gH} + k^2 gH\right)^{1/2} \tag{5.24}$$

The equatorial Kelvin wave is a special solution for $v=0$. Its dispersion relation can be derived from (5.17) using $v=0$, but can be also recovered by setting $n=-1$. Its dispersion relation is simple that of a gravity wave of phase speed c

$$\omega_{Kelvin} = ck = \sqrt{gH}\,k \tag{5.25}$$

Therefore, Kelvin waves are non-dispersive waves with their phase speed $c=\omega/k$ equal to the group speed $c_g = \partial\omega/\partial k$. Note that once the solution for v is known one can compute by substitution the ones for u and h, also note that as the shallow water system (5.17) is linear all linear combinations of the different solutions are also a solution to the system. In the simplest case of the Kelvin wave with v'=0 this becomes

$$\begin{aligned} u' &= \hat{u}\exp(-y^*/2)\,\mathrm{Re}\{\exp[i(kx-\omega t)]\}\times G(z) \\ h' &= g^{-1}\omega/k\,\hat{u}\exp(-y^*/2)\,\mathrm{Re}\{\exp[i(kx-\omega t)]\}\times G(z) \end{aligned} \tag{5.26}$$

For a set of solutions for all waves see Verkley and van der Velde (2010). Here we have also made use of the principle of separation of variables and introduced the final missing dependency, namely the propagation of vertical modes using the vertical structure function $G(z)$

$$G(z) = \exp(-z/2H_s)\,\mathrm{Re}\{\exp(imz)\} \tag{5.27}$$

with $m=2\pi/l_z$ is the vertical wave number and H_s is the atmospheric scale height of O(RT/g). The dispersion relation for the vertical direction is obtained from the vertical structure equation which solutions are also known as Hough functions (see Žagar et al. 2005)

$$\frac{1}{\rho_0}\frac{d}{dz}\left(\rho_0\frac{dG}{dz}\right)+\frac{N^2}{gH}G=0; \quad \frac{d\ln\rho_0}{dz}=-\frac{1}{H_s} \tag{5.28}$$

where N is the buoyancy frequency, so that m becomes

$$m=\left(\frac{N^2}{gH}-\frac{1}{4H_s^{\,2}}\right)^{1/2}; \quad N^2=\frac{R}{H_s}\frac{d\theta_0}{dz} \tag{5.29}$$

Interestingly, this links the vertical wave number to the equivalent depth H of the wave.

The different theoretical modes in the ω-k domain are illustrated in Figure 5.3 for the outgoing longwave radiation from the ECMWF operational analysis from 2008-2013 and an ensemble of 1-year integrations from 2001-2009 with Cy40r1 (2014). The figure is similar to Figure 1.13 but both the symmetric and anti-symmetric part are shown and a different method is employed to isolate the modes from their own background spectrum (wave analysis package courtesy Michael Hermann New Mexico Institute).

Through a regression method one can also extract the vertical structure of the different modes. In particular for each variable all the time series at each latitude band and level are regressed to the point with maximum OLR variance (with OLR having been spectrally filtered for the specific mode and then transformed back to physical space). An example of the composite temperature, u-wind and specific humidity anomalies are shown in Figure 5.4 for the MJO mode (top row) and the Kelvin wave mode (bottom row). The MJO anomalies are significantly larger than the kelvin mode anomalies. However, both the MJO and Kelvin mode anomalies show the characteristic baroclinic westward tilt with height of the anomalies in the troposphere, the tilt in the anomalies is reverted in the stratosphere for the Kelvin mode – note that contrary to the Rossby waves that have westward phase and are absorbed in the upper troposphere by the prevailing easterly (westward) winds speed, the Kelvin waves with easterly phase speed can propagate through the stratosphere.

Finally, note the large westerly wind anomaly behind the main MJO convection in the lower troposphere, and the significant lower tropospheric moist anomalies for both the MJO and the Kelvin waves ahead and during the convective phase.

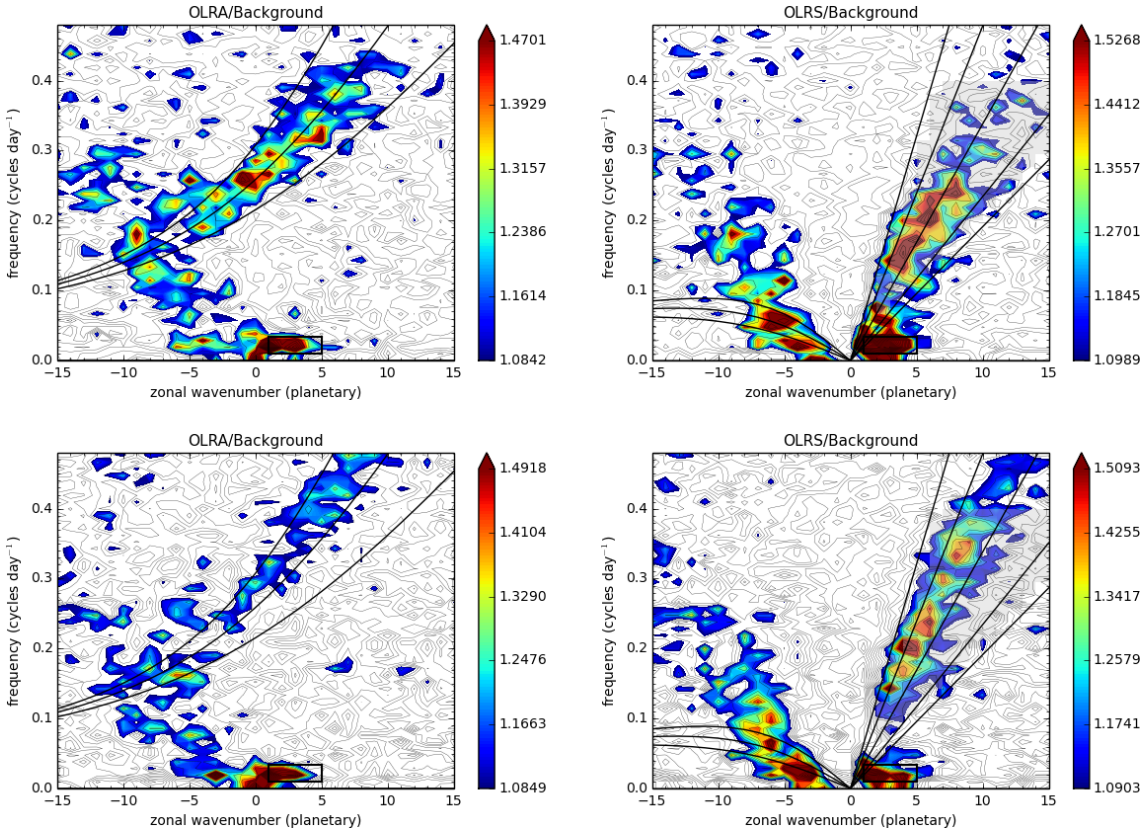

Figure 5.3: Similar to Figure 1.13 wavenumber-Frequency diagrams of OLR from the operational ECMWF analysis (top) and from seasonal integrations with Cy40r1 (2014) (bottom) for both the anti-symmetric (left column) and symmetric part of the spectrum (right column). Spectra have been divided by a background spectrum computed for each data set through smoothing of the raw spectra. Spectral Analysis Software courtesy Michael Herrmann (New Mexico Institute, Socorro). The model realistically represents the Kelvin, MJO and Rossby modes (the MJO mode is highlighted by a box) but somehow lacks the Eastward Inertial Gravity wave activity in the anti-symmetric part of the spectrum.

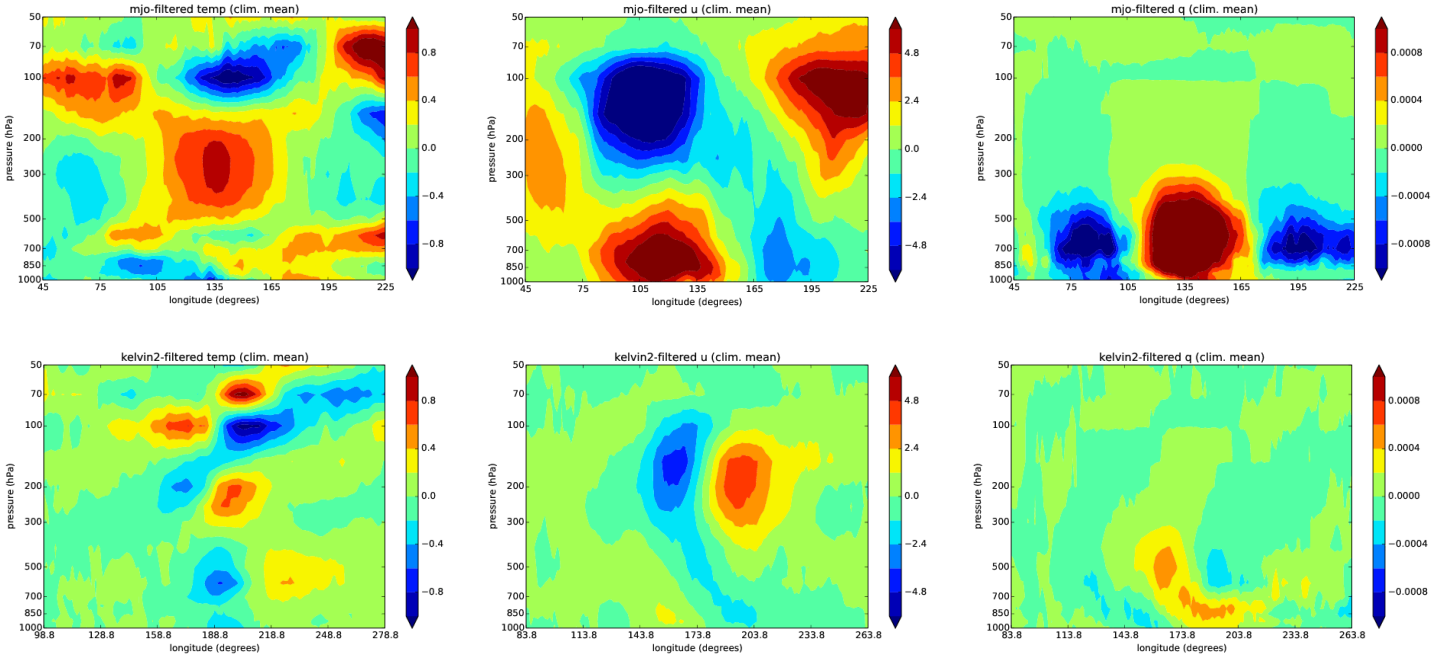

Figure 5.4: Composite of - from left to right - T (K), u (m s^{-1}) and q (g kg^{-1}) anomalies for the MJO mode, top row, and the Kelvin wave mode, bottom row, from the ECMWF operational analysis. The composites are obtained by regression of the time series onto the point with maximum OLR variance in either the MJO or Kelvin spectral bands –courtesy Michael Hermann for the wave analysis package.

References

Andrews, D.G, J.R. Holton and C.B. Leovy, 1987: Middle Atmosphere Dynamics. New York. Academic Press

Arakawa, A. and W. Schubert, 1974: Interaction of a cumulus ensemble with the large-scale environment. Part I. *J. Atmos. Sci.,* **31,** 674-701.

Arakawa, A., 2004: The cumulus parameterization problem: Past, present, and future. *J. Climate,* **17,** 2493-2525.

Bechtold, P., E. Bazile, F. Guichard, P. Mascart and E. Richard, 2001: A mass-flux convection scheme for regional and global models. *Quart. J. Roy. Meteor. Soc.,* **127,** 869-886.

Bechtold, P. and E. Bazile, 2001: The 12-13 November 1999 flash flood in southern France. *J. Atmos. Res.,* **56,** 171-189.

Bechtold, P., F. Lalaurette, A. Ghelli and M. Miller, 2003: Forecasts of severe convection. *ECMWF Newsletter,* No. **98**, 8-16.

Bechtold, P., J.-P. Chaboureau, A. Beljaars, A. K. Betts, M. Köhler, M. Miller and J.-L. Redelsperger, 2004: The simulation of the diurnal cycle of convective precipitation over land in a global model. *Quart. J. Roy. Meteor. Soc.,* **130,** 3119-3137.

Bechtold, P., M. Köhler, T. Jung, M. Leutbecher, M. Rodwell and F. Vitart, 2008a: Advances in simulating atmospheric variability with IFS cycle 32r3. ECMWF Newsletter, No. **114**, 29-38.

Bechtold, P., M. Köhler, T. Jung, F. Doblas-Reyes, M. Leutbecher, M. Rodwell, F. Vitart and G. Balsamo, 2008b: Advances in simulating atmospheric variability with the ECMWF model: From synoptic to decadal time-scales. *Quart. J. Roy. Meteor. Soc.* **134,** 1337-1351. Also available as *ECMWF Technical Memorandum* **No 556**.

Bechtold, P., 2008c: Convection parametrization. ECMWF Seminar proceedings on "The parametrization of subgrid physical processes", 63-85. also available under *http://www.ecmwf.int/publications /library/ do/ references/list/200809* .

Bechtold, P., N. Semane, P. Lopez, J.-P. Chaboureau, A. Beljaars and N. Bormann, 2014 : Representing equilibrium and non-equilibrium convection in large-scale models. *J. Atmos. Sci*, **71,** 734-753.

Betts, A. and F. J. Dugan, 1973: Empirical formula for saturation pseudoadiabats and saturation equivalent potential temperature. *J. Atmos. Sci.,* **12,** 731-732.

Betts, A. K. and M. Miller, 1986: A new convective adjustment scheme. Part II: Single-column tests using GATE wave, BOMEX, ATEX, and acrtic-air mass data sets. *Quart. J. Roy. Meteor. Soc.,* **112,** 693-709.

Bjerknes, J., 1938: Saturated ascent of air through a dry-adiabatically descending environment. *Quart. J. Roy. Meteor. Soc.,* **64,** 325-330.

Bougeault, P., 1985: A simple parameterization of the large-scale effects of cumulus convection. *Mon. Wea. Rev.,* **113,** 2108-2121.

Bretherton, C. S. and P. Smolarkiewicz, 1989: Gravity waves, compensating subsidence and detrainment around cumulus clouds. *J. Atmos. Sci.,* **46,** 740-759.

Brown, R. G. and C. S. Bretherton, 1997: A test of the strict quasi-equilibrium theory on long time and space scales. *J. Atmos. Sci.,* **54,** 624-638.

Caniaux, G., J.-L. Redelsperger and J.-P. Lafore, 1994: A numerical study of the stratiform region of a fast-moving squall line. Part I: General description and water and heat budgets. *J. Atmos. Sci.,* **51,** 2046-2074.

Carpenter, R. L. Jr, K. K. Droegemeier and A. M. Blyth, 1998: Entrainment and detrainment in numerically simulated cumulus congestus clouds. Part II: Cloud budgets. *J. Atmos. Sci.,* **55,** 3433-3439.

Chaboureau, J.-P., F. Guichard, J.-L. Redelsperger and J.-P. Lafore, 2004: the role of stability and moisture in the diurnal cycle of convection over land. *Quart. J. Roy. Meteor. Soc.,* **130,** 3105-3117.

Cheinet, S., 2004: A multiple mass flux parameterization for the surface-generated convection. Part II: Cloudy cores. *J. Atmos. Sci.,* **61,** 1093-1113.

Cheng, L., T.-C. Yip and H.-R. Cho, 1980: Determination of mean cumulus cloud vorticity from GATE A/B-scale potential vorticity budget. *J. Atmos. Sci.,* **37,** 797-811.

Chikira, M. and M. Sugiyama, 2010: A cumulus parameterization with state-dependent 6 entrainment rate. Part I: Description and sensitivity to temperature and humidity profiles. *J. Atmos. Sci.,* **67,** 2171-2193.

Cho, H.-R., 1997 and D. Pendlebury: Wave CISK of equatorial waves and the vertical distribution of cumulus heating. *J. Atmos. Sci.,* **54,** 2429-2440.

Cho, H.-K., K. P. Bowman, G. R. North, 2004: Equatorial waves including the Madden-Julian oscillation in TRMM rainfall and OLR data. *J. Climate,* 17, 4387-4406.

Clark, A.J., W. A. Gallus Jr., and T.-C. Chen, 2007: Comparison of the diurnal precipitation cycle in convection-resolving and non-convection-resolving mesoscale models. *Mon. Wea. Rev*., **135**, 3456-3473.

Diedhiou, A., S. Janicot, A. Viltard and P. de Felice, 1999: Easterly wave regimes and associated convection over West Africa and tropical Atlantic: Results from the NCEP/NCAR and ECMWF reanalyses. *Climate Dyn.,* **15,** 795-822.

Derbyshire, S., I. Beau, P. Bechtold, J.-Y. Grandpeix, J.-M. Piriou, J.-L. Redelsperger, and P. Soares, 2004: Sensitivity of moist convection to environmental humidity. *Quart. J. Roy. Meteor. Soc.,* **130,** 3055-3079.

Derbyshire, S., A. Maidens, S. Milton, R. Stratton and M. Willett, 2011: Adaptive detrainment in a convective parameterization. *Quart. J. Roy. Meteor. Soc.,***137,** 1856-1871.

De Rooy, W.C., P. Bechtold, K. Fröhlich, C. Hohenegger, H. Jonker, D. Mironov, A.P. Siebesma, J. Teixeira and J.-I. Yano, 2013: Entrainment and detrainment in cumulus convection: an overview. *Quart. J. Roy. Meteor. Soc., **139,** 1-19.*

Donner, L. J., 1993: A cumulus parameterization including mass fluxes, vertical momentum dynamics, and mesoscale effects. *J. Atmos. Sci.,* **50,** 889-906.

Donner, L. J.and V. T. Philipps, 2003: Boundary-layer control on convective available potential energy: Implications for cumulus parametrization. *J. Geophys. Res.*, **108,** 4701, doi:10.1029/2003JD003773.

Eitzen, A. Z. and D. A. Randall, 2005: Numerical simulations of interactions between gravity waves and deep moist convection *J. Atmos. Sci.,* **62,** 1480-1496.

Fraedrich, K., 1973: On the parameterization of cumulus convection by lateral mixing and compensating subsidence. Part I. *J. Atmos. Sci.,* 30, 408-413.

Fritsch, J. M. and C. F. Chapell, 1980: Numerical prediction of convectively driven mesoscale pressure system. Part I; convective parameterization. *J. Atmos. Sci.,* **37,** 1722-1733.

Fournier, A. M. A. Taylor and J. J. Tribbia, 2003: The spectral element atmosphere model (SEAM): High resolution parallel computation and localized resolution of regional dynamics. *Mon. Wea. Rev.,* **132,** 726-748.

Fraedrich, K., 1976: A mass budget of an ensemble of transient cumulus clouds determined from direct cloud observations. J. Atmos. Sci., 33, 262-343.

Gerard, L., 2015: Bulk mass-flux perturbation formulation for a unified approach of deep convection at high resolution. *Mon. Wea. Rev.,* **143,** 4038-4063.
Grant, A. L. M., 2001: Cloud-base fluxes in the cumulus-capped boundary layer. *Quart. J. Roy. Meteor. Soc.,* **127,** 407-422.

Gregory, D. and M. Miller, 1989: A numerical study of the parameterization of deep tropical convection. *Quart. J. Roy. Meteor. Soc.,* **115,** 1209-1241.

Gregory, D, R. Kershaw and P. Inness, 1997: Parameterization of momentum transport by convection. II: tests in single-column and general circulation models. *Quart. J. Roy. Meteor. Soc.,* **123,** 1153-1183.

Gregory, D., J.-J. Morcrette, C. Jakob, A. C. M. Beljaars and T. Stockdale, 2000: Revision of convection, radiation and cloud schemes in the ECMWF integrated forecasting system. *Quart. J. Roy. Meteor. Soc.,* **126,** 1685-1710.

Guichard, F., J.-P. Lafore and J.-L. Redelsperger, 1997: Thermodynamical impact and internal structure of a tropical convective cloud system. *Quart. J. Roy. Meteor. Soc.*, **123,** 2297-2324.

Guichard, F. and D. Gregory, 1998: On the ability of cloud parameterizations to represent organized convection: A case study contrasting cloud resolving and single column model realization. WCRP report, *Proceedings of the COARE98 conference*, 7-14 July 1998, Boulder, USA.

Grist, J. P., 2002: Easterly waves over Africa. Part I: The seasonal cycle and contrasts between wet and dry years. *Mon. Wea. Rev.,* **130,** 197-211.

Grabowski, W. W., 2003: MJO-like coherent structures: Sensitivity simulations using the cloud-resolving convection parameterization (CRCP). *J. Atmos. Sci.,* **60,** 847-864.

Herman, M. J., Ž. Fuchs, D. Raymond and P. Bechtold, 2016: Convectively coupled Kelvin waves: from linear theory to global models. *J. Atmos. Sci.,* **73,** 407-428.

Heus, T., G. van Dijk, H.J.J. Jonker, and H.E.A. van den Akker, 2008: Mixing in shallow cumulus clouds studied by lagrangian particle tracking. *J. Atmos. Sci.,* **65,** 2581-2597.

Hoskins, B. J., M. E. McIntyre and A. W. Robertson, 1985: On the use and significance of isentropic potential vorticity maps. *Quart. J. Roy. Meteor. Soc.,* **111**, 877-946.

Hsieh, J.-S. and K. H. Cook, 2005: Generation of African easterly wave disturbances: Relationship to the African Easterly Jet. *Mon. Wea. Rev.,* **133,** 1311-1327.

Hsieh, W. W. and B. Tang, 1998: Applying neural network models to prediction and data analysis in meteorology and oceanography. Bull. Amer. Met. Soc., 79, 1855-1870.

Jakob, C. and A. P. Siebesma, 2003: A new subcloud model for mass-flux convection schemes. Influence on triggering, updraught properties and model climate. *Mon. Wea. Rev.,* **131,** 2765-2778.

Johnson, R. H., T. M. Rickenbach, S. A. Rutledge, P. E. Ciesielski and W. H. Schubert, 1999: Trimodal characteristics of tropical convection. *J. Climate,* **12,** 2397-2418.

Kain, J. S. and J. M. Fritsch, 1990: A one-dimensional entraining/detraining plume model and its application in convective parameterizations. *J. Atmos. Sci.,* **47,** 2784-2802.

Kim, D., A. H. Sobel, E. D. Maloney, D. M. W. Frierson and I-S. Kang, 2011: A systematic relationship between intraseasonal variability and mean state bias in AGCM simulations. *J. Climate*, **24,** 5506-5520.

Kuo, H. L., 1965: On formation and intensification of tropical cyclones through latent heat release by cumulus convection. *J. Atmos. Sci.,* **22,** 40-63.

Kuo, H. L., 1974: Further studies of the parameterization of the influence of cumulus convection on large-scale flow. *J. Atmos. Sci.,* 31, 1232-1240.

Lin, C. and A. Arakawa, 1997: The macroscopic entrainment processes of simulated cumulus ensemble. Part II: Testing the entraining-plume model. *J. Atmos. Sci.,* **54**, 1044-1053.

Lin, C. and A. Arakawa, 2000: Empirical determination of the basic modes of cumulus heating and drying profiles. *J. Atmos. Sci.,* **57**, 3571-3591.

Lin, J. L., M. I. Lee, D. Kim, I. S. Kang and D. M. W. Frierson, 2008: The impacts of convective parameterization and moisture triggering on AGCM-simulated convectively coupled equatorial wave. J. *Climate*, **21,** 883-909.

Liu, J. Y. and H. D. Orville, 1969: Numerical modeling of precipitation and cloud shadow effects on mountain-induced cumuli. *J. Atmos. Sci.,* **26,** 1283-1298.

Kershaw, R. and D. Gregory, 1997: Parameterization of momentum transports by convection. I: Theory and cloud modeling results. *Quart. J. Roy. Meteor. Soc.,* **123,** 1133-1151.

Madden R. A. and P. R. Julian, 1971: Detection of a 40-50 day oscillation in the zonal wind in the tropical Pacific. *J. Atmos. Sci.*, **28,** 702-708.

Manabe, S. and R. Strickler, 1964: Thermal equilibrium of the atmosphere with a convective adjustment scheme. *J. Atmos. Sci.,* **21,** 361-385.

Mapes, B. E., 1997: Equilibrium vs. activation control of large scale variations of tropical deep convection. In *The physics and parameterization of moist atmospheric convection*, R. K. Smith, Ed., Kluwer Academic Publishers*, 321-358.*

Matthews, A. J., 2008: Primary and successive events in the Madden-Julian Oscillation. *Quart J. Roy. Meteorol. Soc.,* **134,** 439-453.

Moorthi, S., and M. J. Suarez, 1992: Relaxed Arakawa Schubert: A parameterization of moist convection for general circulation models. Mon. Wea. Rev., 120, 978–1002

Mohr, K. I. and C. D. Thorncroft, 2006: Intense convective systems in West Africa and their relationship to the African easterly jet. *Quart. J. Roy. Meteor. Soc.,* **132,** 163-176.

Morel, C. and S. Sénési, 2001: A climatology of mesoscale convective systems over Europe using infrared satellite infrared imagery. Part II: characteristics of European mesoscale convective systems. *Quart. J. Roy. Meteor. Soc.,* **128,** 1973-1995.

Nasuno, T., H. Tomita, S. Iga and H. Miura, 2007: Multiscale Organization of Convection Simulated with Explicit Cloud Processes on an Aquaplanet. J. Atmos. Sci., 64, 1902-1921.

Neggers, R. A. J., A. P. Siebesma and H. J. J. Jonker, 2002: A multiparcel method for shallow cumulus convection. *J. Atmos. Sci.,* **59,** 1655-1668.

Nicholson, E. S. and J. P. Grist, 2003: The seasonal evolution of the atmospheric circulation over West Africa and Equatorial Africa. *J. Climate,* **16,** 1013-1030.

Nitta, T. and S. Esbensen, 1974: Heat and moisture budget analyses using BOMEX data. *Mon. Wea. Rev.*, **102**, 17-28.

Park, S., 2014: A unified convection scheme (UNICON). Part I: Formulation. *J. Atmos. Sci.,* **71,** 3902-3930.

Petch, J. C., and A. R. Brown, and M. E. B. Gray, 2002: The impact of horizontal resolution on the simulations of convective development over land. *Quart. J. Roy. Meteor. Soc.,* **28,** 2031-2044.

Piriou, J.-M., J.-L. Redelsperger, J.-F. Geleyn, J.-P. Lafore and F. Guichard, 2007: An approach for convective parameterization with memory: separating microphysics and transport in grid-scale equations. *J. Atmos. Sci.,* **64,** 4127-4139.

Raymond, D. and A. M. Blyth, 1992: Extension of the stochastic mixing model to cumulonimbus clouds. *J. Atmos. Sci.,* **49,** 1968-1983.

Randall, D. A., M. Khairoutdinov, A. Arakawa and W. Grabowski, 2003: Breaking the cloud parameterization deadlock. *Bull. Am. Meteorol. Soc.*, **84**, 1547-1564.

Redelsperger, J.-L., D. B. Parsons and F. Guichard, 2002: Recovery processes and factors limiting cloud-top height following the arrival of a dry intrusion observed during TOGA COARE. J. Atmos. Sci., 59, 2438-2457.

Rossby, C.-G., and collaborators, 1937: Isentropic analysis. *Bull Amer. Meteor. Soc.,* **18,** 201-209.

Shutts, G.J. and M. E. B. Gray, 1999: Numerical simulations of convective equilibrium under prescribed forcing. *Quart. J. Roy. Meteor. Soc.,* **125,** 2767-2787.

Siebesma, A. P. and J. W. M. Cuijpers, 1995: Evaluation of parametric assumptions for shallow cumulus convection. *J. Atmos. Sci.*, **52,** 650-666.

Siebesma, A. P., 1998: Shallow cumulus convection. In *Buoyant convection in geophysical flows*, **513,** E. J. Plate et al. Eds, Kluwer Academic, 441-486.

Shutts, G., 2008: The forcing of large-scale waves in an explicit simulation of deep tropical convection. *Dyn. Atmos. Ocean,* **45,** 1-25.

Simmons, A. J., 1982: The forcing of stationary wave motion by tropical diabatic heating. *Quart. J. Roy. Meteor. Soc.,* **108,** 503-534.

Simpson, J., 1983: Cumulus clouds: interactions between laboratory experiments and observations as foundations for models. pp. 399-412 in *Mesoscale Meteorology*. Eds. D. K. Lilly and T. Gal-Chen. Reidel, Dordrecht, the Netherlands.

Simpson, J. and V. Wiggert, 1969: Models of precipitating cumulus towers. *Mon. Wea. Rev.,* **97,** 471-489.

Slingo, J. M., and K. Sperber, and J.-J. Morcrette, and G. L. Potter, 2001: Analysis of the temporal behavior of convection in the tropics of the European Centre for Medium-range Weather Forecast model. *J. Geophys. Res.*, **97**, 119135.

Sobel, A. H., J. Nilsson and L. M. Polvani, 2001: The weak temperature gradient approximation and balanced tropical moisture waves. *J. Atmos. Sci.,* **58,** 3650-3665.

Stein, J., E. Richard, J.-P. lafore, J.-P. Pinty, N. Ascensio and S. Cosma, 2000: Meso-Nh simulations with grid-nesting and ice-phase parameterization. *Meteorol. Atmos. Phys.,* **72,** 203-221.

Steinheimer, M., M. Hantel and P. Bechtold, 2008: Convection in Lorenz's global energy cycle with the ECMWF model. *Tellus*, **60A**, 1001-1022. Also available as *ECMWF Technical Memorandum* **No 545**.

Steiner, M., R. A. Houze Jr and S. E. Yuter, 1995: Climatological characterization of three dimensional storm structure from operational radar and rain gauge data. *J. Appl. Meteor.*, **34,** 1978-2007.

Sundqvist, H., 1978: A parameterization scheme for non-convective condensation including prediction of cloud water content. *Quart. J. Roy. Meteor. Soc.,* **104,** 677-690.

Tiedtke, M., 1989: A comprehensive mass flux scheme for cumulus parameterization in large-scale models. Mon. Wea. Rev., 117, 1779-1800.

Tompkins, A. M., 2001: Organization of tropical convection in low vertical wind shear: The role of water vapor. *J. Atmos. Sci.*, **58,** 529-545.

Toumazou, V. and J.-F. Cretaux, 2001: Using a Lanczos eigensolver in the computation of empirical orthogonal functions. *Mon. Wea. Rev.,* **129,** 1243-1250.

Vaillancourt, P. A., M. K. Yau and W. W. Grabowski, 1997 : Upshear and downshear evolution of cloud structure and cloud properties. *J. Atmos. Sci.,* **54,** 1203-1217.

Verkley, W.T.M. and I.R. van der Velde, 2010: Balanced dynamics in the Tropics. *Quart. J. Roy. Meteorol. Soc*., **136,** 41-49.

Vitart, F. and F. Molteni, 2010: Simulation of the MJO and its teleconnections in an ensemble of 46-day EPS hindcasts. *Quart. J. Roy. Meteorol. Soc*., **136,** 842-855.

Webster, P. J. and H.-R. Chang, 1988: Equatorial energy accumulation and emanation regions. Impacts of a zonally varying basic state. *J. Atmos. Sci.,* **45,** 803-829.

Wang, S. and B. Stevens, 2000: Top-hat representation of turbulence statistics in cloud-topped boundary layers: A large eddy simulation study. *J. Atmos. Sci.,* **57,** 423-441.

Wheeler, M., G. Kiladis and P. Webster 2000: Large-scale dynamical fields associated with convectively coupled equatorial waves. *J. Atmos. Sci.,* **57,** 613-640.

Wheeler, M. and G. N. Kiladis, 1999: Convectively coupled equatorial waves: Analysis of clouds and temperature in the wavenumber-frequency domain. *J. Atmos. Sci.,* **56,** 374-399.

Xu, K.-M., and many co-authors, 2002: An intercomparison of cloud-resolving models with the Atmospheric Radiation Measurement summer 1997 Intensive Observation Period data. *Quart. J. Roy. Meteor. Soc.,* **128,** 593-624.

Yanai, M. and R. H. Johnson, 1997: Impacts of cumulus convection on thermodynamic fields. In *The physics and parameterization of moist atmospheric convection*, R. K. Smith, Ed., Kluwer Academic Publishers, 39-62.

Yanai, M., S. Esbensen and J. Chu, 1973: Determination of bulk properties of tropical cloud clusters from large-scale heat and moisture budgets. *J. Atmos. Sci.,* **30,** 611-627.

Yang, G.-Y. and J. Slingo, 2001: The diurnal cycle in the tropics. *Mon. Wea. Rev.,* **129,** 784-801.

Yang, G.-Y., B. Hoskins and J. Slingo, 2003: Convectively coupled equatorial waves: A new methodology for identifying wave structures in observational data. *J. Atmos. Sci.,* **60,** 1637-1654.

Yano, J.-I. P. Bechtold, J.-L. Redelsperger and F. Guichard, 2004: Wavelet-compressed representation of deep moist convection. *Mon. Wea. Rev,* **132,** 1472-1485. *Quart. J. Roy. Meteor. Soc.,* **131,** 2313-2336.

Yano, J.-I., J.-L. Redelsperger, P. Bechtold and F. Guichard, 2005: Mode decomposition as a methodology for developing convective-scale representations in global models. *Quart. J. Roy. Meteor. Soc.,* **131,** 2313-2336.

Žagar, N., Andersson, E. and M. Fisher, 2005: Balanced tropical data assimilation based on a study of equatorial waves in ECMWF short-range forecast errors. *Q. J. R. Meteorol. Soc.,* **131,** 987-1011.

Žagar, N., A. Kasahara, K. Terasaki, J. Tribbia and H. Tanaka, 2015: Normal-mode function representation of global 3D datasets: an open-access software for atmospheric research community. Geosc. Model Dev.

Zhang, C., 2005: Madden-Julian oscillation. *Rev. Geophys.,* **43,** doi:10.1029/2004RG000158.Zhang, G. J. and N. A. McFarlane, 1991: Convective stabilization in midlatitudes. *J. Atmos. Sci.,* **119,** 1915-1928.

Zhang, G. J. and H.-R. Cho, 1991: Parameterization of the vertical transport of momentum by cumulus clouds. Part I: Theory. *J. Atmos. Sci.,* **48,** 1483-2539.

Zhang, G. J. and X. Wu, 2003: Convective momentum transport and perturbation pressure field from a cloud-resolving model simulation. *J. Atmos. Sci.,* **60,** 1120-1139.